Theses and Dissertations

Graduate School

2016

Electronic Structure and Stability of Ligated Superatoms and Bimetallic Clusters

William H. Blades

VCU Department of Physics, Bladeswh@vcu.edu

Virginia Commonwealth University

This is to certify that the thesis prepared by William H. Blades, entitled ELECTRONIC STRUCTURE AND STABILITY OF LIGATED SUPERATOMS AND BIMETALLIC CLUSTERS, has been approved by his committee as satisfactory completion of the requirements for the degree of Master of Science in Physics and Applied Physics.

_____

Shiv N. Khanna, Ph.D., Department of Physics

_____

Marilyn F. Bishop, Ph.D., Department of Physics

_____

Alenka Luzar, Ph.D., Department of Chemistry

_____

Alison Baski, Ph.D., Interim Dean, College of Humanities and Sciences

_____

F. Douglas Boudinot, Ph.D., Dean, Graduate School

May 4, 2016

Electronic Structure and Stability of Ligated Superatoms and Bimetallic Clusters

A thesis submitted in partial fulfillment of the requirements for the degree of Master of Science at Virginia Commonwealth University

by

William Harrison Blades

B.S. Physics, 2014
Virginia Commonwealth University

M.S. Physics and Applied Physics, 2016
Virginia Commonwealth University

Director: Dr. Shiv N. Khanna
Commonwealth Professor
Department of Physics

Virginia Commonwealth University
Richmond, Virginia
May 2016

Acknowledgements

First, I would like to thank my advisor Professor Shiv Khanna for giving me the opportunity to be a part of his world renowned group. His calm demeanor and positive attitude made conducting research a pleasant experience, and I am very grateful for his help and guidance these past two years. I would also like to thank Dr. Arthur Reber for his constant support. Art has been an excellent teacher and has spent a significant portion of his valuable time to help me throughout this process. Without his advice and instruction, I would not have smoothly negotiated this path. Dr. Vikas Chauhan has also been an excellent source of inspiration and guidance, and I thank him for spending his time instructing me. Dr. Bishop and Dr. McMullen have taught the majority of my physics classes at VCU, and I would like to thank them for the many hours they spent imparting their knowledge onto me. My undergraduate research advisor Dr. McLeskey has provided excellent advice and support, and I appreciate the opportunities he gave me during my senior year. Last but not least, I would like to thank my high school physics teacher Michael Fetsko for generating my interest in physics. Outside the academic circle I would like to thank my family and friends for their unwavering support while I have chased my dreams. You all have been a constant source of inspiration, and I love you all very much.

Table of Contents

Chapter 1. Introduction

Chapter 2. Theoretical Methods

Chapter 3. Experimental Methods

Chapter 4. What Determines if a Ligand Activates or Passivates a

Superatom Cluster?

Chapter 5. Magnetic Spin Moments and Stability of Bimetallic Transition Metal Clusters: VCu_n^+, VAg_n^+, VAu_n^+ (n = 2-14)

Chapter 6. Conclusions

List of Tables and Figures

Abstract

ELECTRONIC STRUCTURE AND STABILITY OF LIGATED SUPERATOMS AND BIMETALLIC CLUSTERS

By William Harrison Blades

A thesis submitted in partial fulfillment of the requirements for the degree of Master of Science at Virginia Commonwealth University

Virginia Commonwealth University, 2016

Major Director: Dr. Shiv N. Khanna, Commonwealth Professor, Department of Physics

Quantum confinement in small metal clusters leads to a bunching of states into electronic shells reminiscent of shells in atoms. The addition of ligands can tune the valence electron count and electron distribution in metal clusters. A combined experimental and theoretical study of the reactivity of methanol with $Al_nI_m^-$ clusters reveals that ligands can enhance the stability of clusters. In some cases the electronegative ligand may perturb the charge density of the metallic core generating active sites that can lead to the etching of the cluster. Also, an investigation is conducted to understand how the bonding scheme of a magnetic dopant evolves as the electronic structure of the host material is varied. By considering VCu_n^+, VAg_n^+, and VAu_n^+ clusters, we find that the electronic and atomic structure of the cluster plays a major role in determining how an impurity will couple to its surroundings.

Chapter 1

Introduction

1.1 Motivation

With the birth of quantum mechanics in the early 20th century, it was immediately apparent that the laws governing the interactions and dynamics of the atomic scale were strikingly different from the Newtonian framework used to describe macrosystems. As quantum mechanics and solid-state physics continued to progress and our instrumentation and tools became more accurate, a plethora of opportunities were made available. We eventually gained the ability to study and control incredibly small amounts of matter, and through careful experimentation and analysis, the subsequent physical phenomena that arose from such precise manipulation were realized. Exciting new possibilities were made apparent as we discovered how drastically an atomic system changes with alterations to its geometry, charge state, and composition. These capabilities eventually gave rise to a prerogative that was grounded in using the highly variable properties of nanoscale systems to make materials stronger, faster, and more compact. Or as Richard Feynman so aptly stated, "There's Plenty of Room at the Bottom." The world heeded Dr. Feynman's words, and the area of nanoscience was born.

As the dimensions of a material are reduced below 100 nanometers, the electronic states of the system become more discrete and are subject to the rules of quantum confinement. Not only are there variations in the electronic profile of the material, but the geometric structure of a quantum confined system will follow a different packing regime than the bulk material. The departure from both the electronic and geometric bulk structure properties is the most desirable aspect of nanoscale systems. It has been the goal of The Shiv Khanna Research Group at Virginia Commonwealth University to study the effects of quantum confinement on small clusters of atoms.[1] Understanding the fundamental properties that govern the electronic structure, geometric configuration, and stability of these clusters is of great importance. By identifying energetically favorable systems, new avenues are made available that could lead to cluster-assembled materials that take advantage of the unique-nanoscale properties that clusters possess.[2] Simply by changing a cluster's size, composition, and charge state, varying properties can be realized, which could be used to drive the principal properties of the assembled material.

To make cluster-assembled materials a reality, it is advantageous to first classify stable clusters that could be used as building blocks to form novel materials. By studying the reactivity of clusters with polar solvents and oxygen, systems that are chemically inert under ambient conditions can be identified. Previous studies have shown that ligands can be added to a cluster to tune the valence count and act as protecting groups against etching.[3–7] However, what is unclear is under what circumstances will a ligand cause a cluster to become reactive or unreactive, and what kind of conditions lead to the passivation or activation of the cluster. Synergetic theoretical and experimental studies have taken place to establish how a ligand changes the reactivity pattern of a metallic cluster.

Another area of interest revolves around understanding the fundamental properties that dictate how a quantum confined system will couple to a dopant with a magnetic spin moment. It has been shown previously that introducing impurities into clusters can result in a localized spin moment and changes in the valence of the magnetic impurity.[8–13] As the cluster grows in size, the magnetic impurity will start to bond more effectively with the constituent atoms in the cluster and under the right circumstances the magnetic spin moment of the system may be quenched. The stability of these clusters follows a simple shell-filling scheme; however exactly when and how this localized magnetic spin moment will couple to its surrounding is not fully understood. By varying the electronic and geometric composition of the surrounding cluster, greater insight into the underlying mechanisms that drive how the host material interacts with the localized magnetic spin moment can be provided.

1.2 Magic Numbers

Cluster science involves observing and analyzing the electronic and structural trends in groups of atoms as they evolve from a couple of atoms to their bulk configurations. The origins of cluster science are rooted in the extensive research efforts that sought to understand and explain the intensity and distribution of clusters generated in the gas phase. These studies involved vaporizing a source material with a laser, ionizing the generated clusters, and measuring the distribution of ionized clusters by analyzing their mass to charge ratio. In the mid 1980s Knight and co-workers analyzed sodium clusters and observed peaks in intensity at clusters containing 2, 8, 20, 40, 58 and 92 atoms.[14] An electronic shell model was derived to explain the observed peaks in the mass spectrum. This model was an extension of the nuclear

shell model, but instead pertained to a delocalized electronic gas that the valence electrons of the individual atoms comprise. This paradigm has been one of the most successful frameworks proposed by the cluster science community and continues to be a cornerstone of the field today.

1.2.1 The Spherical Jellium Model

The electronic shell model that was used to account for the peaks observed in the nascent mass spectrum of sodium clusters by Knight and co-workers provides a relatively simple scheme to account for the confinement of an electron gas.[14,15] It assumes that the nucleus of the atoms and the core electrons provide a uniform spherical distribution of background charge of radius r_0. This approach to understand the behavior of small metal clusters was first suggested by Walter Ekardt in 1984.[16] A potential, that is radially dependent and based on the charge distribution, is found and is approximately constant inside the radius of the system in question,

$$U(r) = \frac{U_0}{\exp\left[\frac{r - r_0}{\varepsilon}\right] + 1}$$

where U_0 is the sum of the Fermi energy and the work function of the bulk material, r_0 is the effective radius of the cluster sphere, and ε is a parameter that determines the variation of the potential at the edge of the sphere. The concept of a homogeneous background charge is contingent on the delocalized nature of the valence electrons. Instead of being localized on their respective nuclei, the valence electrons are confined to the cluster and contribute to a nearly free electron gas. This uniform background charge distribution and the metallic like behavior it resembled was characterized by Conyers Herring as a "positive jelly" and is now known as the *Spherical Jellium Model*.[17]

Adopting this time-independent spherical potential will allow the solutions to Schrodinger's equation to be separated into radial and angular parts, R and Y respectively. This begins by writing the wavefunction as a product,

$$\Psi_{n,\ell,m}(r,\theta,\varphi) = R_{n,\ell}(r)Y_{\ell,m}(\theta,\varphi)$$

where n is the principal quantum number, ℓ is the angular quantum number, and m is the magnetic quantum number. Valence electrons subjected to this spherical potential that only depends on the radius r_0, will have solutions that yield atomic like shells. These solutions will still be contingent on the quantum numbers ℓ and n; however there is no $\ell < n$ restriction like there is for the atoms on the periodic table. Therefore, the valence electrons that are subjected to such conditions would correspond to the delocalized orbitals $1S^2$, $1P^6$, $1D^{10}$, $2S^2$, $1F^{14}$, $2P^6$ etc. The capitol letters are used to distinguish the usual atomic orbitals (s, p, d, etc) and the delocalized orbitals (S, P, D, etc). These delocalized orbitals are at the heart of cluster physics and will be used throughout this thesis.

1.3 Superatoms

The early conceptual framework surrounding the reactivity of clusters began with studies on aluminum-based clusters carried out by The Castleman Group at The Pennsylvania State University.[1,18,19] A size dependent reactivity pattern was observed in which Al_{13}^-, Al_{23}^-, and Al_{37}^- were unreactive when exposed to oxygen. Aluminum has three valence electrons, and so the stability was attributed to the shell closures at 40, 70, and 112 electrons respectively, which corresponds to the filled electronic shells in the Jellium model proposed by Knight et. al. in

1984. This study gave clear indication that the electronic profile of a cluster not only determines the abundances observed in the mass spectrum, but a cluster's chemical properties as well.

In a series of papers written in 1990s, Khanna and Jena[20–23] proposed that by changing the charge state, composition, or geometry of a cluster, stable clusters with closed geometric and electronic shells could be synthesized. These electronically favorable systems were coined superatoms. These superatoms could be specifically tailored to exhibit desired properties beyond those displayed by the cluster's constituent atoms. The cornerstone of their work was focused on taking advantage of the electronic and geometric stability of clusters with closed shells.[24] This concept was expanded with extensive work done with aluminum-based clusters, such as $Al_{12}C$, $Al_{13}K$, and Al_{13}^-, that aimed to understand the chemical properties of clusters with closed electronic and geometric shells. One of the most promising results was that of Al_{13}^- which has the corresponding delocalized orbitals $1S^2$, $1P^6$, $1D^{10}$, $2S^2$, $1F^{14}$, $2P^6$ and an electron affinity of 3.62 eV.[25] This electronic structure and unusually high electron affinity allowed analogies to be drawn between Al_{13}^- and halogens, specifically chlorine (electron affinity 3.61 eV).[25,26] After subsequent theoretical and experimental research was conducted to show how Al_{13}^- bound to potassium, this halogen like nature was confirmed, which allowed Al_{13}^- to be classified as a superatom with halogen-like characteristics. These findings introduced the idea that certain clusters could make up a new dimension of the periodic table of elements.

A joint effort undertaken by the Castleman and Khanna groups centered on building the conceptual basis behind an extended periodic table of elements. Together, they worked on cementing the definition of a superatom cluster and in doing so established the superatom concept within the field of cluster science.[1,11,27–31] This new conceptual basis no longer centered on clusters that simply mimicked the properties of elemental atoms. According to the modified

concept, superatoms are clusters with their electronic states grouped into shells with well-defined valences that demonstrate completely new chemical features beyond those exhibited by the constituent atoms. This new standard of enhanced energetic and chemical stability was probed by continuing work on the superhalogen Al_{13}^-. Reactivity studies were carried out by ligating Al_{13}^- with halogens and exposing the clusters to O_2.[31–33] It was discovered that $Al_{13}I^-$ and $Al_{13}I_2^-$ were resistant to oxygen etching and maintained the relatively high electron affinity observed in Al_{13}^-. The chemically inert behavior displayed by these aluminum iodide anion based clusters allowed for their classification as superhalogens. More reactivity studies were undertaken, which served as a means to probe the electronic profile of these superatom systems. In doing so, additional information was gathered about the chemical behavior of these elegant systems. The reactivity patterns of superatom clusters are discussed in the sections below. First, a general overview of oxygen reactivity is provided in Section 1.3.1. Then, in Section 1.3.2 the reactivity of bare anionic aluminum clusters with methanol is discussed. The fine distinctions between the two reactivity patterns are highlighted, which provides a clear indication of the dual reactivity pattern superatom clusters possess.

1.3.1 Oxygen Etching

A)

$Al_n^- + O_2$

Al_{13}^-

Al_{23}^-

Al_9^- Al_{11}^- Al_{15}^- Al_{17}^- Al_{21}^-

Intensity

SPE (eV)

Al_{13}^-

Al_{23}^-

Al_{21}^-

Al_n^-

B)

$Al_{13}^- + O_2$

$Al_5^- + O_2$

$Al_4H_3^- + O_2$

$Al_3^- + O_2$
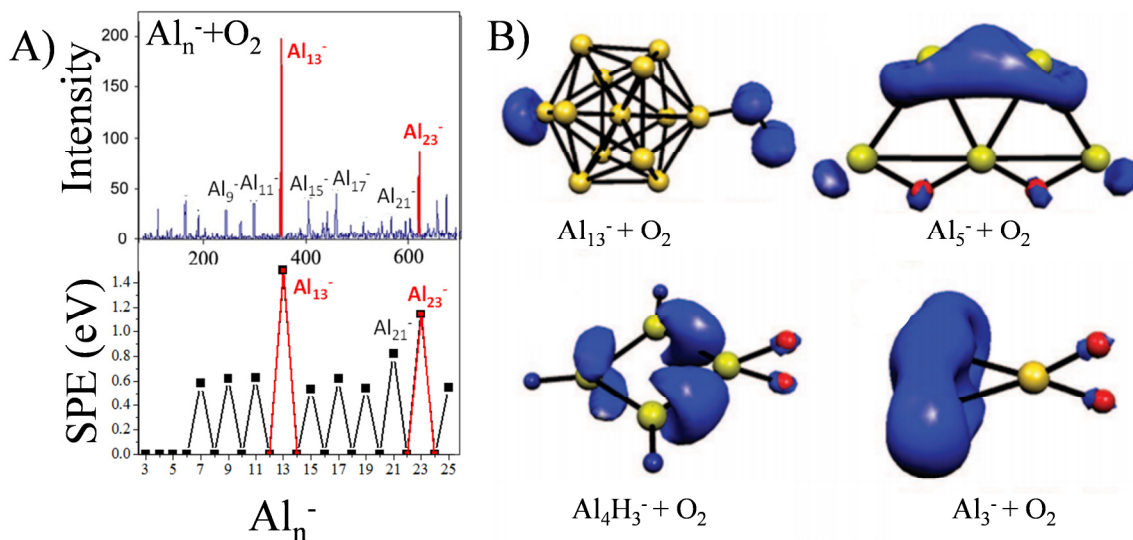
Figure 1.3.1 A) The mass spectrum of anionic aluminum clusters in gas phases etched with oxygen, and their corresponding spin excitation energy (SPE). Al_{13}^- and Al_{23}^- have large HOMO-LUMO gaps, which correspond to a SPE of 1.4 eV and 1.2 eV respectively. B) Spin density and geometric structures of Al_{13}^-, Al_5^-, $Al_4H_3^-$, and Al_3^- with O_2.[1,34]

As mentioned above, superatoms exhibit enhanced resistance to etching when exposed to reactants, such as O_2.[34] This resistance can be attributed to the large energy gap between the cluster's highest occupied molecular orbital and lowest unoccupied molecular orbital (HOMO-LUMO gap). For example, Al_{13}^- has 40 valence electrons that fill the $1S^2$ $1P^6$ $1D^{10}$ $2S^2$ $2F^{14}$ $2P^6$ delocalized electronic shells and a HOMO-LUMO gap of 1.83 eV. To react with O_2, which has a triplet ground state and unfilled minority pi* orbitals, the minority pi* orbitals need to be filled. This will require a spin excitation of the cluster to conserve the overall spin of the reactive complex. For the cluster to generate an excited spin state it will have to overcome a spin excitation barrier. The activation energy necessary to overcome this barrier is determined by the HOMO-LUMO gap of the cluster. If the cluster has a sufficiently high HOMO-LUMO gap it does not react, and the spin remains localized on the oxygen atoms. Through a combined

8

theoretical and experimental effort it was found that in gas phase, clusters with a gap exceeding 1.2 eV are resistant to O_2 etching. This means that the spin excitation energy, which is determined by the HOMO-LUMO gap, controls the reactivity of aluminum clusters and is an energetically driven process.

1.3.2 Reactivity of Polar Solvents
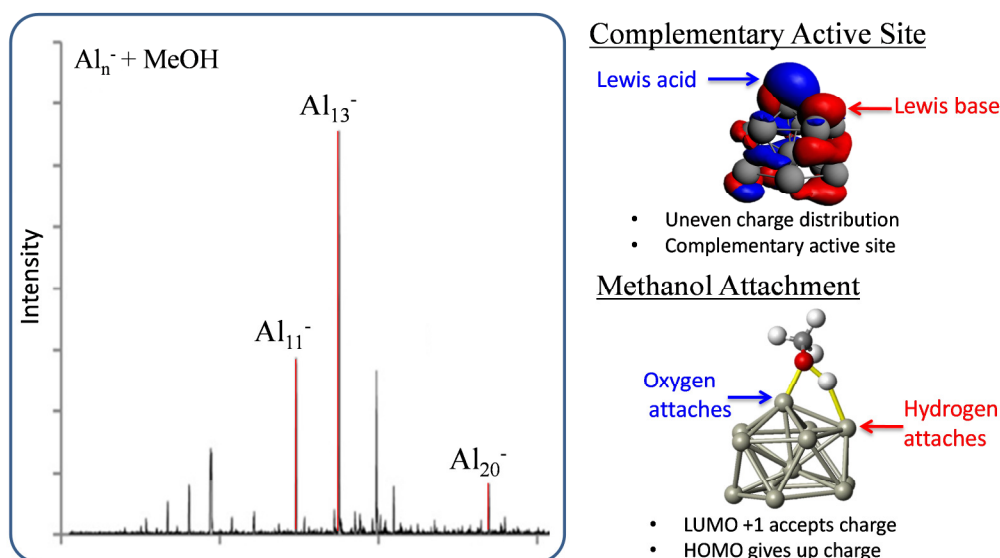
Figure 1.3.2. The mass spectrum Al⁻ clusters in gas phases etched with methanol. A schematic diagram of the complementary active sites that are responsible for the reactivity. The placement of the methanol molecule's oxygen and hydrogen atoms on the active sites are also shown.

Earlier studies have shown that clusters exhibit a dual reactivity pattern, meaning they react differently when exposed to oxygen than to polar solvents like water or methanol. The geometry of the cluster and the distribution of charge density have been shown to play the determining role in whether a cluster will react to a polar solvent.[35–37] When a cluster has an uneven charge density, Lewis acid sites that accept charge and Lewis base sites that donate charge are primarily responsible for the manner in which the polar solvent will interact with the cluster. The Lewis acid site is most important because when the oxygen atom in water or alcohol

9

attaches to the site, a lone pair of electrons is transferred to the cluster. This makes the cluster's ability to accept charge paramount in whether it will be reactive or unreactive when exposed to protic species.

When a cluster has both a Lewis acid and Lewis base, this complementary active site will make the cluster highly susceptible to react with polar solvents. These complementary active sites are observed when a cluster has an adatom site or an uneven geometric feature that perturbs the charge density of the system. Therefore, the stability of metal clusters are maximized when, (i) the cluster has a closed electronic shell that corresponds to a HOMO-LUMO gap larger than 1.2 eV; and (ii) the charge density is evenly distributed over the surface of the cluster preventing the presence of active sites. What is not understood, however, is how will a ligand interact with the cluster to either bolster or diminish these effects.

1.4 Localized Magnetic Spin Moments

Previous studies have shown that when a dopant is added to a cluster, the valence electrons of that impurity will not always participate in hybridized bonding with the rest of the cluster's valence electrons.[8,9,27,38–41] Instead of interacting with the nearly fee electron gas and forming delocalized electronic shells, the valence electrons of the dopant will remain confined to the atom. These highly localized electronic states found on the impurity have a magnetic spin moment, the magnitude of which depends on the number of unpaired electrons. However, as the cluster grows in size these localized electrons will start to participate in hybridized bonding with the host cluster's valence electrons. In some cases, if there is a large enough electronegative difference between the dopant and the host material, the impurity can pull electrons from the

10

surrounding atoms and the magnetic spin moment will become larger in magnitude. Precisely when and how this bonding occurs is determined by the electronic structure of the dopant and the host material, respectively. It has been shown previously that the valence of the dopant will evolve as a cluster grows in size.[8,9] As this process takes place, some of the dopant's electrons will form hybridized bonds, while others will continue to be localized. Eventually there is a transition in valence that correlates to the symmetry of the delocalized electronic orbitals, and all of the dopant's valence electrons will participate in hybridized bonding. This leads to an eventual quenching of the magnetic spin moment as these valence electrons successfully couple to the nearly free electronic gas. The purpose of this work is to examine exactly how the electronic structure of the host material affects this valence transition and the manner in which these localized electronic states couple to the surrounding atoms.
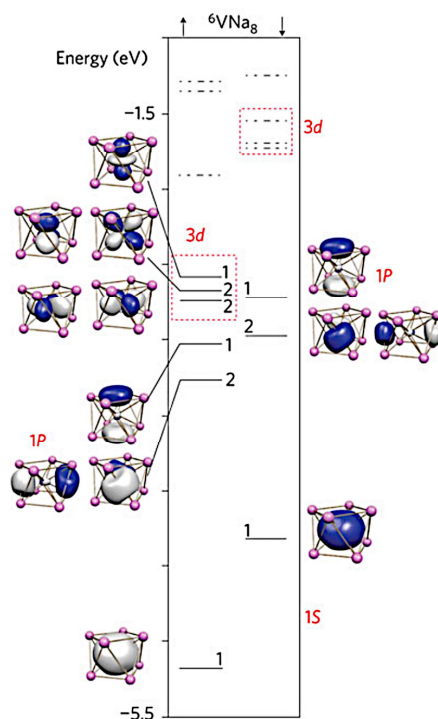

Figure 1.4. Molecular orbital diagram of a VNa$_8$ cluster. The filled lines correspond to the filled states and the dotted lines correspond to the unfilled states. Each localized (lowercase letter) and delocalized (uppercase letter) orbital is labeled.[11]

11

1.5 Summary and Thesis Layout

As outlined in Chapter 1, it is the goal of this thesis to understand the fine distinctions regarding the reactivity patterns of ligated superatom clusters and the bonding scheme of bimetallic clusters with localized magnetic spin moments. Applying a first principles density functional theory approach, the Amsterdam Density Functional set of codes is employed as a means to evaluate each cluster's electronic structure and stability. Chapter 2 of this thesis will cover a general background of Density Functional Theory and provide information regarding some of the important details of the theory. Once that has been completed, a brief outline of the experimental techniques used at The Pennsylvania State University will be given in Chapter 3 (The specific parameters used in reactivity study will be provided in chapter 4). The main body of work contained within this thesis is broken down into two chapters. Chapter 4 comprises the aluminum iodide reactivity study and Chapter 5 covers the magnetic spin moments and bonding of bimetallic copper, silver, and gold vanadium clusters. A summary of each chapter is offered at the end of the respective chapter, and a general summary and future project section is provided at the end of this report in Chapter 6. The appendix of this thesis contains the supplemental material of both chapters 4 and 5, and is subsequently divided into two sections.

Chapter 2

Theoretical Methods

2.1 Quantum Mechanics

The birth of quantum mechanics began with investigations into the behavior and nature of light in the 17th century. Notable scientists such as Roberts Hooke, Leonhard Euler, and Thomas Young proposed a wave theory of light, which differed greatly from the accepted theory at the time that light behaved like a particle. Louis de Brogie, who derived a relation between momentum and wavelength, defined one of the more groundbreaking consequences of quantum mechanics. The relationship between wavelength and momentum is expressed as,

$$\lambda = \frac{\hbar}{p}$$

where λ is the wavelength, p is the momentum, and $\hbar$ is Planck's constant. This showed that electrons not only behave like particles, but also exhibit properties of waves. Thus, wave-particle duality was born. This is an essential piece of quantum confinement, which arises once the diameter of a material is equal to the de Broglie wavelength of the electron wave function.

To evaluate the quantum mechanical behavior of a physical system, Erwin Schrodinger derived an equation to determine the wavefunctions of a quantum state. In the simplest form the time independent Schrodinger equation is an energy eigenvalue equation,

$$\hat{H}\Psi_i = E\Psi_i$$

where $\hat{H}$ is the Hamiltonian, Ψ_i is the eigenstate or wavefunction, and E is the energy. Substituting in the kinetic and potential energy terms (in atomic units) into the Hamiltonian yields the following expression,

$$[-\frac{1}{2}\nabla_i^2 + V(\vec{r})]\Psi_i(\vec{r}) = E\Psi_i(\vec{r})$$

This is known as the Schrodinger wave equation, and is the foundation of which all theories that analyze quantum mechanical systems are based, such as the Hartree-Fock and Kohn-Sham methods described in later sections. In this form the Schrodinger equation is very manageable and can be solved with relative ease. However, many body systems quickly turn this equation into something that is extremely difficult to solve without the right approximations.

2.2 Born-Oppenheimer Approximation

With the advent of the Schrodinger equation, physicists started to design specific Hamiltonians to handle explicit many body systems.[42,43] For example, the exact Hamiltonian for a system that contains N electrons and M nuclei is written as,

$$\hat{H} = -\sum_{i=1}^{N}\frac{1}{2}\nabla_i^2 - \sum_{A=1}^{M}\frac{1}{2M_A}\nabla_A^2 - \sum_{i=1}^{N}\sum_{A=1}^{M}\frac{Z_A}{r_{i,A}} + \sum_{i=1}^{N}\sum_{j>1}^{N}\frac{1}{r_{i,j}} + \sum_{A=1}^{M}\sum_{B>A}^{M}\frac{Z_A Z_B}{R_{A,B}}$$

where M_A is the mass of the nuclei, $R_{A,B}$ are the position of the nuclei, and $r_{i,j}$ represent the position of the electrons. The first two terms represent the kinetic energy of the electrons and

nuclei respectively. The last three terms characterize the attractive electrostatic interactions between the nuclei and the electrons and the repulsive potential due to the electron-electron and nucleus-nucleus interactions. Although this is the exact Hamiltonian for a many electron system, using this to evaluate Schrodinger's equation proves to be extremely difficult for a many electron system. In the early 20th century two scientists, Max Born and J. Robert Oppenheimer, expounded upon the exact Hamiltonian by separating the ion kinetic energy terms of the operator. By developing this framework, the Hamiltonian for a many electron system can be broken down into two terms: the Hamiltonian of M interacting ions ($\widehat{H}_I$) and N interacting valence electrons ($\widehat{H}_e$) that experience some external potential,

$$\widehat{H} = \widehat{H}_e + \widehat{H}_I$$

This approximation takes advantages of the differences between the scale of the electrons and the nuclei. According to the Born-Oppenheimer approximation, because the mass of the electrons are significantly smaller than the mass of the nuclei, the electrons can be considered to be moving in a field of fixed nuclei, where the nuclear kinetic energy term is zero and the nuclear potential energy is constant. The electron only part of the Hamiltonian is written as,

$$\widehat{H}_e = -\sum_{i=1}^{N} \frac{1}{2}\nabla_i^2 - \sum_{i=1}^{N}\sum_{A=1}^{M} \frac{Z_A}{r_{i,A}} + \sum_{i=1}^{N}\sum_{j>1}^{N} \frac{1}{r_{i,j}} = T_e + V_{eI} + V_{ee}$$

where T_e is the kinetic energy of the electrons and V_{eI} and V_{ee} are the potential energy terms of the electron-nuclei and electron-electron interactions. The ions are handled separately and are represented by stationary nuclei that generate an electric potential the electrons move in. Applying the Born-Oppenheimer approximation the Hamiltonian of M interacting ions is expressed as,

$$\widehat{H}_I = \sum_{A=1}^{M} \sum_{B>A}^{M} \frac{Z_A Z_B}{R_{A,B}}$$

This framework is called the clamped nucleus Hamiltonian or electronic Hamiltonian. Using the Born-Oppenheimer approximation the Schrodinger equation is evaluated by separating the wavefunctions of a many body system into electronic and nuclear components. The electronic and nuclear Hamiltonians then operate on these respective wavefunctions. The total energy of the system is simply $E_{tot} = E_e + E_N$, where E_e and E_N are the respective electronic and nuclear energies.

2.3 Hartree Theory

Once Born and Oppenheimer had approximated the many body Schrodinger equation, an English mathematician and physicist by the name of Douglas Hartree devised a method to handle a many-electron system that was subjected to a static external potential $V(\mathbf{r})$.[44-46] When dealing with a many-electron system, Hartree approximated the total electron wavefunction $\Psi_0(\vec{r}_1, \vec{r}_2 ... \vec{r}_N)$ as a product of one-electron functions $\phi_i^H(\vec{r}_i)$,

$$\Psi^H(\vec{r}_N) = \prod_{i=1}^{N} \phi_i^H(\vec{r}_i)$$

Using these notions, the one-electron Schrodinger equation becomes what is known as the Hartree equation,

$$\sum_{i=1}^{N} [-\frac{1}{2}\nabla_i^2 + V(\vec{r}_i)]\phi_i^H(\vec{r}_i) + \sum_{j=1,j\neq i}^{N} \int d^3 r_j \frac{\left|\phi_j^H(\vec{r}_j)\right|^2}{\left|\vec{r}_i - \vec{r}_j\right|}\phi_i^H(\vec{r}_i) = E_i \phi_i^H(\vec{r}_i)$$

16

where N is the total number of electrons, the static potential is $V(\vec{r}_i) = -\sum_{A=1}^{M} \frac{Z_A}{r_{i,A}}$, $\phi_i^H(\vec{r}_i)$ is the wavefunction that represents each electron, and E_i is the energy eigenvalue of the ith electron. The third term is known as the Hartree potential. This is a self-consistent field caused by the electrons, and is a potential the ith electron experiences.[46] The final solution of this equation has to be self-consistent with the initial guess; therefore self-consistency is a requirement of the Hartree method. Although this method gives an approximate numerical value, the Pauli exclusion principle is violated and the self-consistent potential acting upon the ith electron depends on i, which makes wavefunctions $\phi_i^H(\vec{r}_i)$ non-orthogonal.[45] However, Hartree's formalism was improved upon with the derivation of the Hartree-Fock equations, which is discussed in the subsequent section.

2.4 Hartree-Fock Theory

Vladimir Fock helped build upon Hartree's method by introducing a scheme that approximated the wavefunctions and energy levels of atoms and handled the antisymmetry of electronic wave functions.[44–47] Fermions have antisymmetric wavefunctions, which can be represented mathematically,

$$\Psi(\vec{r}_1, \vec{r}_2) = -\Psi(\vec{r}_2, \vec{r}_1)$$

This introduced an anti-symmetrized product into the one electron wavefunctions, and by writing the anti-symmetrized wavefunctions using a Slater determinant the shortcomings of the Hartree equation were finally resolved. A Slater determinant can be written generally as,

17

$$\Psi\left(\vec{r}_1, \vec{r}_2 \ldots \vec{r}_N\right) = \frac{1}{\sqrt{N!}} \begin{bmatrix} \psi_1(\vec{r}_1) & \psi_2(\vec{r}_1) & \cdots & \psi_N(\vec{r}_1) \\ \psi_1(\vec{r}_2) & \psi_2(\vec{r}_2) & \cdots & \psi_N(\vec{r}_2) \\ \vdots & \vdots & \ddots & \vdots \\ \psi_1(\vec{r}_N) & \psi_2(\vec{r}_N) & \cdots & \psi_N(\vec{r}_N) \end{bmatrix}$$

where the determinant will go to zero if $\Psi\left(\vec{r}_1 = \vec{r}_2\right)$. Now the total wavefunction can be written as an anti-symmetrized product (A) of one-electron wavefunctions $\phi_i^{HF}(\vec{r}_i)$, which satisfies the Pauli exclusion principle. The Hartree-Fock wavefunctions are expressed as,

$$\Psi^{HF}(\vec{r}_N) = A \prod_{i=1}^{N} \phi_i^{HF}(\vec{r}_i)$$

Using the Hartree-Fock method leads to a procedure that approximately solves the time-independent Schrodinger equation,

$$\sum_{i=1}^{N}[-\frac{1}{2}\nabla_i^2 + V(\vec{r}_i)]\phi_i^{HF}(\vec{r}_i) + \sum_{j=1, j\neq i}^{N} \int \frac{d^3 r_j}{|\vec{r}_i - \vec{r}_j|} [\left|\phi_j^{HF}(\vec{r}_j)\right|^2 \phi_i^{HF}(\vec{r}_i) - \phi_j^{HF}(\vec{r}_j)\phi_i^{HF}(\vec{r}_j)\phi_j^{HF}(\vec{r}_i)] = E_i \phi_i^{HF}(\vec{r}_i)$$

To summarize, this method assumes that the wavefunction can be approximated by a single Slater determinant, which provides the lowest energy eigenvalue of the wavefunction, and is made up of one spin orbital per electron.[44,47] Just like the Hartree equation this process also relies on the self-consistent field method, which requires the final wavefunction to be equal to the initial wavefunction until the associated energy eigenvalues are changing by an assigned energy difference. Therefore, an initial wavefunction is taken, this is used to define the electron density $\left|\phi_j(\vec{r})\right|^2$, the Hartree-Fock equation is evaluated using this trial wavefunction, and an output wavefunction is realized. This process continues until the wavefunctions found in the last step are consistent with the trail wavefunctions used to define the electron density. If they are not, a new estimate is used, and the iterative process begins again.

2.5 Density Functional Theory

The development of the Born-Oppenheimer approximation and the Hartree-Fock method were critical steps in developing what is known as Density Functional Theory (DFT). This theory has allowed atomic physicists the ability to calculate the wavefunctions and energy eigenvalues for systems comprised of numerous atoms and molecules. Today, it is a state of the art method for calculating the electronic and geometric structures of a wide variety of systems. The supposition that surrounds this theory is the electron density distribution can accurately represent the ground state of a many electron system.

This was successfully realized when Walter Kohn, Pierre Hohenberg, and Lu Sham produced a set of ground breaking papers in the mid-1960s that formed the basis for DFT.[46–48] The center of this theory revolves around the electron density of the system. This can be written as,

$$n(\vec{r}) = N \int d^3 r_2 \int d^3 r_3 ... \int d^3 r_N \Psi^*(\vec{r}_1, \vec{r}_2 ... \vec{r}_N) \Psi(\vec{r}_1, \vec{r}_2 ... \vec{r}_N)$$

This electron density is then used to construct the many-body system's potential, onto a single-body calculation. This is done by using the electron density $n(\vec{r})$ as a variable that all other observables in the system will be based on. By knowing the particle density, the wavefunction and potential energy of a system can be known, allowing for the subsequent calculation of the other observables in the system. This idea is discussed in more detail in the following sections, and a general overview of the Hohenberg-Kohn Theorems and Kohn-Sham equation is provided.

2.5.1 Hohenberg-Kohn Theorems

Pierre Hohenberg and Walter Kohn expanded the Hartree-Fock method in the spring of 1965 to more accurately account for the electronic nature of many particle systems.[46,47,49] Their work utilized functionals, which represent the spatially dependent density of electrons in a system. The cornerstone of Hohenberg-Kohn theorem revolves around the idea that given a ground state density $n_0(\bar{r})$ it is possible to calculate the corresponding ground-state wavefunction $\psi_0(\bar{r}_1, \bar{r}_2 ... \bar{r}_N)$. In other words, if the ground-state wavefunction $\psi_0(\bar{r}_N)$ is a functional of $n_0(\bar{r})$ then all the ground-state observables are functionals of $n_0(\bar{r})$ as well. Simply put, if $\psi_0(\bar{r}_N)$ can be calculated from $n_0(\bar{r})$ than both functionals are equivalent and contain the same information. A brief summary of the important aspects of the Hohenberg-Kohn Theorem is provided in the following paragraphs.

The nondegenerate ground-state wavefunction is a unique functional of the ground-state density,

$$\Psi_0(\bar{r}_1, \bar{r}_2 ... \bar{r}_N) = \Psi_0[n_0(\bar{r})]$$

A consequence of the ground-state wavefunction being a unique functional of the ground-state density is that the ground-state expectation value of any observable is also a functional of $n_0(\bar{r})$,

$$O[n_0] = \left\langle \psi_0[n_0(\bar{r})] \middle| \hat{O} \middle| \psi_0[n_0(\bar{r})] \right\rangle$$

where $O[n_0]$ is any observable. Therefore, the energy associated with the ground-state wavefunction can be expressed as,

$$E_{v,0}[n_0] = \left\langle \psi_0[n_0(\bar{r})] \middle| \hat{H} \middle| \psi_0[n_0(\bar{r})] \right\rangle$$

20

where $\widehat{H} = \widehat{T} + \widehat{U} + \widehat{V}$. This expectation value has the variational property,

$$E_v[n_0(\bar{r})] \leq E_v[n'(\bar{r})]$$

where $n_0(\bar{r})$ is the ground-state density in potential $\widehat{V}$ and $n'(\bar{r})$ is some other density. If the energy is to be evaluated from some fixed $v(\bar{r})$, then the ground-state density of the system must be used. If the ground-state density is not used the true ground-state energy will never be obtained.[47]

This ground state density, which does not depend on the external potential of the system, determines the electron-ion background and can be represented by a universal functional,

$$F(n) = T(n) + U(n)$$

where $T(n)$ is the functional representing the kinetic energy and $U(n)$ is the functional representing the potential energy. Therefore the ground state energy of an N electron system that is subjected to a potential $v(\bar{r})$ caused by the nuclei is written,

$$E_v[n(\bar{r})] = F(n) + \int d^3 r v(\bar{r}) n(\bar{r})$$

where $E_v[n(\bar{r})]$ is the ground state energy and $F(n)$ is the electronic density functional defined above. The potential energy term is expressed as,

$$V[n(\bar{r})] = \int d^3 r v(\bar{r}) n(\bar{r})$$

This potential is not universal and is dependent on the system that is being studied. Once this potential is known then the functional $V[n(\bar{r})]$ can be obtained. Using these theorems, Walter

Kohn and Lu Sham were able to apply these theorems and devise a way to evaluate many electron systems with relative ease. A summary of this method is provided in the next section.

2.5.2 Kohn-Sham Theorems

A year after the Hohenberg-Kohn paper was published; Kohn collaborated with Lu Sham to produce a scheme that allowed for the indirect minimization of the energy of a many electron system, otherwise known as the exact energy functional.[46,47,50] As with any energy, this contains both kinetic and potential terms. Each of these terms will be disused below:

The kinetic energy $T[n]$ is broken down into two parts: One term represents the kinetic energy of noninteracting electrons of density $n(\vec{r})$, $T_s[n]$. The other term represents the remainder of the kinetic energy or the correlation $T_c[n]$. The single-electron kinetic energy $T_s[n]$ is not known exactly as a functional of $n(\vec{r})$, but can be expressed in terms of the single-particle orbitals of a noninteracting system with density $n(\vec{r})$ as,

$$T_s[n(\vec{r})] = -\sum_{i=1}^{N} \int d^3 r \phi_i^*(\vec{r}) \nabla^2 \phi_i(r)$$

The electrons are noninteracting and therefore the total kinetic energy is simply the sum of the individual kinetic energies. All of the orbitals $\phi_i(\vec{r})$ are functionals of $n(\vec{r})$, therefore $T_s[n]$ is written as an implicit density functional,

$$T_s[n(\vec{r})] = T_s[\phi_i(n)]$$

The energy $T_s[n]$ is not the true kinetic energy of the system; therefore Kohn and Sham introduced exchange-correlation energy into the exact energy functional.[46,47] The exact energy functional can be written,

$$E[n] = T[n] + U[n] + V[n] = T_s[\phi_i(n)] + V_{ext}[n] + V_H[n] + E_{xc}[n]$$

where the exchange-correlation energy $E_{xc}[n]$ contains both the exchange energies due to the Pauli exclusion principle and the correlation energies caused by the instantaneous repulsion of the electrons. The exchange-correlation is discussed in more detail in the next section.

Kohn and Sham then devised a method to indirectly minimalize this exact energy functional. The minimization is written,

$$\frac{\delta E[n]}{\delta n(\bar{r})} = \frac{\delta T_s[n]}{\delta n(\bar{r})} + \frac{\delta V_{ext}[n]}{\delta n(\bar{r})} + \frac{\delta V_H[n]}{\delta n(\bar{r})} + \frac{\delta E_{xc}[n]}{\delta n(\bar{r})} = \frac{\delta T_s[n]}{\delta n(\bar{r})} + v_{ext}(\bar{r}) + v_H(\bar{r}) + v_{xc}(\bar{r}) = 0$$

The terms contained within the minimized energy $E[n]$ will now be discussed in detail. The Born-Oppenheimer approximation yields the ionic potential, which arises from the static ionic background of the nuclei. This potential is external to the electrons in the system and is therefore referred as the external potential and is written as,

$$v_{ext}(\bar{r}) = -\sum_{A=1}^{M} \frac{Z_A}{r_{i,A}}$$

Adapted from the Hartree-Fock equations, the self-consistent electron potential is used and is called the Hartree potential. This is expressed as,

$$v_H(\bar{r}) = \frac{1}{2} \int d^3 r_i \int d^3 r_j \frac{n(\bar{r}_i) n(\bar{r}_j)}{|\bar{r}_i - \bar{r}_j|}$$

23

The last term of $E[n]$ is called the exchange-correlation potential. In its simplest form the exchange-correlation term is,

$$v_{xc}(\vec{r}) = \frac{\delta E_{xc}[n]}{\delta n(\vec{r})}$$

The corresponding energy expression $E_{xc}[n]$ is unknown in the Kohn-Sham approach, where an approximation is considered.[48] This is discussed in more detail in the next section. Now that the energy has been minimalized with respect to electron density, the many-body Schrodinger equation can now be written as the Kohn-Sham equation,[50]

$$[-\frac{1}{2}\nabla_i^2 + v_{ext}(\vec{r}) + v_H(\vec{r}) + v_{xc}(\vec{r})]\Psi_i(\vec{r}) = E\Psi_i(\vec{r})$$

To solve the Kohn-Sham equation the potentials are written together into a single term and a new potential is realized. This potential $v_s(\vec{r})$ is an effective potential that consists of non-interacting particles that generate the same density as any given system of interacting particles.[44,47,48]

$$v_s(\vec{r}) = v_{ext}(\vec{r}) + v_H(\vec{r}) + v_{xc}(\vec{r})$$

By solving the equations of a noninteracting system of electrons that are moving in the potential $v_s(\vec{r})$, the density of the interacting system can be calculated.[46,47] This system is known as an auxiliary equation and is expressed as,

$$[-\frac{1}{2}\nabla_i^2 + v_s(\vec{r})]\phi_i(\vec{r}) = \varepsilon_i\phi_i(\vec{r})$$

which provides the orbitals that generate the electron density $n(\vec{r})$. The Kohn-Sham electron density is found by using the following expression,

$$n_{KS}(\vec{r}) = \sum_{i}^{N} f_i |\phi_i(\vec{r})|^2$$

where f_i is the occupations on the ith orbital. To evaluate the Kohn-Sham equation a simple outline followed:

i) An initial trial electron density $n(\vec{r})$ is defined and $v_s(\vec{r})$ is calculated.

ii) The auxiliary equation is evaluated using the trial electron density and the single-electron wavefunction $\phi_i(\vec{r})$ is found.

iii) The single-electron wavefunctions are then used to define the Kohn-Sham electron density $n_{KS}(\vec{r})$.

iv) This new density is used and the process starts again until the two densities are the same until and the process converges.

This is a very vague description and is missing many important details; however the above procedure gives a good overview of the process used to evaluate the Kohn-Sham equations. After the ground-state electron density has been found the total energy of the system can be calculated. The total ground-state energy is given by the following expression,

$$E_0 = \sum_{i=1}^{N} \varepsilon_i - \frac{1}{2} \int d^3 r_i \int d^3 r_j \frac{n(\vec{r_i})n(\vec{r_j})}{|\vec{r_i} - \vec{r_j}|} - \int d^3 r v_{xc}(\vec{r})n_0(\vec{r}) + E_{xc}[n_0]$$

It is important to note that the eigenvalues, ε_i, obtained from the auxiliary equation have little physical meaning.[47] They are simply the eigenvalues whose eigenfunctions $\phi_i(\vec{r})$ produce the correct electron density. This electron density is what allows for the evaluation of the Kohn-Sham equation.

2.5.3 Exchange-Correlation Functionals

As mentioned above the exchange-correlation energy is unknown in the Kohn-Sham equation. However this can be found by using a uniform distribution of electron gas, where the electron density is constant at all points in space.[46]

$$v_{xc}(\vec{r}) = v_{xc}^{electron-gas}[n(\vec{r})]$$

The exchange-correlation behavior is taken to be the same as that of a uniform electron gas with a density equal to the density of that volume.[48] This allows the exchange correlation potential to be written as a *local density approximation* (LDA) that defines the estimated exchange-correlation functional as,

$$E_{XC}^{LDA}[n(\vec{r})] = \int d^3 r \varepsilon_{xc}[n(\vec{r})] n(\vec{r})$$

where E_{XC}^{LDA} is the exchange-correlation energy per particle of an electron gas with uniform density.[47,48] Most physical systems do not have a uniform charge density and the spatial variation must be included. Therefore, Axel Becke introduced a *generalized gradient approximation* of electron density or GGA parameterization into the Kohn-Sham approach.[51,52] The GGA exchange-correlation energy is written,

$$E_{XC}^{GGA}[n_\uparrow(\vec{r}), n_\downarrow(\vec{r})] = \int d^3 r \varepsilon_{xc}[n_\uparrow(\vec{r}), n_\downarrow(\vec{r}), \nabla n_\uparrow(\vec{r}), \nabla n_\downarrow(\vec{r})] n(\vec{r})$$

This method uses the Hartree-Fock exchange-energy data for atoms, with an added LDA correlation energy, and employs the resulting potential to solve the Kohn-Sham equation.[46] This method reduced the error of the calculation significantly.[48] Both of the studies conducted in this thesis have used the PBE GGA functional to handle the exchange-correlation of our systems.[53]

2.6 DFT in Practice

The Amsterdam Density Functional (ADF) set of codes was used to carry out this theoretical investigation. The electron orbitals are represented by slater type orbitals located at the atomic sites.[54] The Gaussian-type quadrature method is used as the numerical integration scheme for the matrix elements of the exchange-correlation potential.[55–57] This procedure is based on the partitioning of space in the atomic cells. This is represented by a set of integrals that take the general form,

$$\int f(\vec{r})d^3\vec{r} = \int_{sphere} f(\vec{r})d^3\vec{r} + \int_{cell-wthout-sphere} f(\vec{r})d^3\vec{r}$$

where,

$$\int_{sphere} f(\vec{r})d^3\vec{r} = \int_0^R r^2 dr \int_0^{4\pi} f(r,\Omega)d\Omega$$

The Jacobian factor r^2 removes the Coulomb singularity of the integrand at the nuclear position. The remaining cell-minus-sphere region is treated, after suitable coordinate transformations, by a Gaussian product formula in Cartesian-like coordinates.[54] Inside this cell contains a core-region sphere, which fills all space "inside" the molecule. The remaining "outer" region, which is farther away from the atoms, all the integrands decay exponentially as the distance is increased.

2.6.1 Basis Sets

ADF used Slater-type orbitals (STOs) as basis set elements, which are located as the site of each atom.[54] The STOs are expressed using the function,

$$f(\vec{r}) = Y_{\ell,m}(\theta,\varphi)r^n e^{-\alpha r}$$

where $Y_{\ell,m}(\theta, \varphi)$ is the spherical harmonic factor, r has its origin at the center of an atom, and α is the exponential factor that determines the long-rang decay of the function. STOs have the advantage of producing the required cusp behavior as well as the appropriate long-range decay of the wavefunction. Using these, high-quality basis sets can be constructed using a relatively small number of functions. The TZ2P basis set is used in this thesis to represent the electron wavefunctions located at the atomic sites of the clusters.

2.6.2 Frozen Core

To speed up the computational time, frozen cores are employed to minimize the extent the basis set is used.[54] The deep-core atomic orbitals of a system do not change significantly once chemical bonding has occurred, and they are represented by a total charge density and core potential. This charge density ignores the slight change in deep-core orbitals once the chemical bonds have formed. A total charge density and potential is also derived for the valence orbitals, as to match the orthogonality between the core and the valence basis functions used in the SCF equations. This is achieved by adding a series of auxiliary "core functions" to the valence function; precisely one for each frozen core orbital. This is represented by a linear combination of core orbitals where the valence orbitals are expressed as,

$$\chi_v^{valence} \Rightarrow \chi_v^{valence} + \sum_\mu c_{\mu,v} \chi_\mu^{core}$$

where χ_μ^{core} is the auxiliary core function, $\chi_v^{valence}$ is the valence function, and $c_{\mu,v}$ is a coefficient determined by condition that the modified valence function is orthogonal to each frozen core orbital.[54] The orbitals that make up the frozen core are determined by very accurate single-atom calculations using large STO basis sets.

2.6.3 ZORA

To handle the relativistic effects of the systems studied, the zero-order regular approximation (ZORA) was employed.[58–61] By rewriting the energy expression and expanding in the parameter $E/(2mc^2 - V)$, which remains small even close to the nucleus, the zeroth order term is found to be,

$$E = \frac{p^2 c^2}{2mc^2 - V} + V$$

Therefore, retaining only the zeroth order term the ZORA Hamiltonian takes the form,

$$H_{zora} = \sum_i p_i \frac{c^2}{2mc^2 - V} p_i + \frac{mc^2}{(2mc^2 - V)^2} \sigma \cdot (\nabla V \times \bar{p}) + V$$

This Hamiltonian operates on the corresponding eigenstates of the system, and the relativistic effects experienced by the electrons are accounted for.

Chapter 3

Experimental Methods

3.1 Mass Spectrometry

Since the dawn of cluster science, mass spectrometry has been employed to understand the stability of clusters produced in gas phase. This analytical method generates ionized clusters and measures the relative abundances of clusters produced in gas phase by calculating a mass to charge ratio. There are many different techniques employed to generate these clusters; however generally this goal is achieved by hitting a source target with a laser, where the source target is tailored to fit the experiment. The few common source target procedures are seeded supersonic nozzle sources, laser vaporization sources, liquid-metal ion sources, and ion sputtering sources.[62] Each technique produces extremely small fragments consisting of a few atoms that are jettisoned off the source target and are directed down a collimation chamber using an ion gun or inert gas, i.e. helium. These fragments are then ionized and accelerated down the chamber where a magnetic bottle neck bends the trajectory of the clusters. The trajectory of the cluster will depend on the mass of the cluster, which eventually hits a detector. The mass to charge ratio is subsequently determined by the time of flight. A schematic of the apparatus at Penn State used for the experimental methods of Chapter 4 can been seen as Figure 3.1.[63] Once a mass to charge

distribution has been obtained, etchants (oxygen, methanol, etc) can be introduced into the system. By comparing the distinct peaks in the mass spectrum before and after etching, the stability of the clusters can be probed.
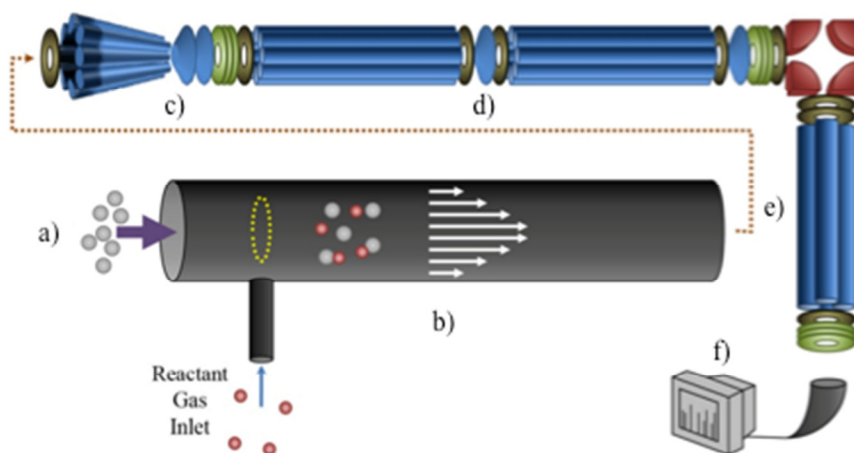
Figure 3.1. A general schematic diagram of the mass spectrometer used in the experimental section of this thesis.[63] a) Cluster Source, b) Fast Flow Reactor, c) Collisional Focusing Conical Octopole, d) Differential Pumping, e) Quadrupole Mass Spectrometer, and f) Ion Current Detector

Chapter 4

What Determines if a Ligand Activates or Passivates a Superatom Cluster?

In this chapter, the role of how ligands affect the reactivity of clusters is investigated in detail.[64] Ligands such as thiols, phosphines, and halides surrounding the metallic core are usually used to withdraw electrons from the metal cluster leading to a delocalized electron count that corresponds to a filled electronic shell and are used as passivating and protecting groups.[4–7,65–67] Ligand protected metal clusters synthesized via wet chemistry have also generated extensive interest, and the stability of these ligated clusters are also explained using the superatom concept.[3,65,66,68,69] Several aluminum based cluster assembled materials have been synthesized including those based on Al_{77}[5] and icosahedral Al_{12}[70–74] motifs. Al_{77} is particularly interesting as the cluster has a highly spherical shape and an odd number of electrons, and does not have a closed electronic shell. The fact that it forms a material implies that electronic shell closure is not the only criteria for material assembly. As described in Section 4.5, we show that the selective positioning of the ligands can be used to distort the charge density over the surface of the aluminum cluster resulting in active sites.[75] The addition of a ligand can therefore protect a cluster enhancing stability or make it more reactive. The question is under what circumstances do ligands passivate or activate a superatom cluster?

We have performed a synergistic experimental (Penn State) and theoretical (VCU) study of the etching of $Al_nI_m^-$ clusters with methanol. Due to its clean etching spectrum, and because its vapor pressure is higher than water, methanol was chosen as the etchant. The cluster reaction experiments were conducted in a fast flow reactor, and theoretical studies of the reactivity and active sites of $Al_nI_m^-$ were emphasized for n = 7-14 and m = 0-2 using DFT. We have identified four superatom clusters in this size regime with closed electronic shells, Al_{13}^-, $Al_{13}I_2^-$, $Al_7I_2^-$ and $Al_{14}I_3^-$. Al_{13}^- and $Al_{14}I_3^-$ have closed electronic shells corresponding to a $|1S^2 | 1P^6 | 1D^{10} 2S^2 | 1F^{14} 2P^6|$ configuration. $Al_7I_2^-$ has a closed shell of 20 valence electrons corresponding to a $| 1S^2 | 1P^6 | 1D^{10} 2S^2 |$ configuration. The stability of $Al_{13}I_2^-$ can be viewed in two ways. An analysis of the electronic orbitals indicates that the orbitals corresponding to $|1S^2 | 1P^6 | 1D^{10} 2S^2 | 1F^{14} 2P^6|$ are all occupied. A 2P delocalized orbital has a strong mixing with the Iodine atoms and one can also look upon the cluster within a picture of where each I removes one electron from the delocalized shell as described by Walter et. al.[3] In this picture, the electronic shells are described as $|1S^2 | 1P^6 | 1D^{10} 2S^2 | 1F^{14} 2P^4|$ with the 2P bonding orbital counted as a localized orbital. Regardless of the scheme used to describe the electronic profile of $Al_{13}I_2^-$ these complementary viewpoints both describe a cluster that has a large HOMO-LUMO gap, a spherical metal core, and an even distribution of electrons around the metallic core. Three of these four clusters are resistant to methanol etching; however, $Al_{14}I_3^-$ is reactive due to its activated adatom structure, where an aluminum atom with iodine lies on top of the icosahedral core. This activated adatom is found to serve as a Lewis acid site. The $Al_{13}I_m^-$ clusters (m = 0-3) and $Al_7I_2^-$ are unreactive with methanol because of their symmetric core and their even distribution of charges around the surface of the cluster. Iodine atoms may induce Lewis acid and Lewis base active sites on the opposite sides of the cluster, while balanced ligands tend to

passivate a cluster, demonstrating that the position of the iodine ligands may have a profound effect on the reactivity.

4.1 Aluminum Iodide Cluster Production and Reactivity

Theoretical and experimental efforts were undertaken to understand how a ligand will perturb the electronic profile and chemical stability of a cluster. A well-resolved mass spectrum of $Al_nI_m^-$ (7 < n < 37, m = 0-3) clusters was achieved by adding solid iodine into the laser vaporization (LaVa) source under a pressure of about ~20 Torr. To experimentally determine which how $Al_nI_m^-$ clusters react to methanol a mass spectrometer is employed. A well-resolved mass spectrum of $Al_nI_m^-$ (7 < n < 37, m = 0-3) clusters was generated by using a laser vaporization (LaVa) source,[76] made of stainless steel, with an external motor to control the target rotation of Al rod (Kurt J. Lesker, 99.999% purity, ϕ 6 mm), as well as a gas inlet connection to allow a constant flow of helium (Praxair, Inc., purity > 99.995%). Solid iodine (Sigma-Aldrich, 99.999%) was added in the LaVa-source container to form aluminum iodide clusters. The outlet expansion nozzle was made of a Teflon tube (~2.5 cm length) with an inner diameter of 0.32 cm. The pressure inside the source during operating conditions was kept at ~20 Torr, suggesting a Knudsen number of ~2.8 $\times 10^{-3}$ and a terminal Mach number of ~12.3. The helium buffer gas introduced from the inlet of the source carried the clusters through the nozzle into a flow tube where they encountered and reacted with methanol (Sigma-Aldrich, >99.9%) at room temperature. The reactant methanol gas was introduced in the cluster beam ~30 cm downstream from the source (resulting in thermalized $Al_nI_m^-$ clusters) and allowed to react with the clusters over a 60 cm distance and time of ~8 ms. The reaction products were extracted into a

differentially pumped ion guide vacuum system, and analyzed via a quadrupole mass spectrometer (Extrel QMS). The pressure in the reaction flow-tube was kept at ~0.7 Torr, i.e., several hundred collisions for the related reactions.

The $Al_nI_m^-$ clusters display a normal distribution centered at Al_{21}^-, except for Al_{13}^-, which exhibits slightly enhanced stability. Aluminum reacts with iodine at room temperature and the formed aluminum iodides mainly cover a range of $Al_nI_{1-3}^-$, with $Al_{13}I^-$ and $Al_{13}I_2^-$ as the most abundant. After the addition of methanol, the $Al_nI_m^-$ clusters begin to etch and the abundances undergo a dramatic change, as shown in Figure 4.1A-1B (for more details see Appendix, Figure A1, A2). Peaks corresponding to I^-, I_3^-, AlI_4^-, and I_5^- appear with enhanced intensities owing to the production of I^- in the etching reactions. This fragmentation is discussed in more detail in section 4.7 of the report. Most of the $Al_nI_m^-$ clusters with sizes larger than n = 13 disappear or display weakened intensities. Figure 4.1-2A, 4.1-2B, and 4.1-2C plot the intensities of $Al_nI_{0-2}^-$ clusters in the absence and presence of methanol. The intensities of Al_7I^-, Al_8I^-, $Al_8I_2^-$, Al_{13}^-, $Al_{13}I_2^-$ and $Al_{13}I_4^-$ are increased up to twice their nascent peaks. $Al_7I_2^-$, $Al_{20}I^-$, $Al_{13}I^-$, and $Al_{13}I_3^-$ display similar intensities before and after methanol etching. It is interesting to note that $Al_{13}I^-$ and $Al_{13}I_3^-$ have an odd number of electrons, which confirms that a closed electronic shell is not necessary for a cluster to be resistant to methanol etching. $Al_{14}I_3^-$ was previously found to be resistant to oxygen etching,[31] however the abundance of $Al_{14}I_3^-$ is almost completely depleted after methanol is introduced to the flow tube. Seen from Figure 4.1-2A, 4.1-2B and 4.1-2C, Al_7I^- and $Al_7I_2^-$ have higher abundances after methanol etching, while Al_7^- has a rather low abundance both before and after methanol etching. The addition of iodine on Al_7 (forming $Al_7I_{1,2}^-$) stabilizes the cluster with respect to methanol etching. On the other

hand, Al_{11}^- is resistant to methanol etching, while $Al_{11}I^-$ and $Al_{11}I_2^-$ are etched away by methanol, showing that the addition of iodine may sometimes activate a cluster.
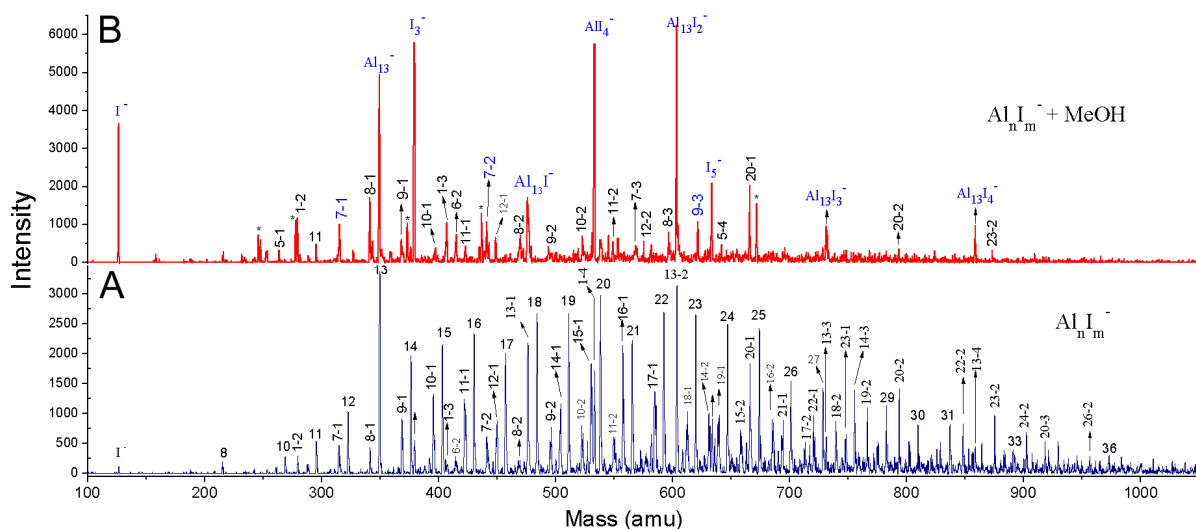

Figure 4.1-1. The reactivity of $Al_nI_m^-$ clusters with MeOH. **A,** The nascent mass spectrum of $Al_nI_m^-$ clusters. **B,** The spectrum of $Al_nI_m^-$ clusters after methanol etching. A few peaks marked with * refer to $Al_n(CH_3OH)_m^-$.
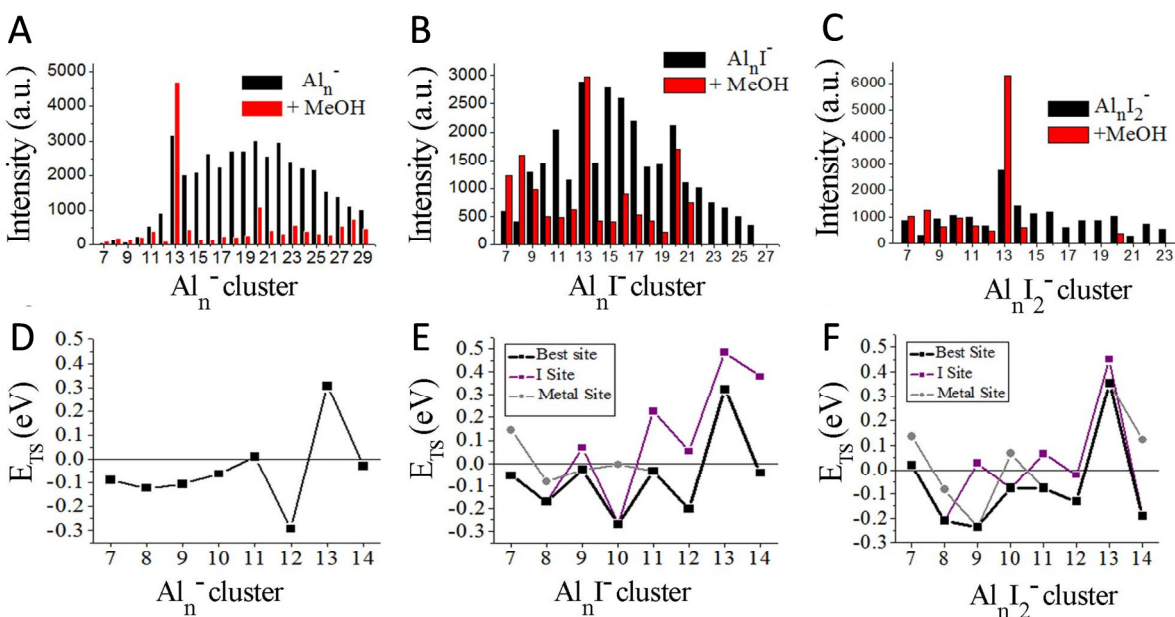

Figure 4.1-2. Ionic intensities and transition state energies (E_{TS}). A/B/C, The experimental ionic intensities of Al_n^-, Al_nI^-, and $Al_nI_2^-$ at the absence and presence of methanol, where the intensity values correspond to the integral areas of the correlated peaks of Figure 4.1-2. **D/E/F,** The calculated E_{TS} for the cleavage of the O-H bond of methanol for Al_n^-, Al_nI^-, and $Al_nI_2^-$.

36

4.2 Structures and Electronic Properties of $Al_nI_m^-$ (n = 7-14 and m = 1-3)

The lowest ground state isomers for $Al_nI_m^-$ (n = 7-14 and m = 1-3) are shown below. Each cluster was optimized without constraint and was given full vibrational freedom. The HOMO-LUMO gaps and both aluminum and iodine binding energies are also provided.
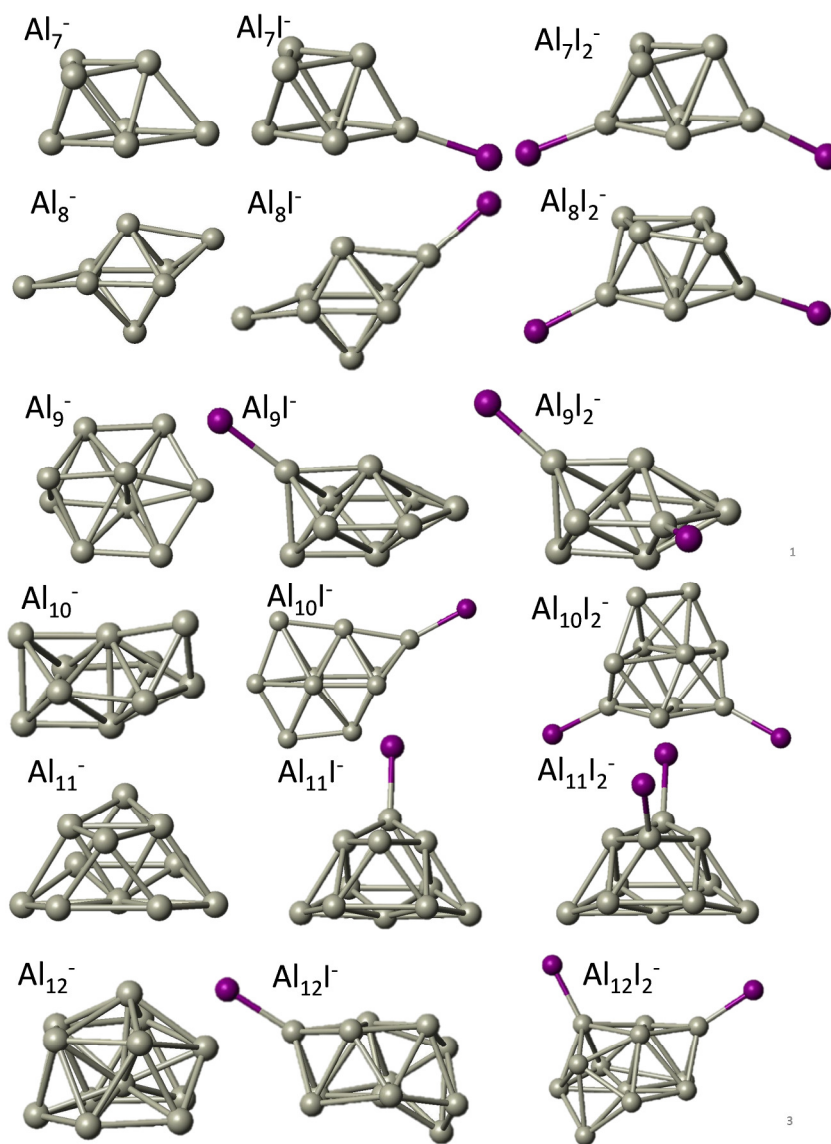
Figure 4.2-1. The optimized lowest-energy structures of $Al_{7-12}I_{0-2}^-$.
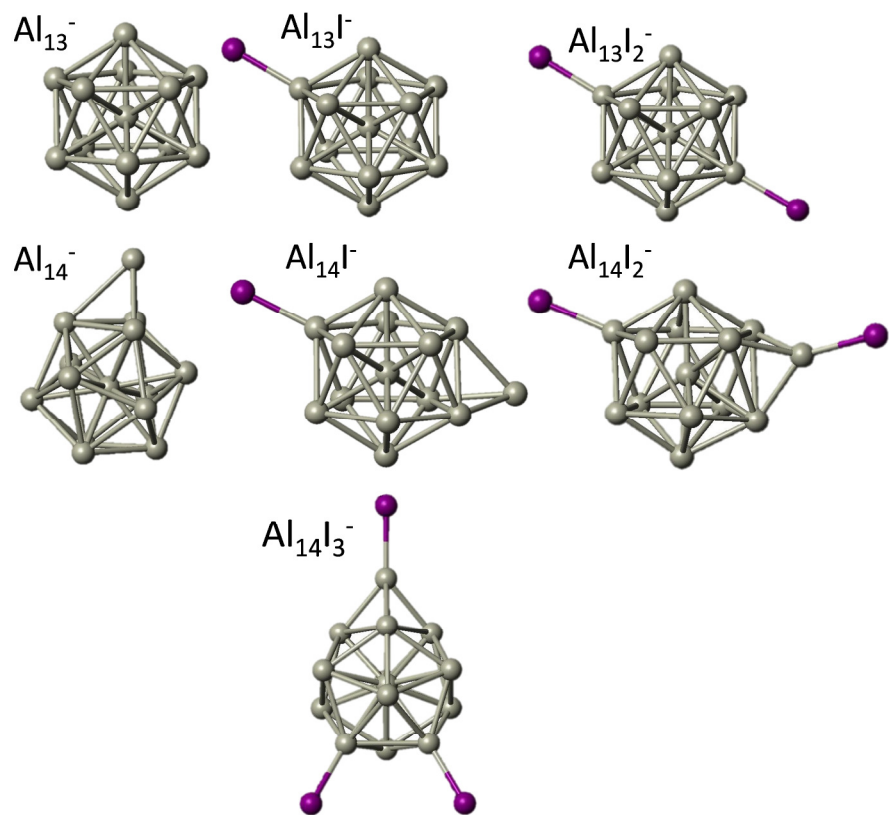
Figure 4.2-2. The lowest-energy structures of $Al_{13,14}I_{0-3}^{-}$.
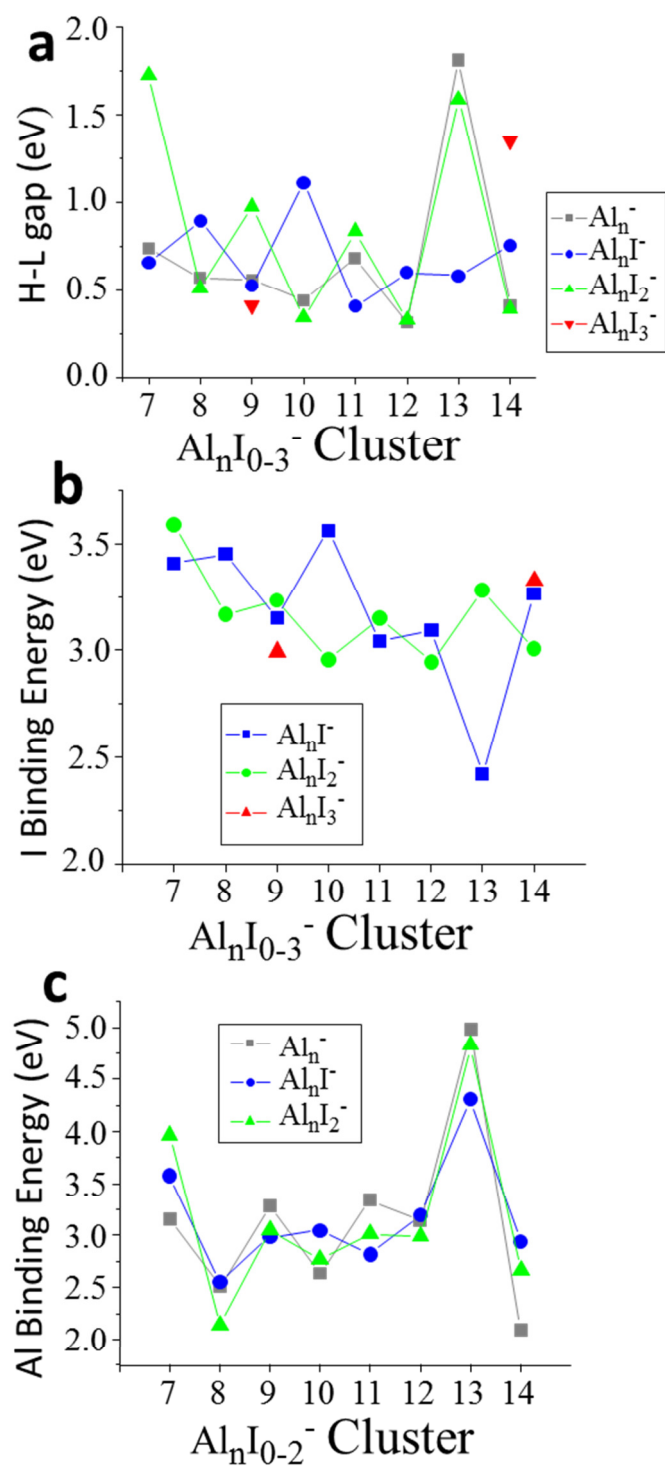
Figure 4.2-3. Binding energy and HOMO-LUMO gaps. A, The HOMO-LUMO gaps of $Al_nI_m^-$. B, Iodine binding energies of $Al_nI_m^-$ clusters. C, Aluminum binding energies for $Al_nI_{0-2}^-$. n = 7-14, m = 0-2.

4.3 Linear Transit Method

The theoretical reactivity values were calculated by using the linear transit approach, and the transition state energy was found (E_{TS}). The transition state energy was used because the energy to cleave the O-H bond is less than the energy required for desorption of the molecule. Once we had obtained the lowest energy isomers for $Al_nI_{0-2}^-$ (n = 7-14), $Al_9I_3^-$, and $Al_{14}I_3^-$, a methanol atom was positioned at various sites on each cluster. The O-H bond distance was set over a range of distances, until a saddle point was found. This process allowed us to determine the binding energy of the methanol and the transition state energy. Once the O-H bond has been stretched, the cluster was allowed full vibrational freedom and the final energy of the cluster was obtained. To investigate exactly how a ligand will activate or passive a superatom cluster, the linear transit approach was preformed on both aluminum-aluminum sites and aluminum-iodine sites, and an energetic minimum was obtained for each. Specific information regarding the use of E_{TS} is provided in the next section. A schematic of the process is shown below in Figure 4.3.
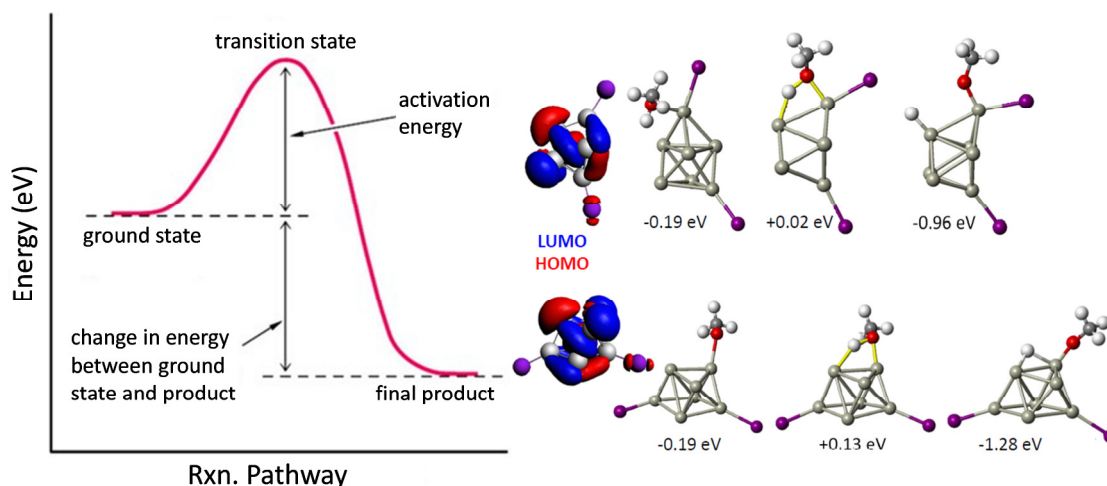
Figure 4.3. A schematic of the reaction pathway used in this thesis is provided. The placement of the methanol on a metal-metal and aluminum-iodine site is also provided. The HOMO and LUMO isosurfaces of $Al_7I_2^-$, and the binding energy, transition state energy and final state energy for the reaction of methanol with $Al_7I_2^-$ at the I site (top), and metal site (bottom).

4.4 Observed Etching and Reactivity of Clusters

To understand the mechanism by which these clusters react with methanol, we have investigated the lowest energy structures for $Al_nI_{0-2}^-$ (n = 7-14), and also $Al_9I_3^-$ and $Al_{14}I_3^-$. Their respective HOMO-LUMO gaps and the binding energies of both the aluminum and iodine, have been plotted and can be seen in Figure 4.2-3. Several clusters we found to have HOMO-LUMO gaps that are large enough that the cluster may be considered to have a closed electronic shell. For example, $Al_7I_2^-$ has a gap of 1.73 eV; Al_{13}^- and $Al_{13}I_2^-$ have gaps of 1.81 eV and 1.59 eV respectively, and $Al_{14}I_3^-$ has a gap of 1.35 eV. Previous studies have indicated that clusters with HOMO-LUMO gaps higher than 1.2 eV are generally non-reactive towards oxygen.[19] To understand the reactivity with methanol, we have calculated the lowest energy transition state for the breaking of the O-H bond on the cluster's surface, as graphed them in Figure 4.1-2D-F, for Al_n^-, Al_nI^-, and $Al_nI_2^-$, respectively.

Figure 4.1-2D shows the transition state energy, E_{TS}, for the Al_n^- clusters. We have used the E_{TS}, as shown in Eq.1, as a measure of the reactivity in the gas phase. The reaction will proceed rapidly when the E_{TS} is negative, and the reaction will proceed slowly when the E_{TS} is positive.

$$E_{TS} = E (Al_nI_m^- (CH_3O\text{-}H)_{TS}) - E (CH_3OH) - E(Al_nI_m^-) \tag{1}$$

We have plotted the lowest energy transition state for each cluster at a metal site in which the oxygen of methanol is bound to an unprotected aluminum atom, as well as the iodine site corresponding to an aluminum atom that is bound to an iodine atom. Al_{11}^- and Al_{13}^- are both found to have positive E_{TS} values, which is consistent with the experimental findings that Al_{13}^- increases in intensity and Al_{11}^- shows resistance to reactivity. The remaining clusters n = 7-14

all show minimal abundance after methanol etching. For the Al_nI^- series in Figure 2B and 2E, we find only $Al_{13}I^-$ has a positive E_{TS}, and $Al_{13}I^-$ is experimentally the most abundant species in the series. The experimental results also find that Al_7I^- and Al_8I^- have an increased abundance, while theory finds them to be reactive. These clusters are likely products of the fragmentation of larger clusters, therefore determining exactly how reactive they are in experiments is difficult. For the $Al_nI_2^-$ series in Figure 4.1-2C and 4.1-2F, theory finds that $Al_7I_2^-$, and $Al_{13}I_2^-$ have positive E_{TS}, which is consistent with the experimental results by noting that $Al_{13}I_2^-$ is by far the most abundant cluster in this series while $Al_7I_2^-$ is the third most abundant.

We will now examine the reactivity of the $Al_{13}I_m^-$ superatomic clusters with methanol. Figure 4.4A shows the reaction pathway for Al_{13}^- with methanol, which is plotted below. Al_{13}^- has a closed electronic shell and an icosahedral geometric structure. The LUMO orbitals are plotted in blue, and the HOMO orbitals are plotted in red. The closed electronic shell demonstrates that the frontier orbitals are evenly distributed over the surface of the cluster, preventing the presence of active sites. The oxygen atom of methanol does not readily bind to the cluster, demonstrating that Al_{13}^- is not a good Lewis acid. The E_{TS} is 0.31 eV indicating that the reaction will proceed slowly. The addition of iodine results in $Al_{13}I^-$ having a Lewis base site, which appears on the opposite side of the cluster as the iodine ligand site, while the LUMO density is evenly distributed over the surface of the metal cluster. The E_{TS} of $Al_{13}I^-$ is 0.32 eV, indicating that $Al_{13}I^-$ will also be resistant to methanol etching. When we investigate the cleavage of the O-H bond at the iodine site, we find that the E_{TS} increases to 0.49 eV. This provides further evidence that the addition of iodine fails to activate the Al_{13}^- cluster. The reason for this is that the Lewis acidity of the $Al_{13}I^-$ cluster is still poor because the induced active site is half filled and cannot serve as a Lewis acid. The reaction of $Al_{13}I_2^-$ is shown in

42

Figure 4.4C, and the E_{TS} is found to be 0.35 eV. The two iodine atoms lie on opposite sides of the cluster, quenching each other's induced active sites. Furthermore, $Al_{13}I_2^-$ remains a poor Lewis acid, with the LUMO charge density evenly distributed over the icosahedral core of the cluster. It can be concluded that the addition of iodine to Al_{13}^- maintains the pure cluster's resistance to reaction with methanol because the cluster remains a poor Lewis acid due to its icosahedral closed geometric shell. This hypothesis is confirmed by the high abundance of the $Al_{13}I^-$, and $Al_{13}I_2^-$ in the experiment after exposure to methanol.
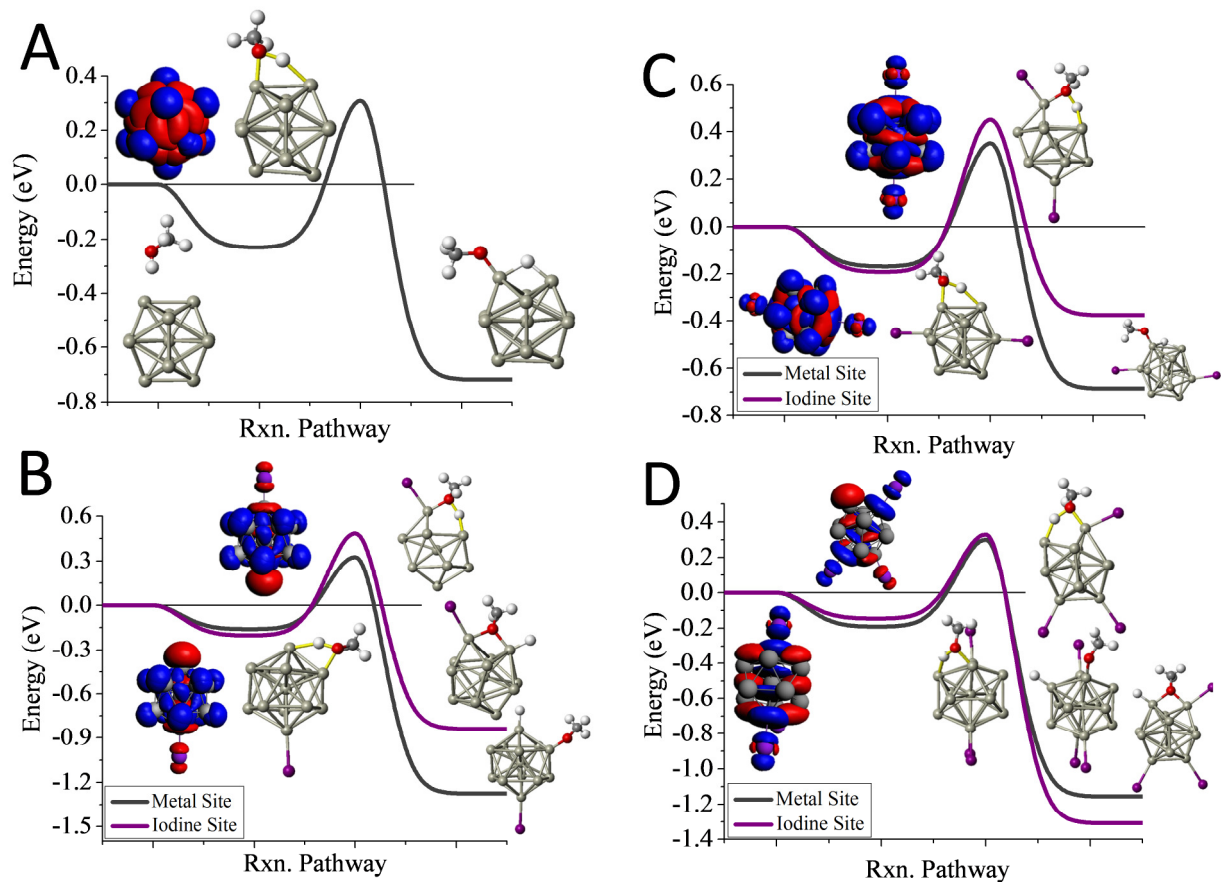
Figure 4.4. The reaction pathways of $Al_{13}I_{0-3}^-$ + MeOH are provided above. A) Al_{13}^-, B) $Al_{13}I^-$, C) $Al_{13}I_2^-$. The red indicates the HOMO or near HOMO orbitals for degenerate orbitals, and Blue indicates LUMO or LUMO+1 orbitals that are fully unoccupied.

4.5 Selective Ligand Position

To highlight how the position of a ligand determines if a cluster will be reactive or not, a few examples are considered in the following sections. In section 4.5.1 multiple close lying isomers of $Al_9I_3^-$ are studied. Each isomer has the same metal core structure, however there are slight variations in the arrangement of the iodine ligands. In section 4.5.2, an isomer of $Al_{13}I_2^-$ is studied, which is denoted as $*Al_{13}I_2^-$. As discussed in the Section 4.4, the ground state geometry of $Al_{13}I_2^-$ has the iodine positioned on opposite sides of the metal core, which provides an even charge distribution and subsequently quenches the induced active sites produced by the iodine. However, in this section we consider when the iodine atoms are positioned adjacent to each other, which offers a significant variation in the energetic behavior of the cluster. The selective positioning of the iodine ligands can result in completely different electronic structures, the consequences of which are explained in the following sections.

4.5.1 Reactivity of $Al_9I_3^-$

One of the puzzles of the experimental mass spectra is the relatively large abundance of $Al_9I_3^-$ after methanol etching. Our investigations lead to 3 isomers, the ground state structure, and two structures with different iodine positions that are 0.03 eV and 0.06 eV higher in energy. As shown in Figure 4.5.1, we have also investigated the reaction pathway of the three lowest energy isomers of $Al_9I_3^-$. The lowest energy structure of $Al_9I_3^-$, isomer A in Figure 4.5.1, has two adjacent iodine atoms located on the octahedral core, and a third located perpendicular to the first two iodines. A Lewis acid site is found on the opposite side of the cluster as the third iodine atom, and the E_{TS} is -0.16 eV, showing that with unbalanced iodine atoms, the cluster is reactive.

A second isomer, B in Figure 4.5.1, has balanced ligands and lies 0.03 eV higher in energy than the ground state isomer. With the balanced ligands, the transition state for the O-H bond cleavage is only -0.02 eV, less than the energy of the reactants. This transition state is relatively high in energy making it likely to show some resistance to methanol etching. The relatively high abundance of the $Al_9I_3^-$ cluster is due to this isomer having some resistance to methanol etching. A third isomer C possesses unbalanced ligands and has a transition state energy of -0.03 eV. This may also contribute to the observed abundance. All three isomers contain isostructural metallic cores; however, variations in the precise positioning of the iodine ligand can result in dramatic variations of a cluster's reactivity.
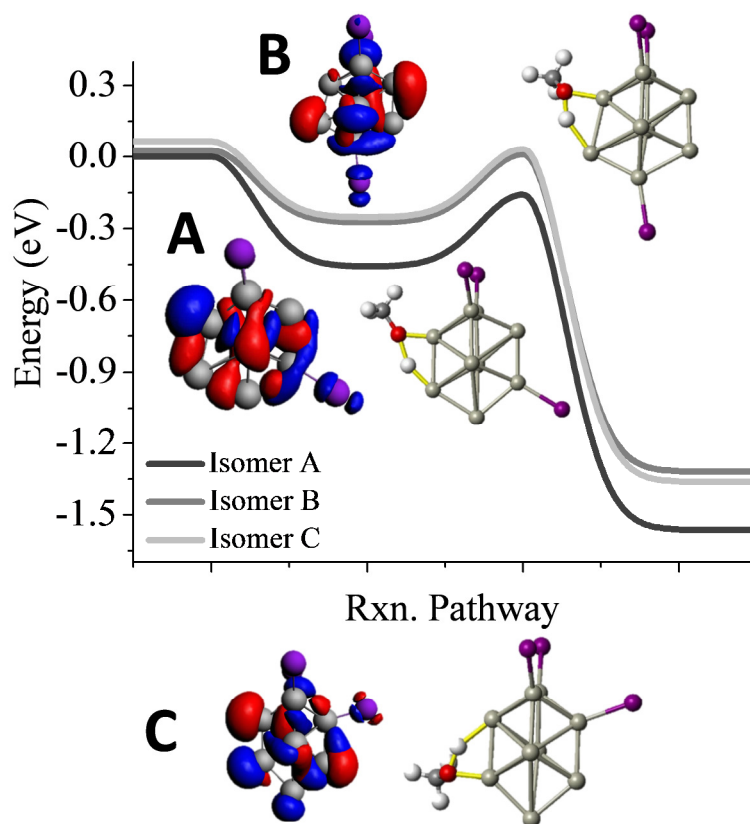
Figure 4.5.1. $Al_9I_3^-$ reactivity. Reaction pathway for the three lowest energy isomers of $Al_9I_3^-$ (A/B/C). The red indicates the HOMO, and the blue indicates LUMO+1. Rxn. Pathway is abbreviated for cluster reaction coordinate and pathway.

4.5.2 Reactivity of $*Al_{13}I_2^-$

To investigate how ligands can be used to distort the charge density of a cluster with a spherical geometry, an isomer of $Al_{13}I_2^-$ is considered. This isomer has iodine ligands positioned adjacent to each other and will be expressed as $*Al_{13}I_2^-$. When electronegative ligands are positioned in such a manner, a complimentary active site is induced on the opposite side of the cluster. As shown in Figure 4.5.2, the cluster is highly reactive and has an E_{TS} of -0.32 eV. The large increase in methanol binding energy, -0.67 eV, is a hallmark of the Lewis acidity of this cluster, and indicates how readily the Lewis acid site accepts a pair of electrons from the oxygen. The adjacent arrangement of the iodine atoms results in a much lower HOMO-LUMO gap of only 0.70 eV. This further demonstrates how unbalanced ligands can change the electronic structure of a cluster, which subsequently alters its reactivity with polar solvents such as methanol.
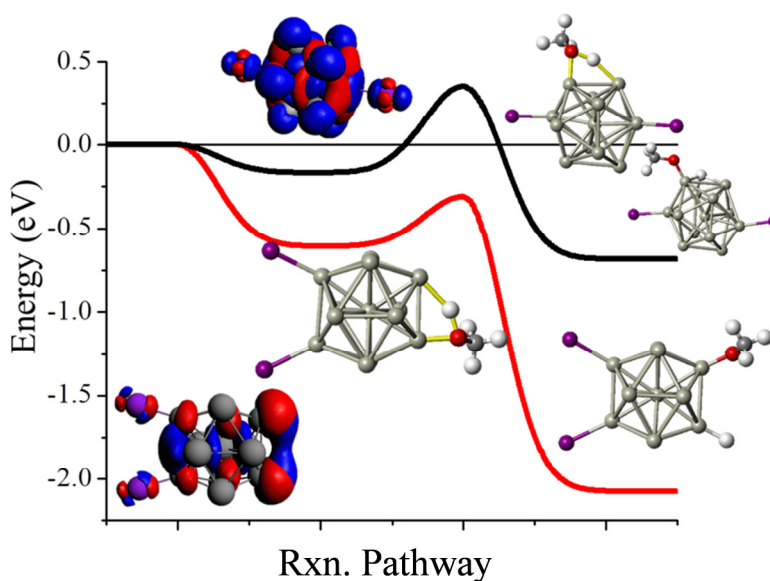
Figure 4.5.2. $Al_{13}I_2^-$ and $*Al_{13}I_2^-$ reaction pathways. The reaction pathway for both the ground state and isomer are provided for comparison. The red indicates the HOMO, and the blue indicates LUMO. Rxn. Pathway is abbreviated for cluster reaction coordinate and pathway. The red line is the reaction pathway for the adjacent iodine $*Al_{13}I_2^-$ and the black line represents the pathway for $Al_{13}I_2^-$.

4.6 Geometric Effects on Reactivity

Previous studies have shown how the geometry of a cluster can perturb its energetics, and the results presented in this report have found a similar pattern. Not only was it found that the geometric structure of a cluster plays an important role in determining the reactivity, but the attachment of a ligand at the unsymmetrical geometric site or adatom could actually enhance the reactivity of the cluster. To highlight this, the reactivity patterns of $Al_{14}I_{0-3}^-$ and $Al_7I_{0-2}^-$ are discussed below.

4.6.1 Reactivity of $Al_{14}I_{0-3}^-$

The reaction pathway of $Al_{14}I^-$ with methanol is shown in Figure 4.6.1D. The structure has an Al_{14} core with a 13-atom icosahedral structure with the 14th atom an adatom, where the iodine atom is bound to the site opposite the adatom. The frontier orbitals reveal a Lewis acid/ Lewis base complementary active site adjacent to the iodine atom on the cluster. The lowest energy transition state is located at the complementary active site, and E_{TS} is -0.04 eV, implying a fast reaction with methanol. The lowest energy transition state at the icosahedral iodine site is found to be unreactive, with a transition state energy of 0.38 eV greater than the reactants.

$Al_{14}I_2^-$ has a metallic core with a 13-atom icosahedron and an adatom, with one iodine bound to the adatom and another to an Al atom on the opposite side of the cluster. The E_{TS} at the iodine site is -0.19 eV, indicating that the cluster reacts rapidly, as shown by Figure 4.6.1E. The lowest energy transition state at the metal site is +0.12 eV, suggesting that the cluster will only react at the adatom iodine site. The electronic structure reveals that a low-lying LUMO+3 orbital is localized on the adatom and can serve as a Lewis acid site. $Al_{14}I_3^-$ has a similar geometry as

$Al_{14}I_2^-$, with the third iodine atom added at a second icosahedral aluminum atom opposite the adatom. The E_{TS} at the iodine site is -0.12 eV, indicating that the cluster should react rapidly with methanol, shown in Figure 4.6.1F. The E_{TS} at the metal site is +0.30 eV, revealing that $Al_{14}I_3^-$ will only react at the adatom site. The methanol will react rapidly at the ligand activated adatom sites of $Al_{14}I_2^-$ and $Al_{14}I_3^-$ while being slow to react at the metal sites. This is confirmed by the nearly complete etching of $Al_{14}I_2^-$ and $Al_{14}I_3^-$ in the experimental mass spectrum.
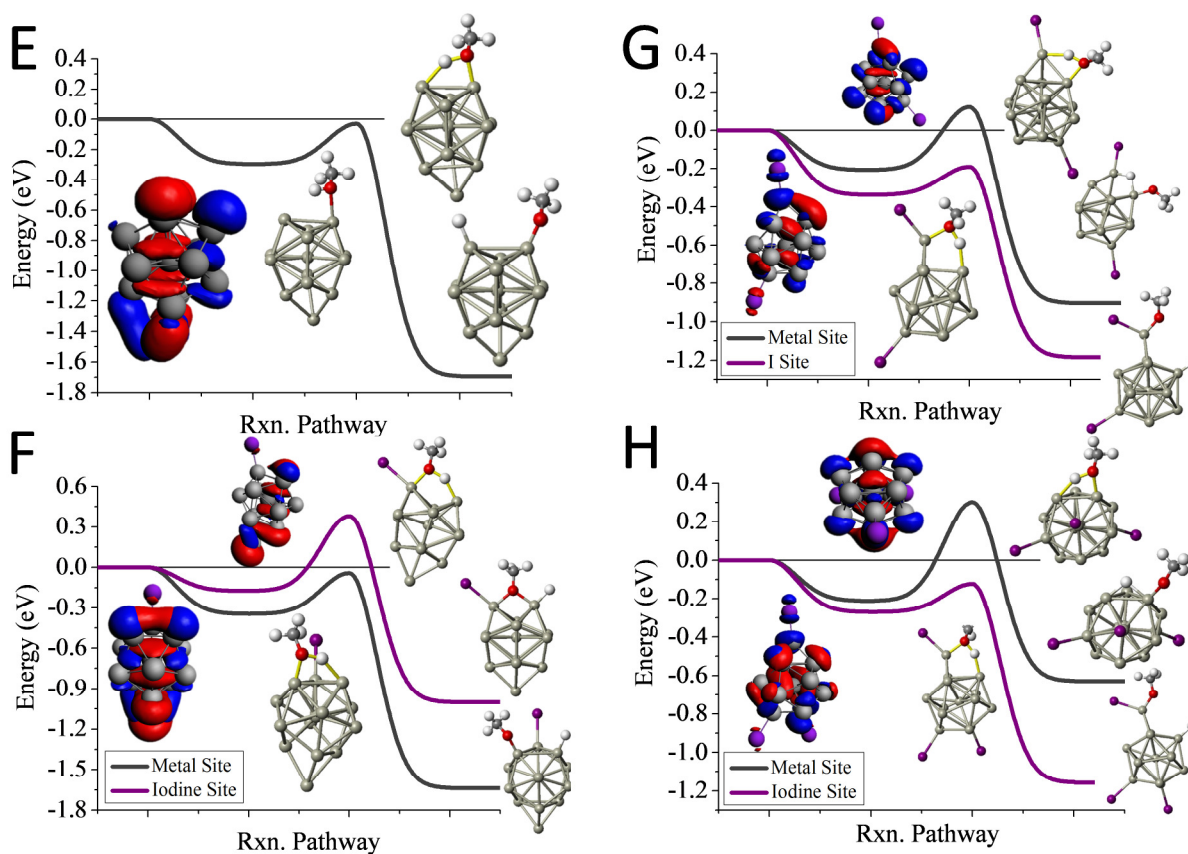
Figure 4.6.1. The reaction pathways of $Al_{14}I_{0-3}^-$. + MeOH are provided above. E) Al_{14}^-, F) $Al_{14}I^-$, G) $Al_{14}I_2^-$, H) $Al_{14}I_3^-$. The red indicates the HOMO or near HOMO orbitals for degenerate orbitals, and Blue indicates LUMO or LUMO+1 orbitals that are fully unoccupied.

4.6.2 Reactivity of $Al_7I_{0-2}^-$

To further understand how a ligand will enhance or diminish the geometric perturbations of a cluster as it gains a closed electronic shell, we investigate the $Al_7I_{0-2}^-$ clusters. Al_7^- is shown in Figure 4.6.2A, and reacts readily with methanol in experiments and has an E_{TS} of -0.09 eV. The structure of Al_7^- is an octahedron with an adatom. The frontier orbitals indicate that the Al atoms on the opposite side of the adatom may serve as complementary active sites. In Al_7I^- the iodine atom adds to the Al adatom site, and the resulting activated adatom has a transition state energy of -0.05 eV, indicating that the cluster should react with methanol, as shown in Figure 4.6.2B. The metal site has the lowest energy transition state of +0.14 eV, indicating that the addition of iodine has passivated the cluster's metallic core.

$Al_7I_2^-$ is passivated with respect to methanol etching, with two iodine atoms on opposite sides of the cluster. The E_{TS} at the iodine site is +0.02 eV, greater than the energy of the reactants (Fig. 4.6.2C). The transition state at the most reactive metal site is +0.13 eV indicating that the metal core is also passivated. The $Al_7I_2^-$ cluster still maintains its adatom-like geometry, however the addition of a second iodine ligand to balance out the first ligand increases the energy of the orbital localized on the adatom site, making the cluster less reactive. The relatively large abundance of $Al_7I_2^-$, paired with the low abundance of Al_7^- after methanol etching confirms our analysis. The reaction pathways for $Al_7I_{0-2}^-$ + MeOH in Figure 4.6.2 can be seen below.
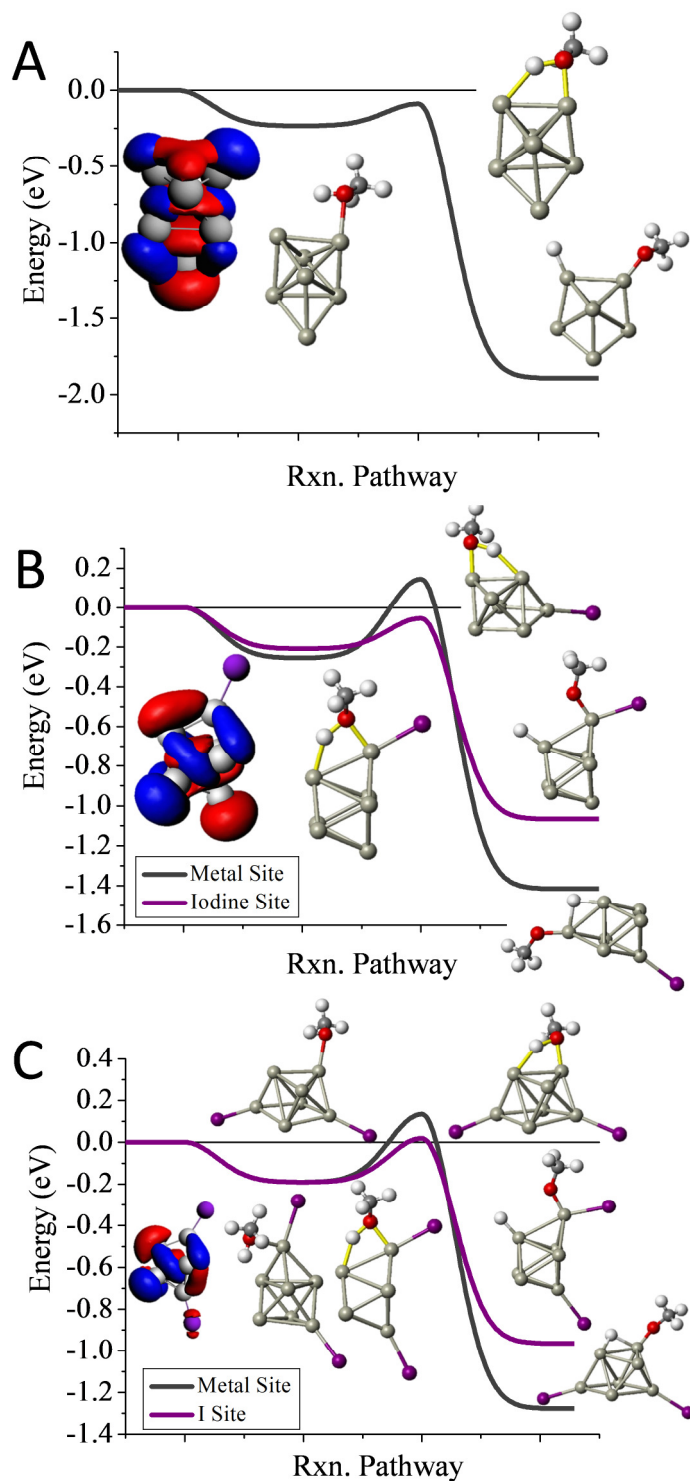
Figure 4.6.2. The reaction pathways of $Al_7I_{0-2}{}^-$ with MeOH. The calculated reaction pathways for A) $Al_7{}^-$, B) Al_7I^-, and C) $Al_7I_2{}^-$ with MeOH. The red indicates the HOMO or near HOMO orbitals for degenerate orbitals, and Blue indicates LUMO or LUMO+1 orbitals that are fully unoccupied. Rxn. Pathway is abbreviated for cluster reaction coordinate and pathway.

4.7 Fragmentation

The fragmentation channels of $Al_nI_m^-$ after methanol etching are examined in this section. Experimentally, we see three prominent features, i) a decrease in the size distribution of the clusters, ii) the abundance of I^-, I_3^-, I_5^-, and AlI_4^- all dramatically increase after the methanol etching, and iii) there is little abundance of aluminum clusters with methoxy, $Al_nOCH_3^-$. The calculated energies are shown in Figure 4.7 in which positive energies correspond to an endothermic reaction, and negative energies correspond to an exothermic reaction. For Al_n^-, the loss of $AlOCH_3$ is the energetically most favorable pathway and is exothermic in several cases, as seen in Eq. 2.

$$Al_n^- + CH_3OH \rightarrow Al_{n-1}H^- + AlOCH_3 \tag{2}$$

This equation suggests that some of the smaller clusters seen after etching may be HAl_n^-. For $Al_nI_m^-$, the loss of I^- is a likely channel, as the methoxy often favors binding to an I site, and this will inhibit the loss of $AlOCH_3$.

$$Al_nI_m^- + CH_3OH \rightarrow HAl_nI_{m-1}OCH_3 + I^- \tag{3}$$
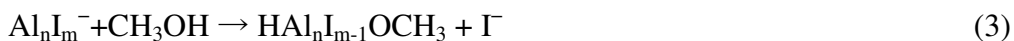
I^- loss is endothermic; however, our previous studies indicate that up to 4 methanol molecules[27] could attach to an aluminum cluster which would generate enough energy to neutralize the cluster and release I^-.
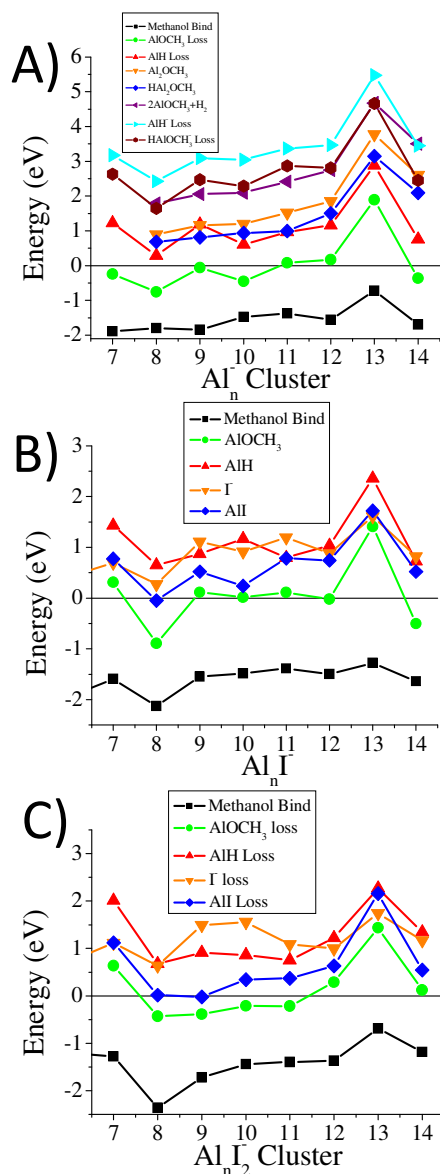
Figure 4.7. The calculated reaction energy for the dissociative binding of methanol, and the dissociative binding of methanol followed by the loss of the fragment given in the legend. A negative implies that the reaction is exothermic. The reactions are as follows:

$$Al_n^- + CH_3OH \rightarrow Al_{n-1}H^- + AlOCH_3 \qquad (1)$$
$$Al_n^- + CH_3OH \rightarrow Al_{n-1}HOCH_3^- + AlH \qquad (2)$$
$$Al_n^- + CH_3OH \rightarrow Al_{n-2}H^- + Al_2OCH_3 \qquad (3)$$
$$Al_n^- + CH_3OH \rightarrow Al_{n-2}^- + HAl_2OCH_3 \qquad (4)$$
$$Al_n^- + 2CH_3OH \rightarrow Al_{n-2}^- + 2AlOCH_3 + H_2 \qquad (5)$$
$$Al_n^- + CH_3OH \rightarrow Al_{n-1}OCH_3 + AlH^- \qquad (6)$$
$$Al_n^- + CH_3OH \rightarrow Al_{n-1} + HAlOCH_3^- \qquad (7)$$
$$Al_nI^- + CH_3OH \rightarrow HAl_nOCH_3 + I^- \qquad (8)$$
$$Al_nI^- + CH_3OH \rightarrow HAl_{n-1}OCH_3^- + AlI \qquad (9)$$

52
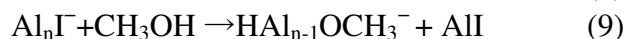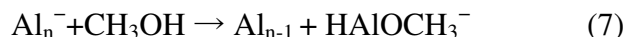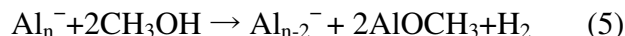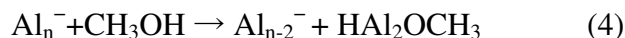
4.8 Conclusions

The addition of iodine ligands to aluminum superatoms may activate or passivate a cluster. To minimize the reactivity of a ligand-protected cluster, the metallic core should have a closed geometric shell with an even distribution of charges around the surface. Secondly, the ligands are most passivating when they are located in a balanced position on opposite sides of the metallic core. $Al_{14}I_3^-$ is found to have a closed electronic shell, however because the metallic core has an adatom site with an iodine atom, the cluster is activated with respect to methanol. $Al_{13}I_2^-$ has an icosahedral core with no adatom and balanced ligands, and is passivated to methanol. The position of the iodine may induce an active site on the opposite side of the cluster; $Al_9I_3^-$ is reactive when the iodine atoms are unbalanced, however when the three iodine atoms are balanced on opposite sides of the cluster, the cluster is passivated. Our work demonstrates that structural features are just as important as electronic shell closure, or even more important when the synthesis is done in an oxygen-free environment. To highlight this point, $Al_{50}Cp_{12}$ is a prominent example of a cluster that is remarkably stable under an inert atmosphere and can be isolated as atomic-precise clusters. This cluster has the hallmarks of stability with a spherical metallic core and balanced ligands. However, the HOMO–LUMO gap of this cluster is only 0.85 eV, and so it is quite reactive when exposed to O_2.[77] This work demonstrates that even if a cluster is protected by ligands, the cluster could be reactive when the geometric considerations are not met, revealing the dual roles of electronic structure and geometric structure on the stability of bare and ligand-protected nanoparticles.

Chapter 5

Magnetic Spin Moments and Stability of Bimetallic

Transition Metal Clusters:

VCu_n^+, VAg_n^+, VAu_n^+ (n = 2-14)

Understanding the manner in which localized magnetic spin states couple to their surroundings is of great importance and has garnered significant attention in recent years.[8,11,13,39,41,78–81] Studies on VAg_n^+ clusters have shown that the vanadium atoms undergo a transition in valence as the cluster grows in size, which corresponds to the symmetry of the delocalized orbital.[8] The stability of these clusters follow a shell-filling scheme depending on whether the geometry of the cluster is 2D or 3D, and the number of delocalized electrons the continuant atoms provide. It was discovered that the first shell closure occurs at VAg_5^+, which has 9 valence electrons, 6 filling the $1S^2$, $1P_x^2$, and $1P_y^2$ delocalized shells, while 3 are localized on the vanadium atom. The second shell closure transpires at VAg_7^+, which has 8 delocalized electrons and 3 localized $3d$ vanadium states. At VAg_{14}^+ there are 18 delocalized electrons and the vanadium atom is fully participating in hybridized bonding with the silver atoms. The nature of the valence transition and the split shell stability scheme provided greater insight into the under lying stability of transition metal clusters with magnetic impurities. Other studies have

shown that a magnetic impurity will interact differently depending on the chemical profile of the atoms that surround the dopant. Therefore, by varying the electronic structure of the host material, different properties can be realized.[82–84] In this chapter we consider the circumstance when a vanadium atom, with electronic configuration [Ar] $3d^3 4s^2$, couples with an arrangement of copper [Ar] $3d^{10} 4s^1$, silver [Kr] $4d^{10} 5s^1$, and gold [Xe] $5d^{10} 6s^1$ atoms, by specifically examining VCu_n^+, VAg_n^+, and VAu_n^+ clusters (n = 2-14). Precisely when and how this bonding occurs is determined by the electronic structure of the dopant and the host material respectively. As the cluster grows in size some of the dopant's electrons will form hybridized bonds, while others will continue to be localized. This leads to an eventual quenching of the magnetic spin moment as these valence electrons successfully couple to the nearly free electronic gas.

To understand exactly how the copper, silver, and gold atoms couple to the vanadium, we have identified the lowest-ground state structures and magnetic spin moments of VCu_n^+, VAg_n^+, and VAu_n^+ (n = 2-14). At small sizes, a 2D to 3D transition is observed, which affects the electronic structure and magnetic spin moment of the cluster. The enhanced *sd* hybridization experienced by the gold atoms allows the 1D delocalized shell to begin to fill at VAu_6^+, and provides a lowered alternating magnetic spin moment. Our calculations reveal that as the clusters grow in size, the $3d$ vanadium states start to participate in hybridized bonding with the surrounding atoms and the spin moment begins to systemically decease starting at VCu_8^+, VAg_{12}^+, and VAu_{11}^+ respectively. By using molecular orbital analysis, a detailed evaluation of the electronic profile of each cluster is offered. Enhanced electronic stability is found when there are 6, 8, and 18 delocalized electrons, which follows a simple shell-filling model. However, the manner in which the vanadium atom couples to the surrounding atoms, and the overall electronic structure of the cluster, determines stability of the system. By varying the energy levels of the

host material's *s* and *d* states, insight is provided that helps clarify the role of the host materials electronic structure in determining bonding characteristics and stability of localized magnetic spin moments in quantum confined systems.

5.1 Trends in copper, silver, and gold atoms

While copper, silver, and gold are all group 1B transition metals, they have different electronic structures, which will play a significant role in determining the overall properties of the clusters. The most obvious variances are found when comparing the energy levels of the *s* and *d* electrons of the copper, silver, and gold atoms. As shown in Figure 5.1-1, there is significant overlap between the 4*s* and 3*d* states of the copper, as they are both sitting around the same energy level, which allows the *s* and *d* states to hybridize relatively well. Comparatively, there is little difference in the 5*s* states of silver, however the 4*d* states are significantly lower in energy and there is a large energy difference between them. The relativistic quantum chemical effects of gold result in an even more varied electronic structure.[85–88] The 6*s* orbital experiences relativistic effects and contracts, driving the *s* electrons lower in energy. This contraction subsequently screens the nuclear attraction experienced by the 5*d* electrons, raising them in energy. These relativistic quantum effects play a significant role in determining the position of the *s* and *d* states in gold and leads to enhanced *sd* hybridization, which corresponds to changes in the overall bonding scheme of the cluster. These variations in the electronic structure of copper, silver, and gold have a profound effect on the manner in which the vanadium atom will interact with the nearly free electron gas of the respective clusters.

Atomic Energy Levels
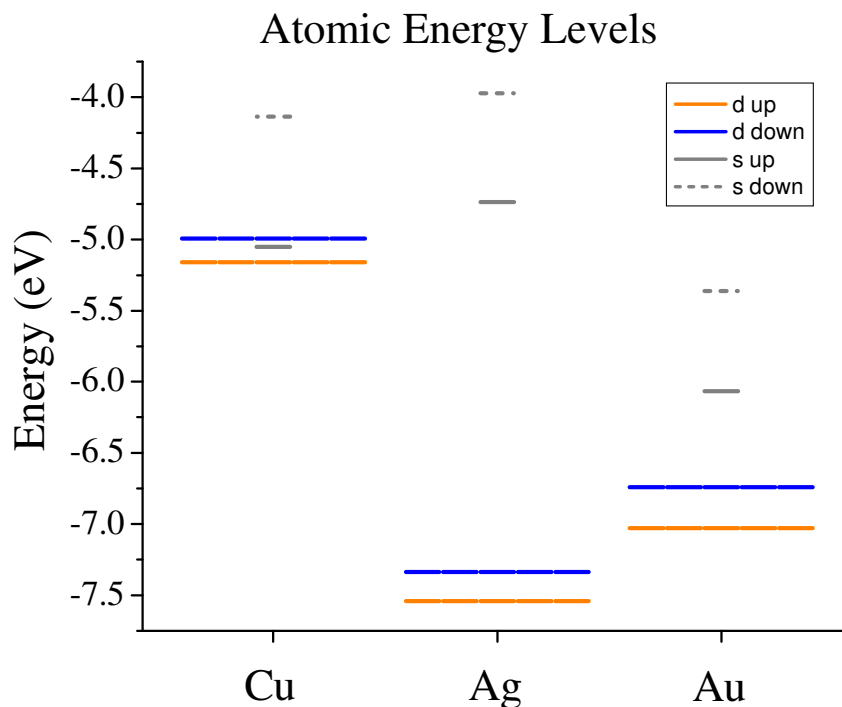
Figure 5.1-1. The energy levels of the *s* and *d* electrons in a single copper, silver, and atom are shown above. The relativistic quantum effects are responsible for the lowered energy level of the *s* electrons and raised *d* electrons in gold.

Precisely when and how this bonding occurs is determined by the electronic structure of the dopant and the host material respectively. Figure 5.1-2 shows the probability of the *s* and *d* electrons in copper, silver, and gold as a function of position. This radial distribution provides additional evidence of the differences between the electronic configuration of copper, silver, and gold, and we expect that these variances will have a profound effect on the bonding between the vanadium and the host metal. Our calculations show that the *s* and *d* states of the copper are more localized on the nucleus. Silver shows a larger radial distribution than copper, as the *s* and *d* states become less localized. The relativistic contraction of the gold 6*s* orbital and subsequent screening of the 5*d*, are exemplified by their respective peak positions.
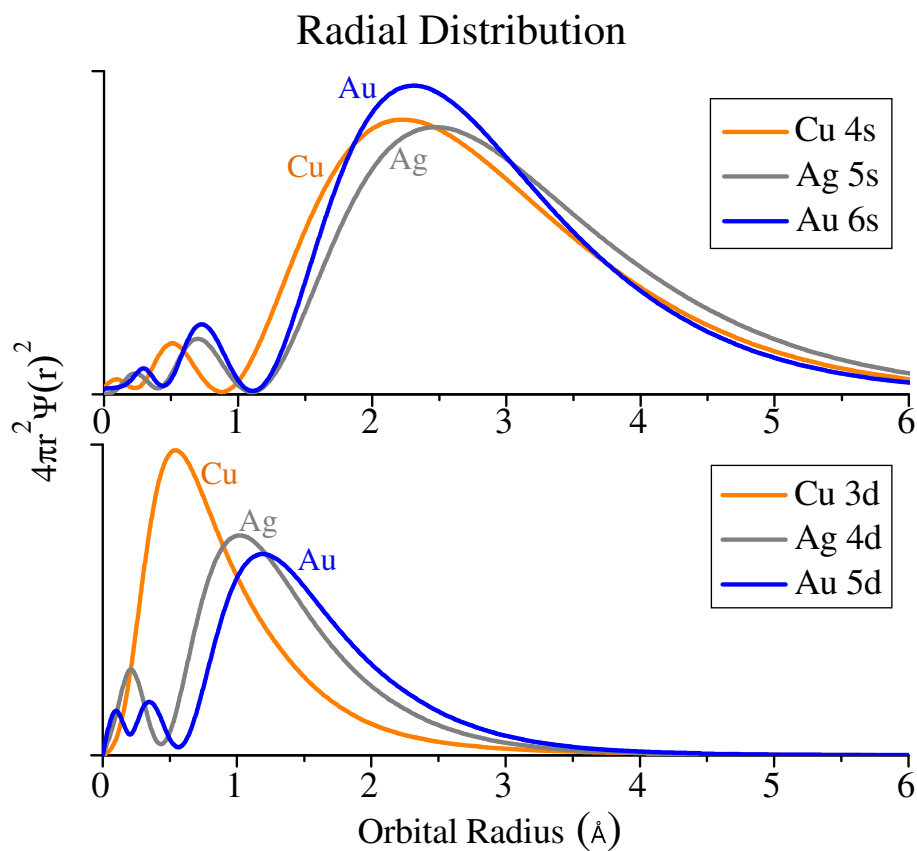
Figure 5.1-2. The probability of the *s* and *d* states of copper, silver, and gold are shown as a function of distance. The radial distribution provides information regarding the localization of the respective orbitals.

5.2 Structures and Energetic Properties of VCu_n^+, VAg_n^+, VAu_n^+ (n = 2-14)

The lowest ground state isomers for VCu_n^+, VAg_n^+, and VAu_n^+ (n = 2-14) are shown below. The geometries were optimized without constraint and were given full vibrational freedom. The HOMO-LUMO gaps and ionization potentials are also provided, along with the binding energies of copper, silver, gold, and vanadium.
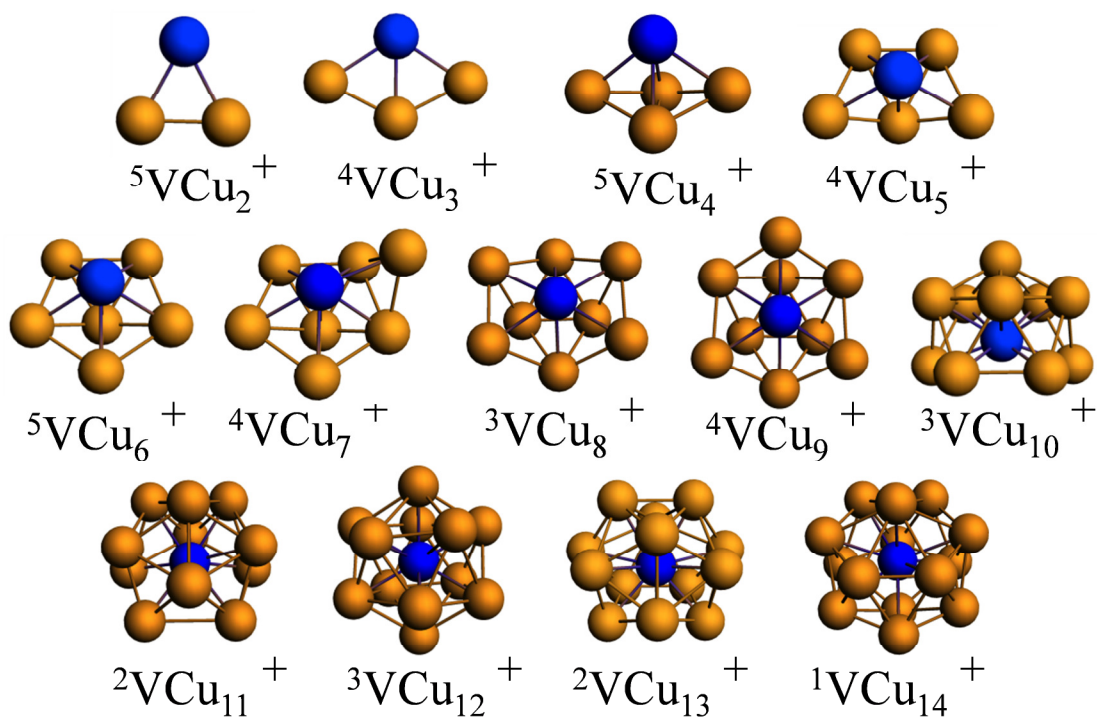
Figure 5.2-1. The optimized lowest-energy structures of VCu_{2-14}^{+}.
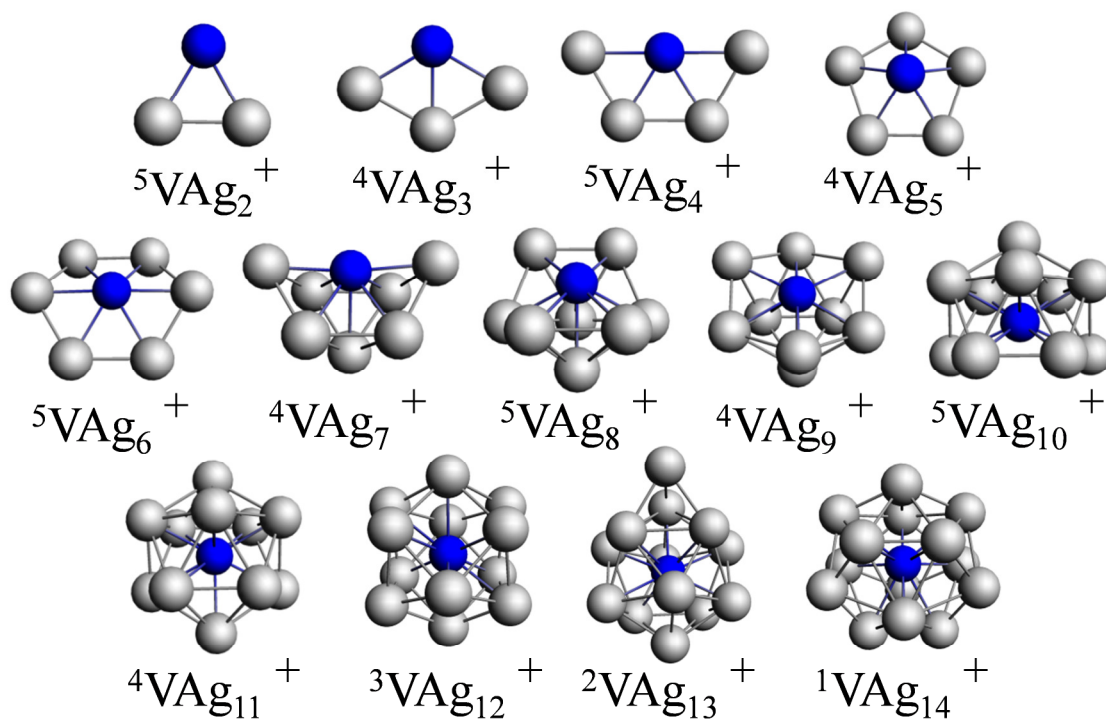
Figure 5.2-2. The optimized lowest-energy structures of VAg_{2-14}^{+}.
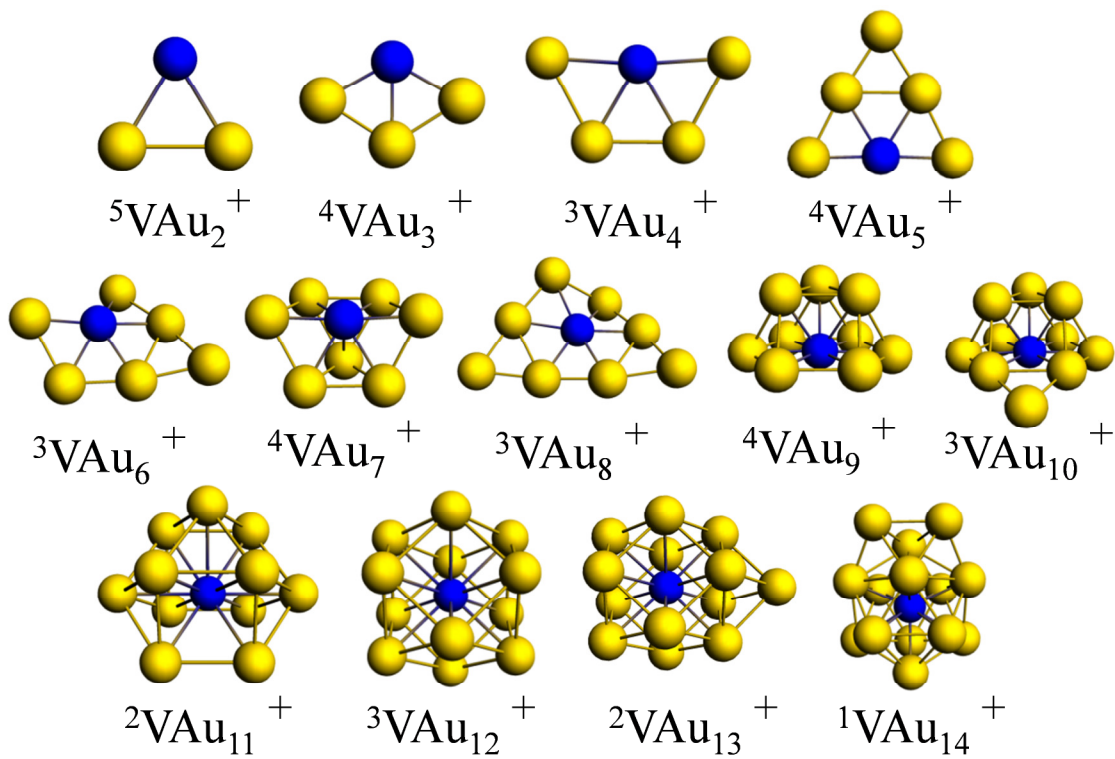
Figure 5.2-3. The optimized lowest-energy structures of VAu$_{2-14}^+$.
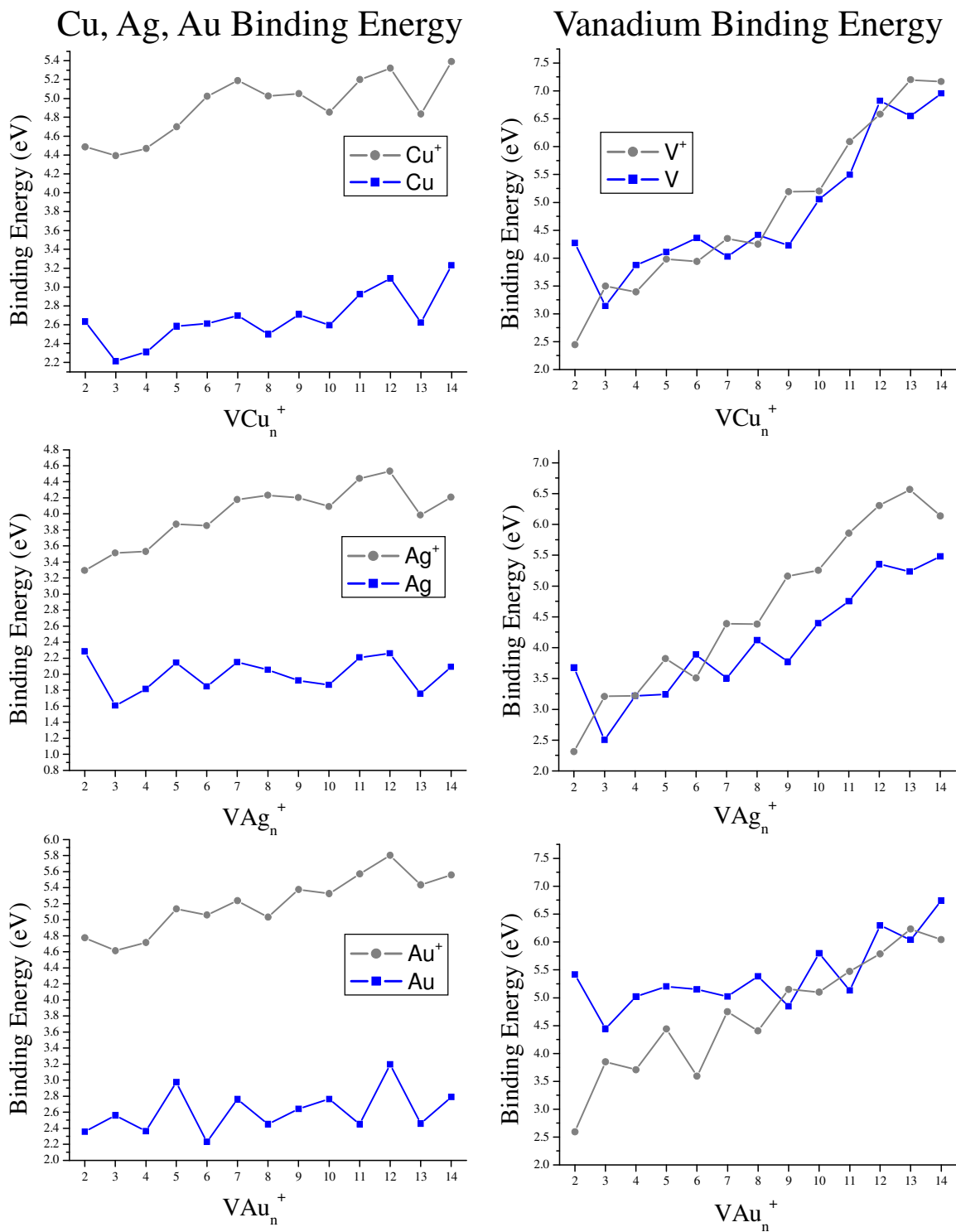
Figure 5.2-4. Copper, silver, gold, and vanadium binding energies of VCu_n^+, VAg_n^+, and VAu_n^+ (n = 2 – 14).

5.2.1 Electronic Stability
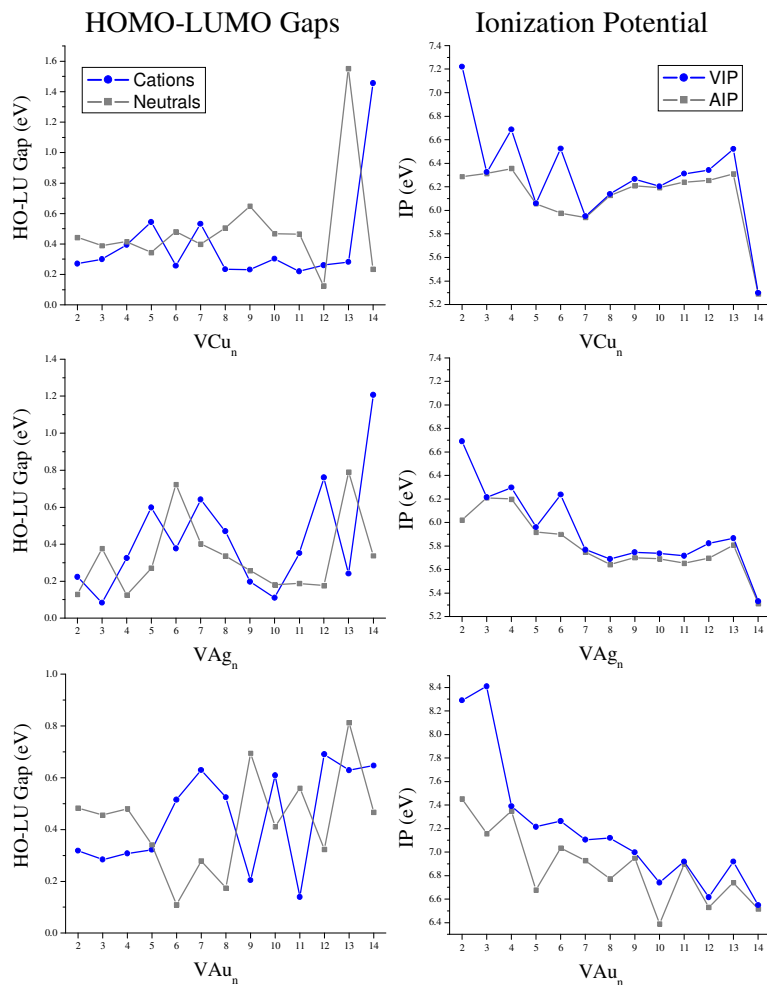
Figure 5.2.1-1. The HOMO-LUMO gaps and ionization potentials, vertical and adiabatic, of VCu_n^+, VAg_n^+, and VAu_n^+ (n = 2 – 14) are provided.

To understand how these geometric configurations affect the electronic stability of our system, the HOMO-LUMO gaps and ionization potentials are considered. We observe shell and subshell closures that correspond to relatively large gaps for the cations and lower ionization potentials for the corresponding neutral species. A subshell closure corresponding to a local maxima in HOMO-LUMO gaps of 0.54 eV and 0.60 eV is found for $^5VCu_5^+$ and $^5VAg_5^+$

respectively. Although both have 6 delocalized electrons providing a similar electronic structure of $1S^21P_x^21P_y^23d^3$, their respective geometries are distinctive. $^4VCu_5^+$ has a 3D geometric structure while $^4VAg_5^+$ favors a planar configuration. In both cases, the vanadium atom has two $4s$ electrons that are participating in hybridized bonding with the copper and silver atoms respectively and 3 localized $3d$ electrons. This subshell closure is also observed for $^4VAu_5^+$, which has a planer structure and its $1S^2$, $1P_x^2$, and $1P_y^2$ orbitals filled. However, our calculations reveal the HOMO is raised in energy, providing large exchange splitting and a lowered gap of only 0.32 eV. As discussed in the previous section, there is a 2D to 3D geometric transition undertaken by the silver and gold vanadium clusters at n = 7. At this size the vanadium atom in $^4VCu_7^+$, $^4VAg_7^+$, and $^4VAu_7^+$ is contributing 3 localized $3d$ electrons to the majority spin channel, and the $1S^2$, $1P_x^2$, $1P_y^2$, and $1P_z^2$ orbitals are filled resulting in an electronic structure of $1S^21P^63d^3$. The filling of the $1S^2$ and $1P^6$ orbitals corresponds to 8 delocalized electrons, allowing for a full shell closure and relatively high HOMO-LUMO gaps of 0.53 eV, 0.64 eV, and 0.63 eV for the copper, silver, and gold systems respectively.
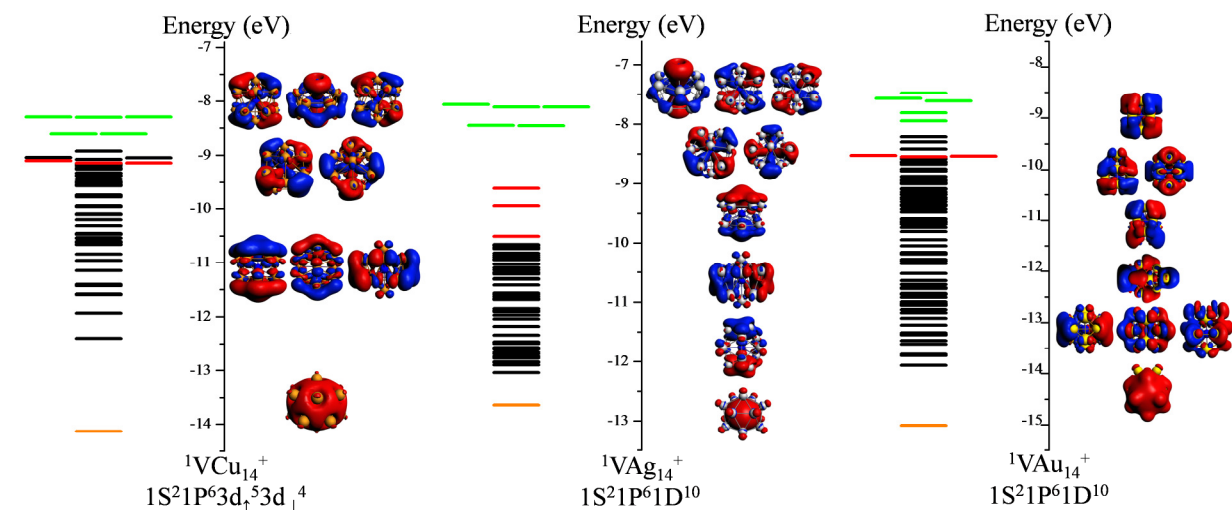
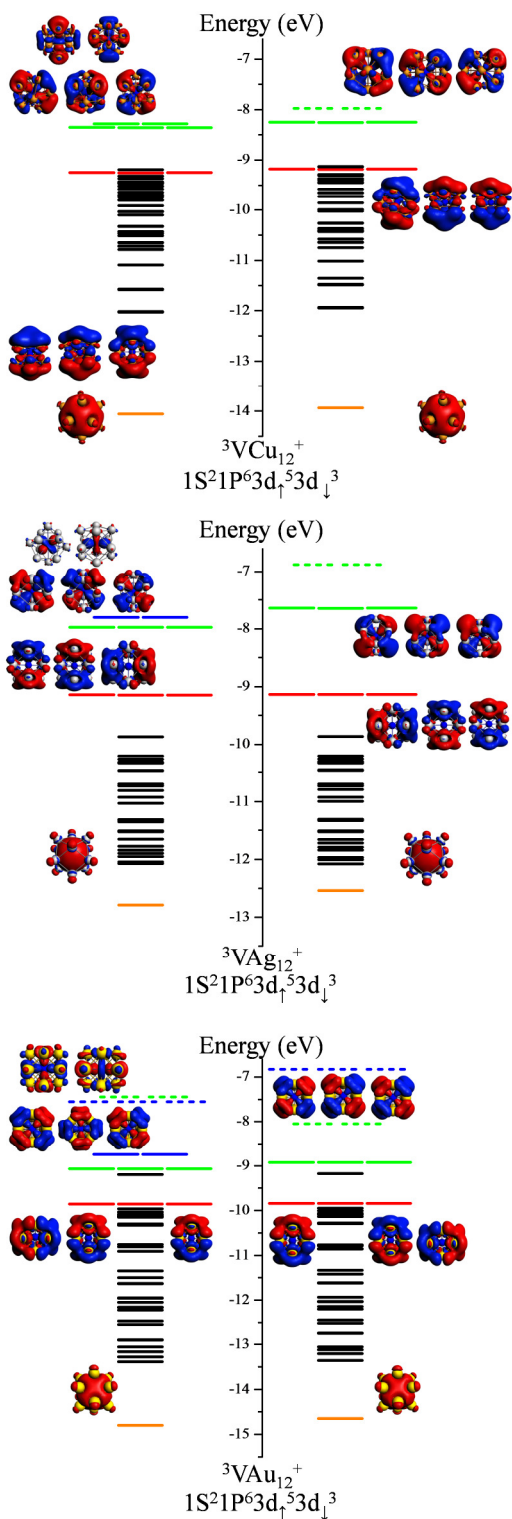**Figure 5.2.1-2**. Molecular orbital diagram of $^1VCu_{14}^+$, $^1VAg_{14}^+$, and $^1VAu_{14}^+$. Solid lines represent occupied orbitals, while the dashed lines represent empty orbitals. The orange, red, and green lines correspond to the delocalized orbitals, 1S, 1P, and 1D. A picture of each delocalized orbital is provided in the order in which it occurs.

While the majority of the local maxima observed in the HOMO-LUMO gaps correspond to these subshell and shell fillings, there is a peak at $^3VAu_{10}^+$ which as 14 valence electrons. The highest occupied molecular orbital is a 1D orbital in the minority spin channel. The prolate geometry of $^3VAu_{10}^+$ results in a crystal-field-like splitting effect, where the orbitals in the xy-plane drop in energy and the d_z^2 orbital increase in energy. This allows for the formation of the delocalized 1D orbitals to form along the xy-plane. The result of this significant orbital splitting yields a respectable HOMO-LUMO gap of 0.61 eV. There are also peaks at $^3VAg_{12}^+$ and $^3VAu_{12}^+$. Both have highly symmetrical octahedral geometric structures and HOMOs that consist of a partially filled e_g shell. The electronic structure of this symmetric structure is $1S^2 1P^6 3d_\uparrow^5 3d_\downarrow^3$, which results in a magnetic spin moment of 2. The localized magnetic spin moment is finally quenched at $^1VCu_{14}^+$, $^1VAg_{14}^+$, and $^1VAu_{14}^+$ as each cluster gains a closed electronic shell of $1S^2 1P^6 1D^{10}$, corresponding to 18 electrons. This electronic structure is providing enhanced stability for $^1VCu_{14}^+$ and $^1VAg_{14}^+$ with HOMO-LUMO gaps of 1.46 eV and 1.21 eV respectively. While $^1VAu_{14}^+$ also has 18 valence electrons and an electronic structure of $1S^2 1P^6 1D^{10}$, this closed electronic shell is responsible for a relatively small HOMO-LUMO gap of only 0.65 eV. This lowered HOMO-LUMO gap is most likely cause by the relatively unsymmetrical geometric configuration, which lowers the unoccupied d_z^2 orbital. The ionization potentials exhibit trends that correspond the subshell and shell closures for VCu_n^+ and VAg_n^+ at n = 5, 7, and 14. VAu_n^+ has much less pronounced minimums, which can be attributed to the planer structures the neutral gold vanadium clusters posses at small sizes.

Energy (eV)

^{3}VCu$_{12}^+$
1S^{2}1P^{6}3d$_\uparrow^5$3d$_\downarrow^3$

Energy (eV)

^{3}VAg$_{12}^+$
1S^{2}1P^{6}3d$_\uparrow^5$3d$_\downarrow^3$

Energy (eV)

^{3}VAu$_{12}^+$
1S^{2}1P^{6}3d$_\uparrow^5$3d$_\downarrow^3$

Figure 5.2.1-3. Molecular orbital diagram of ^{1}VCu$_{12}^+$, ^{1}VAg$_{12}^+$, and ^{1}VAu$_{12}^+$. Solid lines represent occupied orbitals, while the dashed lines represent empty orbitals. The orange, red, and green lines correspond to the delocalized orbitals, 1S, 1P, and 1D. A picture of each delocalized orbital is provided in the order in which it occurs.

65

5.3 Changes in Multiplicity
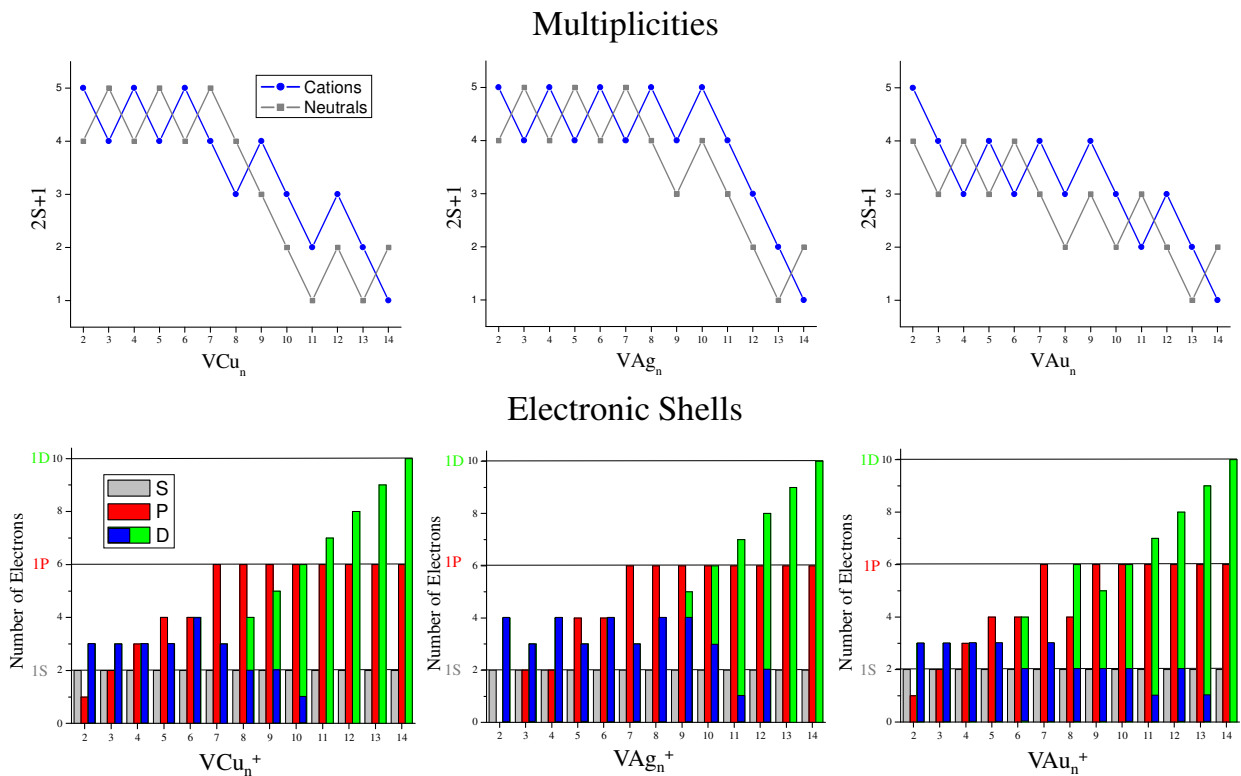
Figure 5.3. The spin multiplicities and corresponding electronic shells of VCu_n^+, VAg_n^+, and VAu_n^+ (n = 2 – 14) are shown above. The silver, red, and green columns represent orbitals corresponding to the $1S^2$, $1P^6$, and $1D^{10}$ shells, respectively. The localized $3d$ vanadium states are represented by the blue columns, which are superimposed over the $1D^{10}$ columns.

The manner in the vanadium atom bonds to the surrounding copper, silver, and gold atoms is most pronounced when the localized magnetic moment on the vanadium atom is considered. Figure 5.3 displays the multiplicities and electronic shells of each cluster. Earlier studies have revealed that the *s* electrons of the host material and the dopant will initially hybridize and fill the $1S^2$ and $1P^6$ shells,[8,9,80] The $3d$ vanadium states (blue) are shown to gradually decrease as they participate in hybridized bonding and subsequently fill the 1D delocalized shell (green). Our calculations reveal both VCu_n^+ and VAg_n^+ have an alternating

multiplicity of 4 and 5. While the VAg_n^+ clusters have the same alternating magnetic moment as VCu_n^+, the molecular orbital analysis shows the $5s$ and $4d$ states of the silver are not hybridizing with the vanadium as well. Consequently, the localized 3d states on the vanadium atom do not start to participate in hybridized bonding with the silver atoms as early, and the magnetic spin moment does not begin to get quenched as soon. VAu_n^+ experiences a lowered alternation of 3 and 4, the exception being VAu_2^+. Upon closer examination of the molecular orbital diagrams, the localized $3d$ states on the vanadium atom are found to be coupling more successfully to the gold atoms at small sizes. This is confirmed by lower alternating multiplicity and the formation of the delocalized 1D orbital at VAu_6^+.

At larger sizes, the magnetic spin moment associated with these localized $3d$ states start to decrease. The $3d$ vanadium electrons begin to participate in hybridized bonding with the copper at VCu_8^+ and are completely hybridizing with the shallow copper s and d states at VCu_{11}^+. Our calculations reveal that as the minority spin channel begins to fill the $3d$ vanadium states begin to form delocalized bonds at VCu_8^+, and the magnetic spin moment begins to decrease. At VCu_{11}^+, all of the $3d$ vanadium states are fully coupled to the copper atoms, providing an electronic structure of $1S^2 1P^6 1D_\uparrow^4 1D_\downarrow^3$. This full hybridization occurs earlier for copper than both the silver and gold vanadium cases. For VAg_n^+ our molecular orbital analysis shows that at $^4VAg_9^+$ the localized 3d states begin to hybridize and contribute to the delocalized 1D orbital and the 3d/1D minority spin channel begins to fill. Although there is slight participation from the vanadium's $3d$ electrons, 4 localized states remain on the vanadium and our analysis shows they are located in the majority spin channel. There are now a total of 5 electrons in the 3d/1D orbital, which provides a magnetic spin moment of $3\mu_B$. As the cluster continues to grow there is greater $3d$ contribution and the moment begins to be quenched at

$^3VAg_{12}^+$. Our calculations indicate that the octahedral structure of $^3VAg_{12}^+$ has 16 valence electrons, 14 of which are contributing to the delocalized orbitals, while the last 2 are localized on the vanadium. This provides an electronic structure of $1S^21P^63d_\uparrow^53d_\downarrow^3$, and a magnetic spin moment of 2. However, unlike copper, not all of the 3d vanadium states are fully hybridized to the silver atoms. Full participation does not occur until $^3VAg_{13}^+$, when the 3d/1D majority spin channel is completely filled. The difference between the copper and silver vanadium systems can be attributed to the relative position of the *d* states and the subsequent bond distances they provide. The 3*d* states of the copper sit higher in energy, creating a more localize orbital, a shorter bond distance, and greater mixing between the *s* and *d* states. This allows the 3*d* and 4*s* states of the vanadium to couple more easily to the copper than the silver at larger sizes. The increased contribution from the copper *d* states and the decrease in multiplicity at VCu_8^+ confirms this.

5.3.1 Enhanced *sd* hybridization

While our comparison shows a superior gold-vanadium interaction at smaller sizes, the alternating magnetic moment does not begin to decrease until VAu_{11}^+ and the 3d states do not fully participate in hybridized bonding until the magnetic spin moment is quenched at VAu_{14}^+. We expect this is due to the geometric configuration of the large VAu_n^+ clusters and the greater bond distances attributed to such arrangements. To understand this variation in electronic and geometric structure, the average bond length between the vanadium and the gold atoms are examined. Although our calculations reveal that the average V-Cu bond distances are shortest, the localized 3*d* states of the vanadium atom are coupling more effectively to the 5*d* and 6*s* states

Average Vanadium Bond Distance
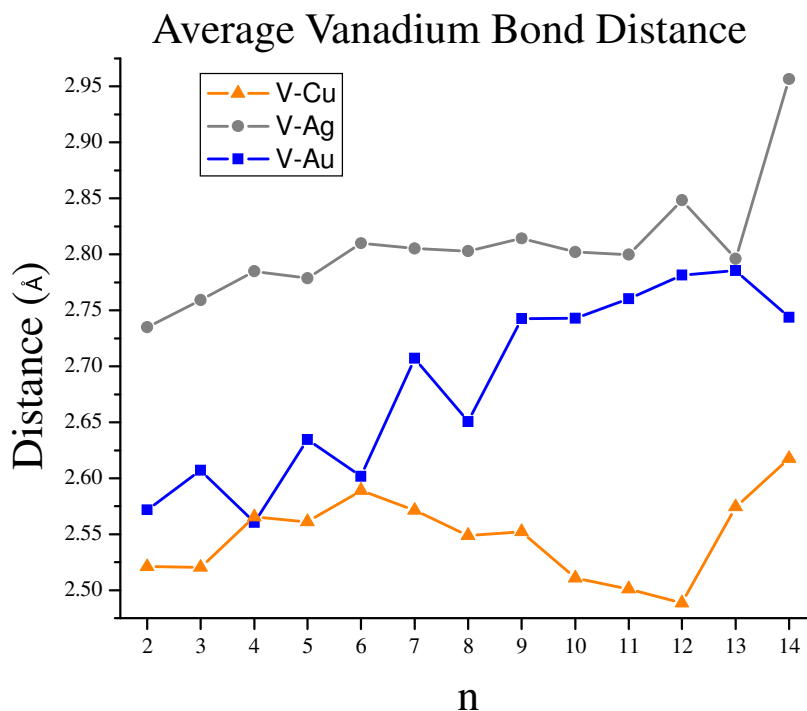
Figure 5.3.1. The average bond distance between the vanadium atom and the surrounding copper, silver, and gold atoms are plotted. While VCu_n^+ and VAg_n^+ have relatively steady trends, there is an even-odd effect in gold between n = 2 – 8.

of the gold atoms at small sizes. Figure 5.3.1 shows that there are local minimums at $^3VAu_4^+$, $^3VAu_6^+$, and $^3VAu_8^+$, which have average V-Au bond distances of 2.56, 2.60, and 2.65 angstroms respectively. This even-odd alternation is not seen in the V-Cu and V-Ag average bond distances. These shortened V-Au bond distances allow the localized 3*d* electrons on the vanadium to successfully couple to the 5*d* and 6*s* states of the gold atoms, providing significantly more contribution to the delocalized orbitals. This is confirmed by our molecular orbital plots and the lower alternating magnetic spin moment. The origin of this result can be attributed to the relativistic quantum effects experienced by the gold atoms and the subsequent enhanced *sd* hybridization it provides.[87]

This pronounced *sd* hybridization is most clear when considering $^3VAu_6^+$, which has 10 valence electrons and an electronic configuration of $1S^2 1P_x^2 1P_y^2 3d_\uparrow^3 3d_\downarrow^1$. Of these valence

electrons, 8 are contributing to the delocalized orbitals and 2 are localized on the vanadium atom. What is interesting about this cluster is instead of filling the delocalized $1P^6$ shell, the planar geometry is forcing the $1P_z^2$ delocalized orbital to be high in energy, and the increased *sd* hybridization provided by the relativistic quantum effects allows the 1D orbital to partially fill. This partial filling occurs at a much smaller size than the copper and silver vanadium systems, which begin to fill their 1D delocalized orbital at $^3VCu_8^+$ and $^4VAg_9^+$ respectively. We attribute the partial filling of the 1D delocalized orbital at such a small size to the enhanced *sd* hybridization provided by the relativistic quantum effects.

We expected that this increase in *sd* hybridization will allow the 3*d* states of the vanadium to completely couple to the gold atoms and contribute to form delocalized orbitals more quickly than copper or silver. However, the molecular orbital analyses and their respective atomic contributions reveal there is a 3*d* state still localized on the vanadium atom at $^2VAu_{13}^+$. As the cluster grows in size and the 2D structures transition to 3D, we see a steady increase in the average V-Au bond distance and a maximum at $^2VAu_{13}^+$. This cluster has an octahedral structured geometry with an adatom site, which provides significant separation between the gold and the vanadium atoms. The increase in bond distance makes it energetically unfavorable for all of the 3*d* states to completely participate in hybridized bonding. It is interesting to note that $^3VAg_{12}^+$ also has the same octahedral structure, however the cluster deforms as the thirteenth silver atom is added. This yields a local minimum in V-Ag bond distance, allowing the 3*d* electrons on the vanadium cluster to fully participate in hybridized bonding. This same deformation is not observed with $^2VAu_{13}^+$ and we conclude that the lack of deformation and the local maximum in the V-Au bond distance is responsible for the lack of hybridization.

5.4 Consequences of Geometric Variations

One of the more interesting features of these bimetallic transition metal clusters is the difference in geometric configuration. While small VCu_n^+ clusters prefer 3D geometries, our calculations show that VAg_n^+ and VAu_n^+ favor planer structures. We expect this 2D to 3D transition corresponds to a split shell model, where at VX_7^+ (X = Cu, Ag, and Au) there are 8 delocalized electrons, and 3 localized electrons. This makes the filling of the $1P^6$ shell energetically favorable, and implies that VX_7^+ should be approximately spherical, allowing the $1P_z$ orbital to drop in energy. This would imply that VX_6^+ should have a planar geometry until the constituent atoms provide enough electrons to fill the $1P^6$ shell. At this size there should be 6 delocalized electrons, and 4 localized. While our calculations show that VAg_6^+ follows this pattern, the enhanced *sd* hybridization in gold results in the formation of a 1D delocalized orbital at VAu_6^+ and the electronic configuration of the 4s and 3d states in copper do not permit a 2D geometric trend to occur after VAu_3^+.

To understand how this geometry affects the electronic profiles of the clusters, the molecular orbital diagrams of n = 6–9 are shown in Figures 5.4-1 and 5.4-2. The electronic structure of $^5VCu_6^+$ has the $1S^2$, $1P_x^2$, and $1P_y^2$ delocalized orbitals filled, however instead of filling the $1P_z^2$ orbital the vanadium atom is providing 4 localized 3*d* electrons in the spin majority channel. These 4 localized electrons are responsible for the large exchange splitting observed in the electronic profile and a lowered HOMO-LUMO gap. $^4VCu_7^+$ has a rather prolate 3D geometry, which accounts for the relatively large $1P^6$ orbital width. The vanadium atom is contributing 3 localized 3*d* electrons to the majority spin channel, and the $1S^2$, $1P_x^2$, $1P_y^2$, and $1P_z^2$ orbitals are filled resulting in an electronic structure of $1S^2 1P^6 3d^3$. The filling of the $1S^2$
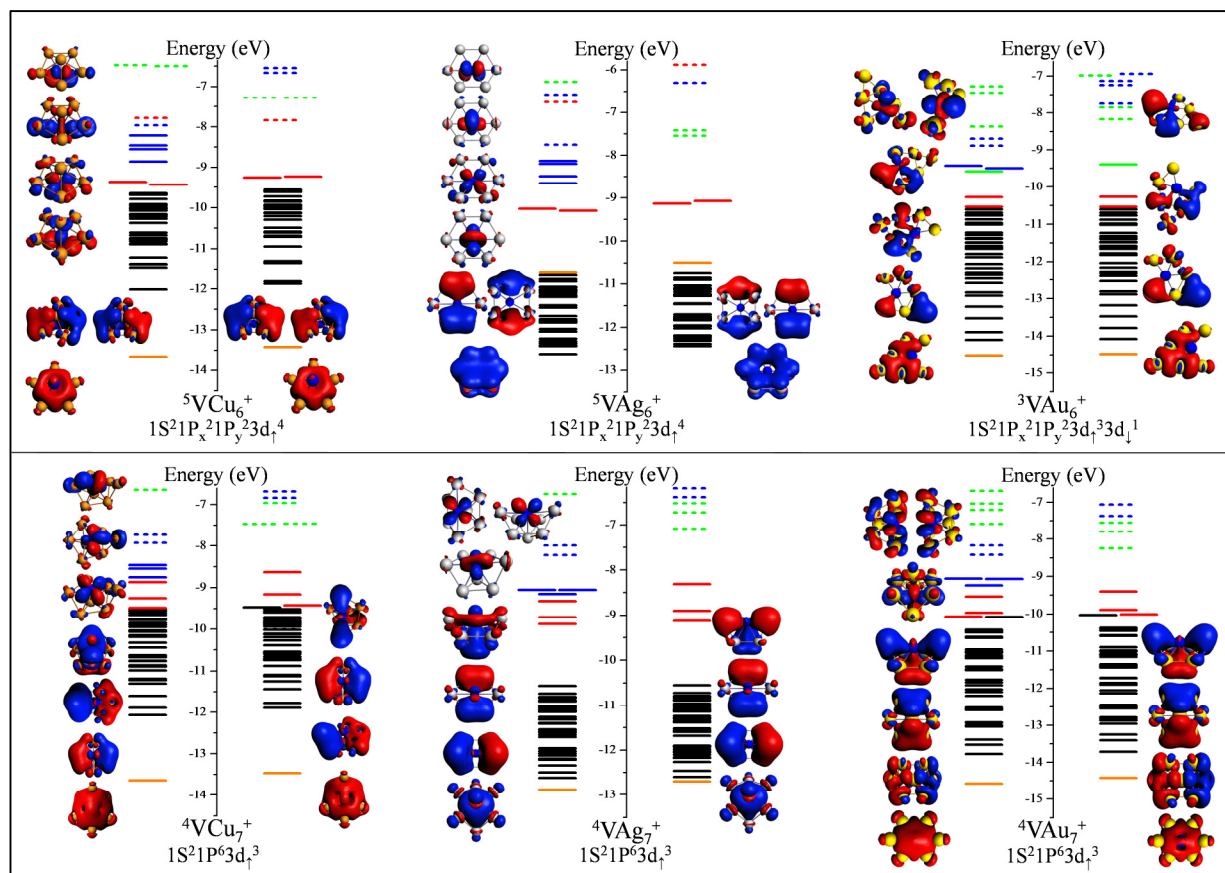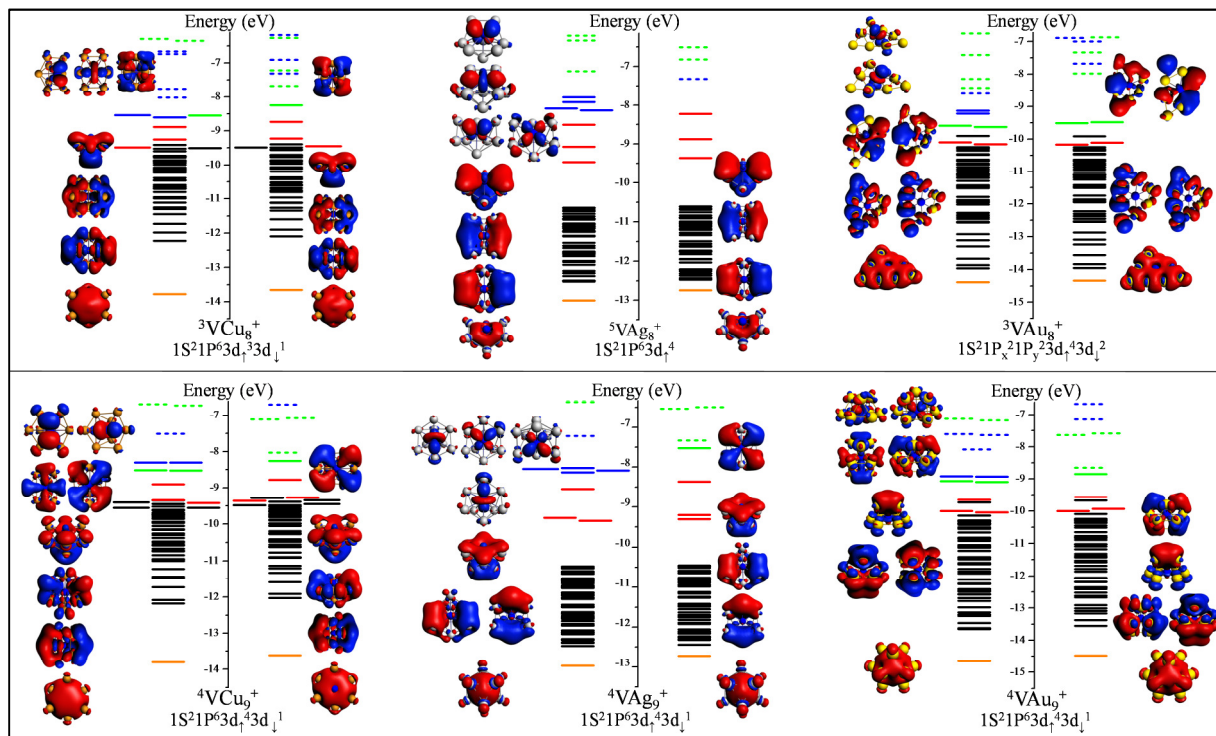
Figure 5.4-1. The molecular orbital diagrams for VCu_n^+, VAg_n^+, and VAu_n^+ (n = 6 – 7). The filled orange, red, and green lines represent orbitals corresponding to the $1S^2$, $1P^6$, and $1D^{10}$ shells, respectively, and the blue lines represent the localized 3d vanadium states. The dashed lines, the color of which represents by the same orbitals as the filled lines, denote the unoccupied orbitals. Pictures of the delocalized orbitals and the localized $3d$ vanadium orbitals are stacked as they appear in the molecular orbital analysis.

and $1P^6$ orbitals corresponds to 8 delocalized electrons, allowing for a full shell closure, and enhanced stability and drives the structure towards a spherical geometry. At $^3VCu_8^+$ both the $1S^2$ and $1P^6$ shells are filled. As the molecular orbital diagrams reveal in Figure 5.4-2, an additional electron is found in the 3d/1D minority spin channel. This lowers the magnetic moment down to 2, and yields an electronic structure of $1S^21P^63d_\uparrow^33d_\downarrow^1$. $^5VAg_6^+$ has a distorted planar geometry and an electronic structure of $1S^21P_x^21P_y^23d^3$. The vanadium atom is providing 4 localized 3d

Figure 5.4-2. The molecular orbital diagrams for VCu_n^+, VAg_n^+, and VAu_n^+ (n = 8 − 9). The filled orange, red, and green lines represent orbitals corresponding to the $1S^2$, $1P^6$, and $1D^{10}$ shells, respectively, and the blue lines represent the localized 3d vanadium states. The dashed lines, the color of which represents by the same orbitals as the filled lines, denote the unoccupied orbitals. Pictures of the delocalized orbitals and the localized 3d vanadium orbitals are stacked as they appear in the molecular orbital analysis.

electrons in the spin majority channel, as the $1P_z^2$ delocalized orbital is still too high in energy to be filled. This is responsible for a magnetic spin moment of 4 and substantial exchange splitting. The distorted planer geometry of $^3VAu_6^+$ has the $1S^2$, $1P_x^2$, and $1P_y^2$ orbitals filled as well, however the vanadium atom is only providing 2 localized 3d electrons to the majority spin channel. The other 3d electron is participating in hybridized bonding with the gold atoms, and contributing to the delocalized 1D orbital in the spin majority and minority channel. The 2D to 3D geometric transition undertaken by the silver and gold vanadium clusters occurs at VAg_7^+ and VAu_7^+ when there are 8 delocalized electrons. This geometric transition allows the $1P_z^2$ orbital to drop in energy and become filled, resulting in a closed electronic shell. After this

transition, VAg_n^+ continues to prefer 3D structures and the 3d/1D orbital eventually begins to fill. However, the gold vanadium system experiences a transition back to a 2D structure at $^3VAu_8^+$. This cluster has 9 delocalized electrons, however only the $1S^2$, $1P_x^2$, and $1P_y^2$ orbitals are filled. Due to its planar-like geometry, the $1P_z^2$ orbital is not filled. The enhanced *sd* hybridization allows the 3d vanadium electrons to undergo hybridized bonding with the electrons of the gold, which forms 2 sets of degenerate 1D delocalized orbitals in the spin majority and spin minority channels respectively. This leaves only 2 localized 3d electrons in the spin majority channel, which are responsible for a magnetic spin moment of 2. There is a final 2D to 3D transition at $^4VAu_9^+$, allowing the $1P_z^2$ orbital to be filled. Our calculations reveal there is also partial hybridization between the vanadium 3d electrons and the electrons in the gold, providing 5 electrons in the 3d/1D orbital. This yields an electronic structure of $1S^2 1P^6 3d_\uparrow^4 1d_\downarrow^1$, with 3 delocalized 1D orbitals, 2 in the majority spin channel and 1 in the minority spin channel.

5.5 Conclusions

The electronic and geometric properties of VCu_n^+, VAg_n^+, and VAu_n^+ clusters have been extensively considered. Our calculations have shown that the electronic structure of the host cluster plays a significant role in determining the bonding characteristics of a dopant with a localized magnetic spin moment. A size-dependent trend is found to exist that determines when the electrons of the vanadium atom will participate in hybridized bonding. The stability of the clusters change as the delocalized shells fill, and an increase in electronic stability is observed. We observe other local maxima in the HOMO-LUMO gap for $^3VAu_{10}^+$, $^3VAg_{12}^+$ and $^3VAu_{12}^+$, which can be attributed to their respective geometric configurations. Which shell is filled

depends whether the geometry of the cluster is 2D or 3D. To understand this bonding scheme the molecular orbital diagrams of each cluster are considered. The first subshell closure occurs at n = 5 where the $1S^2$, $1P_x^2$, and $1P_y^2$ orbitals are filled and there are 3 localized $3d$ electrons remaining on the vanadium atom. At $^4VCu_7^+$, $^4VAg_7^+$, and $^4VAu_7^+$ each cluster has 8 delocalized electrons, which correspond to a closed electronic shell, enhanced electronic stability, and 3D geometric configuration. As the clusters grow in size the $3d$ states of the vanadium will start to participate in hybridized bonding, eventually fully coupling to the host metal atoms at $^1VCu_{14}^+$, $^1VAg_{14}^+$, and $^1VAu_{14}^+$. A detailed analysis of the 2D to 3D geometric transition of both the gold and silver clusters is provided, and the consequences of this transition are expounded upon by examining the average bond distances of each cluster. As a result we find a varied alternation in multiplicity at small sizes between VCu_n^+ and VAg_n^+, which have an alternating multiplicity of 4 and 5, and VAu_n^+, whose multiplicity alternates between 3 and 4. Our calculations reveal this variation is caused by local minima in the average bond distance of the V-Au atoms. As the cluster grows in size the localized magnetic moment begins to be quenched, providing a lowered alternating multiplicity.

Chapter 6

Conclusions

6.1 Summary and Future Projects

The main objective of this work centered on understanding the stability of ligated superatoms and bimetallic transition metal clusters. By identifying energetically stable clusters, novel materials can be synthesized that use these stable clusters as building blocks and take advantage of their highly tunable properties. However, because the electronic and geometric structure of a cluster can change drastically with the addition or removal of a single atom or electron, understanding how a cluster is perturbed when a ligand or dopant is introduced is advantageous. To this end aluminum iodine superatoms and vanadium-doped copper, silver, and gold clusters are examined. The addition of iodine ligands to aluminum superatoms may activate or passivate a cluster depending on the metal core of the cluster and the position of the ligand. To minimize the reactivity of a ligand-protected cluster, the metallic core should have a closed geometric shell and an even distribution of charge on the surface. Furthermore, ligands are found to be passivating when they are located in a balanced position on opposite sides of the metallic core. For example, $Al_{13}I_2^-$ has an icosahedral core with no adatom and balanced ligands, and is passivated with respect to methanol. The importance of balanced ligands, a

symmetric geometry, and an even charge distribution is most notable when $Al_{14}I_3^-$ is considered. $Al_{14}I_3^-$ has a metallic core with an activated adatom site with an iodine atom. The position of the ligand exacerbates the already uneven charge disruption of the cluster and is therefore reactive when exposed to methanol. The position of the iodine may induce an active site on the opposite side of the cluster. $Al_9I_3^-$ is reactive when the iodine atoms are unbalanced; however when the three iodine atoms are balanced on opposite sides of the cluster, the cluster is passivated. This work demonstrates that even if a cluster is protected by ligands, the cluster could be reactive when the geometric considerations are not met, revealing the dual roles of electronic and geometric structure on the stability of bare and ligand-protected nanoparticles. Future studies could be conducted to understand how the polarity of the solvent changes the reaction pattern of the cluster. Also, by considering the manner in which the reactant changes the electronic profile a cluster with a closed electronic shell, more insight could be provided into the reaction dynamics of the superatom clusters with polar solvents.

When a magnetic dopant is introduced into a cluster, the electronic structure of the surrounding atoms play a major role in determining the bonding scheme between the impurity and host material. Therefore, understanding the interplay between the impurity and host material's electronic structures and their ability to couple to one another is imperative. To understand this interaction, the electronic and geometric properties of VCu_n^+, VAg_n^+, and VAu_n^+ clusters have been extensively considered. A size dependent trend is found to exist that determines when the electrons of the vanadium atom will participate in hybridized bonding. As the clusters grow in size, the $3d$ states of the vanadium will start to participate in hybridized bonding, eventually fully coupling to the host metal atoms at $^2VCu_{11}^+$, $^2VAg_{13}^+$, and $^1VAu_{14}^+$. Which orbitals participate in hybridization depends on the geometry of the cluster and the

symmetry of the delocalized electronic orbitals. To highlight how gaining a closed electronic shell changes the geometry of the cluster, VX_7^+ is considered. As the clusters gain 11 valence electrons, our calculations show that 8 of those electrons will contribute to the delocalized $1S^2$ and $1P^6$ shells and 3 electrons will be localized on the vanadium. This split-shell electronic configuration provides a closed electronic shell, enhanced electronic stability, and a 3D geometric configuration. The bond distance between the vanadium and the host material is found to play a significant role in determining the magnitude of the magnetic spin moment. Our results show the enhanced *sd* hybridization of gold leads to local minima in Au-V bond distances, which is responsible for the lowered alternation in multiplicity. Our work demonstrates that the electronic structure and coordination of the host material plays a substantial part in determining how a magnetic impurity will couple to the surrounding atoms. Future studies could be undertaken to see how the geometric structure of the constituent atoms in the cluster determines how the impurity couples to the surrounding atoms. Simply by changing the geometric configuration of the system, the magnitude of the magnetic moment could be varied dramatically and tuned to meet specific requirements.

References

[1] A.W. Castleman and S.N. Khanna, J Phys Chem C **113**, 2664 (2009).

[2] A.W. Castleman, S.N. Khanna, A. Sen, A.C. Reber, M. Qian, K.M. Davis, S.J. Peppernick, A. Ugrinov, and M.D. Merritt, Nano Lett **7**, 2734 (2007).

[3] M. Walter, J. Akola, O. Lopez-Acevedo, P.D. Jadzinsky, G. Calero, C.J. Ackerson, R.L. Whetten, H. Grönbeck, and H. Häkkinen, Proc. Natl. Acad. Sci. **105**, 9157 (2008).

[4] S. Malola and H. Häkkinen, J. Phys. Chem. Lett. **2**, 2316 (2011).

[5] A. Dass, J. Am. Chem. Soc. **131**, 11666 (2009).

[6] M.F. Bertino, Z.-M. Sun, R. Zhang, and L.-S. Wang, J. Phys. Chem. B **110**, 21416 (2006).

[7] Y. Negishi, K. Nobusada, and T. Tsukuda, J. Am. Chem. Soc. **127**, 5261 (2005).

[8] V.M. Medel, A.C. Reber, V. Chauhan, P. Sen, A.M. Köster, P. Calaminici, and S.N. Khanna, J. Am. Chem. Soc. **136**, 8229 (2014).

[9] E. Janssens, S. Neukermans, H.M.T. Nguyen, M.T. Nguyen, and P. Lievens, Phys. Rev. Lett. **94**, 113401 (2005).

[10] E. Janssens, S. Neukermans, X. Wang, N. Veldeman, R.E. Silverans, and P. Lievens, Eur. Phys. J. - At. Mol. Opt. Plasma Phys. **34**, 23 (2005).

[11] J.U. Reveles, P.A. Clayborne, A.C. Reber, S.N. Khanna, K. Pradhan, P. Sen, and M.R. Pederson, Nat Chem **1**, 310 (2009).

[12] X. Jin, G. Espinoza-Quintero, B. Below, V. Arcisauskaite, J.M. Goicoechea, and J.E. McGrady, J. Organomet. Chem. (n.d.).

[13] M.B. Abreu, A.C. Reber, and S.N. Khanna, J. Phys. Chem. Lett. **5**, 3492 (2014).

[14] W.D. Knight, K. Clemenger, W.A. de Heer, W.A. Saunders, M.Y. Chou, and M.L. Cohen, Phys. Rev. Lett. **52**, 2141 (1984).

[15] W.A. de Heer, W.D. Knight, M.Y. Chou, and M.L. Cohen, in *Solid State Phys.*, edited by H.E. and D. Turnbull (Academic Press, 1987), pp. 93–181.

[16] W. Ekardt, *Metal Clusters* (Wiley, New York, 1999).

[17] R.I.G. Hughes, (2006).

[18] R.E. Leuchtner, A.C. Harms, and A.W. Castleman, J. Chem. Phys. **91**, 2753 (1989).

[19] R.E. Leuchtner, A.C. Harms, and A.W. Castleman, J. Chem. Phys. **94**, 1093 (1991).

[20] S.N. Khanna and P. Jena, Phys. Rev. Lett. **69**, 1664 (1992).

[21] S.N. Khanna and P. Jena, Phys. Rev. B **51**, 13705 (1995).

[22] C. Ashman, S.N. Khanna, F. Liu, P. Jena, T. Kaplan, and M. Mostoller, Phys. Rev. B **55**, 15868 (1997).

[23] P. Jena, S. n. Khanna, and B. k. Rao, Surf. Rev. Lett. **3**, 993 (1996).

[24] H. Göhlich, T. Lange, T. Bergmann, and T.P. Martin, Phys. Rev. Lett. **65**, 748 (1990).

[25] X. Li, H. Wu, X.-B. Wang, and L.-S. Wang, Phys. Rev. Lett. **81**, 1909 (1998).

[26] S.N. Khanna and P. Jena, Chem. Phys. Lett. **219**, 479 (1994).

[27] V.M. Medel, J.U. Reveles, M.F. Islam, and S.N. Khanna, J. Phys. Chem. A **117**, 4297 (2013).

[28] V.M. Medel, J.U. Reveles, S.N. Khanna, V. Chauhan, P. Sen, and A.W. Castleman, Proc. Natl. Acad. Sci. **108**, 10062 (2011).

[29] K. Pradhan, J.U. Reveles, P. Sen, and S.N. Khanna, J. Chem. Phys. **132**, 124302 (2010).

[30] J.U. Reveles, S.N. Khanna, P.J. Roach, and A.W. Castleman, Proc. Natl. Acad. Sci. **103**, 18405 (2006).

[31] D.E. Bergeron, P.J. Roach, A.W. Castleman, N.O. Jones, and S.N. Khanna, Science **307**, 231 (2005).

[32] D.E. Bergeron, A.W. Castleman, T. Morisato, and S.N. Khanna, Science **304**, 84 (2004).

[33] D.E. Bergeron, A.W. Castleman, T. Morisato, and S.N. Khanna, J. Chem. Phys. **121**, 10456 (2004).

[34] A.C. Reber, S.N. Khanna, P.J. Roach, W.H. Woodward, and A.W. Castleman, J Am Chem Soc **129**, 16098 (2007).

[35] P.J. Roach, W.H. Woodward, A.W. Castleman, A.C. Reber, and S.N. Khanna, Science **323**, 492 (2009).

[36] A.C. Reber, P.J. Roach, W.H. Woodward, S.N. Khanna, and A.W. Castleman, J. Phys. Chem. A **116**, 8085 (2012).

[37] A.C. Reber, S.N. Khanna, P.J. Roach, W.H. Woodward, and A.W. Castleman, J Phys Chem A **114**, 6071 (2010).

[38] E. Janssens, X.J. Hou, M.T. Nguyen, and P. Lievens, J. Chem. Phys. **124**, 184319 (2006).

[39] G. Espinoza-Quintero, J.C.A. Duckworth, W.K. Myers, J.E. McGrady, and J.M. Goicoechea, J. Am. Chem. Soc. **136**, 1210 (2014).

[40] X. Jin, G. Espinoza-Quintero, B. Below, V. Arcisauskaite, J.M. Goicoechea, and J.E. McGrady, J. Organomet. Chem. (n.d.).

[41] J.M. Goicoechea and J.E. McGrady, Dalton Trans. **44**, 6755 (2015).

[42] M. Born and R. Oppenheimer, Ann. Phys. **389**, 457 (1927).

[43] M. Brack, Rev. Mod. Phys. **65**, 677 (1993).

[44] D. Sherrill, Sherrill Group Notes Chem. (n.d.).

[45] M.Y. Amusia, A.Z. Msezane, and V.R. Shaginyan, Phys. Scr. **68**, C133 (2003).

[46] D. Sholl and J. Steckel, *Density Functional Theory: A Practical Introduction* (Wiley, 2009).

[47] K. Capelle, ArXivcond-Mat0211443 (2002).

[48] A. Zangwill, Phys. Today **68**, 34 (2015).

[49] P. Hohenberg and W. Kohn, Phys. Rev. **136**, B864 (1964).

[50] W. Kohn and L. Sham, Phys. Rev. **140**, 1133 (1965).

[51] A.D. Becke, Phys. Rev. A **38**, 3098 (1988).

[52] A.D. Becke, J. Chem. Phys. **98**, 5648 (1993).

[53] J.P. Perdew, K. Burke, and M. Ernzerhof, Phys. Rev. Lett. **77**, 3865 (1996).

[54] G. te Velde, F.M. Bickelhaupt, E.J. Baerends, C. Fonseca Guerra, S.J.A. van Gisbergen, J.G. Snijders, and T. Ziegler, J. Comput. Chem. **22**, 931 (2001).

[55] P.M. Boerrigter, G. Te Velde, and J.E. Baerends, Int. J. Quantum Chem. **33**, 87 (1988).

[56] G. te Velde and E.J. Baerends, J. Comput. Phys. **99**, 84 (1992).

[57] G. te Velde and E.J. Baerends, Phys. Rev. B **44**, 7888 (1991).

[58] E. van Lenthe, E.J. Baerends, and J.G. Snijders, J. Chem. Phys. **101**, 9783 (1994).

[59] E. van Lenthe, J.G. Snijders, and E.J. Baerends, J. Chem. Phys. **105**, 6505 (1996).

[60] E. van Lenthe, E.J. Baerends, and J.G. Snijders, J. Chem. Phys. **99**, 4597 (1993).

[61] E. van Lenthe, A. Ehlers, and E.-J. Baerends, J. Chem. Phys. **110**, 8943 (1999).

[62] W.A. de Heer, Rev. Mod. Phys. **65**, 611 (1993).

[63] A.W. Castleman, (n.d.).

[64] Z. Luo, A.C. Reber, M. Jia, W.H. Blades, S.N. Khanna, and A.W. Castleman, Chem Sci (2016).

[65] M.W. Heaven, A. Dass, P.S. White, K.M. Holt, and R.W. Murray, J Am Chem Soc **130**, 3754 (2008).

[66] H. Häkkinen, Chem. Soc. Rev. **37**, 1847 (2008).

[67] X.-F. Yang, A. Wang, B. Qiao, J. Li, J. Liu, and T. Zhang, Acc. Chem. Res. **46**, 1740 (2013).

[68] P.D. Jadzinsky, G. Calero, C.J. Ackerson, D.A. Bushnell, and R.D. Kornberg, Science **318**, 430 (2007).

[69] M. Zhu, C.M. Aikens, F.J. Hollander, G.C. Schatz, and R. Jin, J Am Chem Soc **130**, 5883 (2008).

[70] K.-W. Klinkhammer, W. Uhl, J. Wagner, and W. Hiller, Angew. Chem. Int. Ed. Engl. **30**, 179 (1991).

[71] P. Henke, N. Trapp, C.E. Anson, and H. Schnöckel, Angew. Chem. **122**, 3214 (2010).

[72] A. Ecker, E. Weckert, and H. Schnöckel, Nature **387**, 379 (1997).

[73] H. Schnöckel, Chem. Rev. **110**, 4125 (2010).

[74] M. Neumaier, M. Olzmann, B. Kiran, K.H. Bowen, B. Eichhorn, S.T. Stokes, A. Buonaugurio, R. Burgert, and H. Schnöckel, J. Am. Chem. Soc. **136**, 3607 (2014).

[75] M.B. Abreu, C. Powell, A.C. Reber, and S.N. Khanna, J. Am. Chem. Soc. **134**, 20507 (2012).

[76] Z. Luo, C.J. Grover, A.C. Reber, S.N. Khanna, and A.W. Castleman, J. Am. Chem. Soc. **135**, 4307 (2013).

[77] P.A. Clayborne, O. Lopez-Acevedo, R.L. Whetten, H. Grönbeck, and H. Häkkinen, Eur. J. Inorg. Chem. **2011**, 2649 (2011).

[78] H.T. Le, S.M. Lang, J.D. Haeck, P. Lievens, and E. Janssens, Phys. Chem. Chem. Phys. **14**, 9350 (2012).

[79] P. Claes, E. Janssens, V.T. Ngan, P. Gruene, J.T. Lyon, D.J. Harding, A. Fielicke, M.T. Nguyen, and P. Lievens, Phys. Rev. Lett. **107**, 173401 (2011).

[80] T. Höltzl, N. Veldeman, J. De Haeck, T. Veszprémi, P. Lievens, and M.T. Nguyen, Chem. - Eur. J. **15**, 3970 (2009).

[81] V. Chauhan, M.B. Abreu, A.C. Reber, and S.N. Khanna, Phys. Chem. Chem. Phys. **17**, 15718 (2015).

[82] M. Qian, A.C. Reber, A. Ugrinov, N.K. Chaki, S. Mandal, H.M. Saavedra, S.N. Khanna, A. Sen, and P.S. Weiss, ACS Nano **4**, 235 (2009).

[83] V. Chauhan, V.M. Medel, J. Ulises Reveles, S.N. Khanna, and P. Sen, Chem. Phys. Lett. **528**, 39 (2012).

[84] V. Chauhan, S. Sahoo, and S.N. Khanna, J. Am. Chem. Soc. **138**, 1916 (2016).

[85] P. Pyykko, Chem. Rev. **88**, 563 (1988).

[86] H. Häkkinen and U. Landman, Phys. Rev. B **62**, R2287 (2000).

[87] H. Häkkinen, M. Moseler, and U. Landman, Phys. Rev. Lett. **89**, (2002).

[88] D. Schooss, P. Weis, O. Hampe, and M.M. Kappes, Philos. Trans. R. Soc. Lond. Math. Phys. Eng. Sci. **368**, 1211 (2010).

Appendix

This appendix is broken down into two sections. The first corresponds to the study conducted in Chapter 4 and the second corresponds to the study in Chapter 5.

CHAPTER 4 APPENDIX
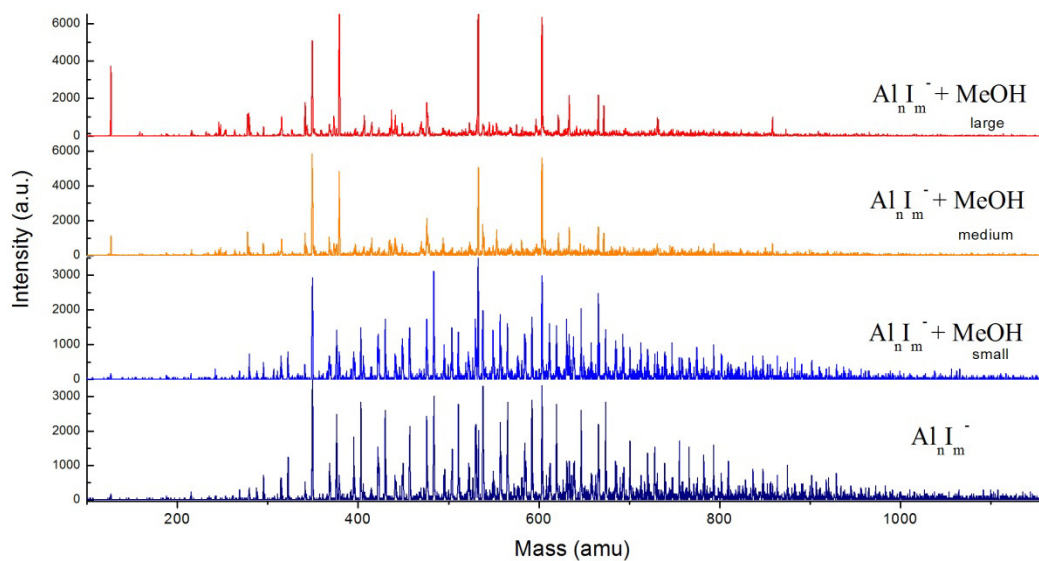
Figure A1. **Flow-rate dependence.** Methanol-etched $Al_nI_m^-$ distribution at different flow-rate of the oxygen gas (~0.5 sccm; ~6 sccm; and ~20 sccm respectively).
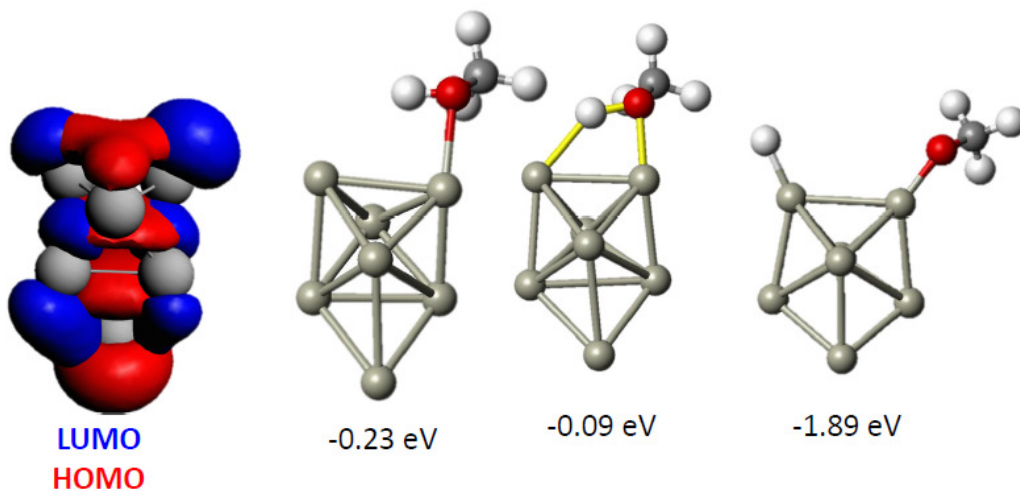
Figure A2. The HOMO and LUMO isosurfaces of Al_7^-, and the binding energy, transition state energy and final state energy for the reaction of methanol with Al_7^-.
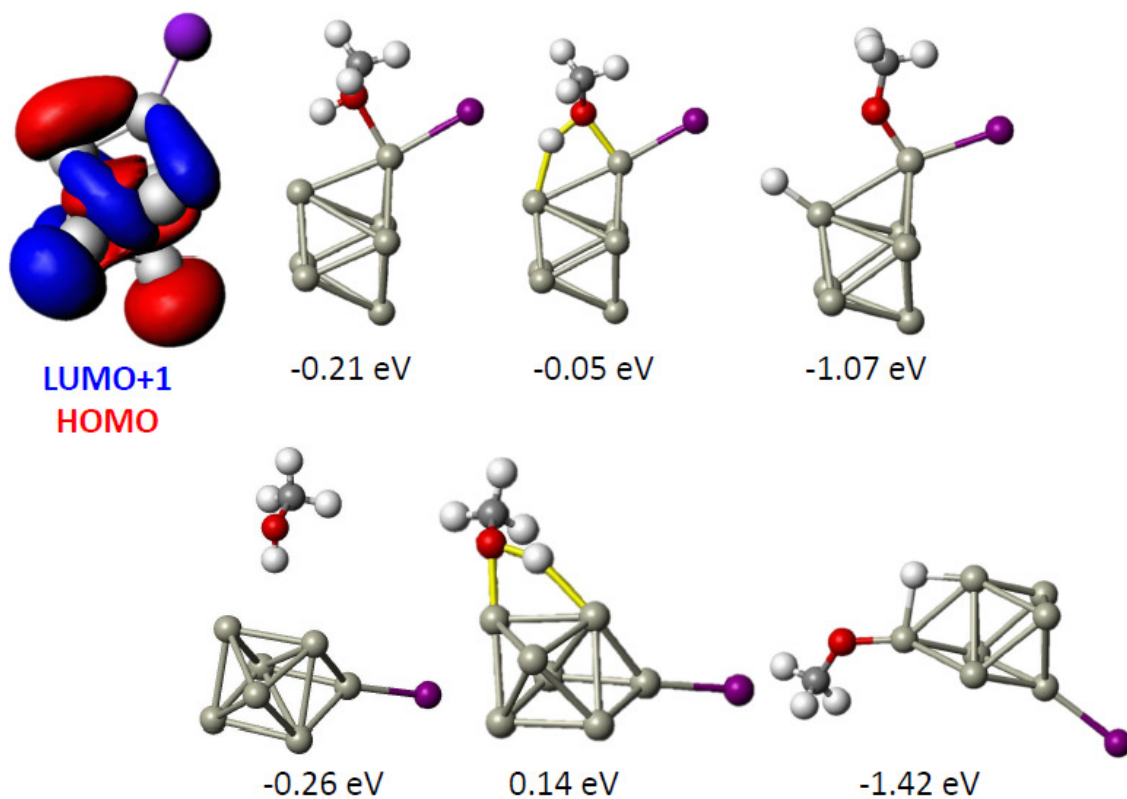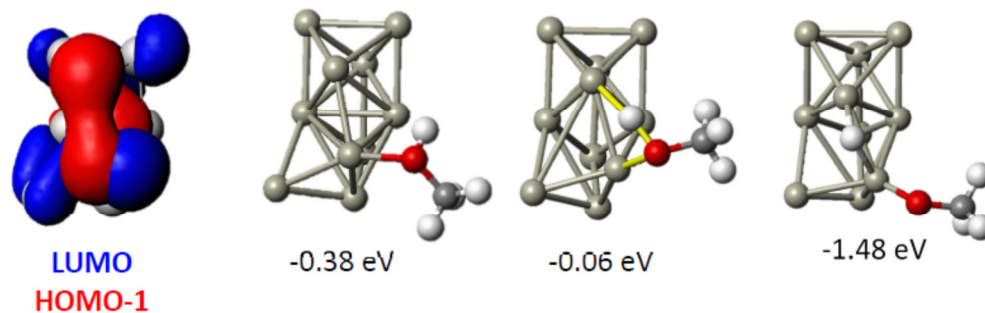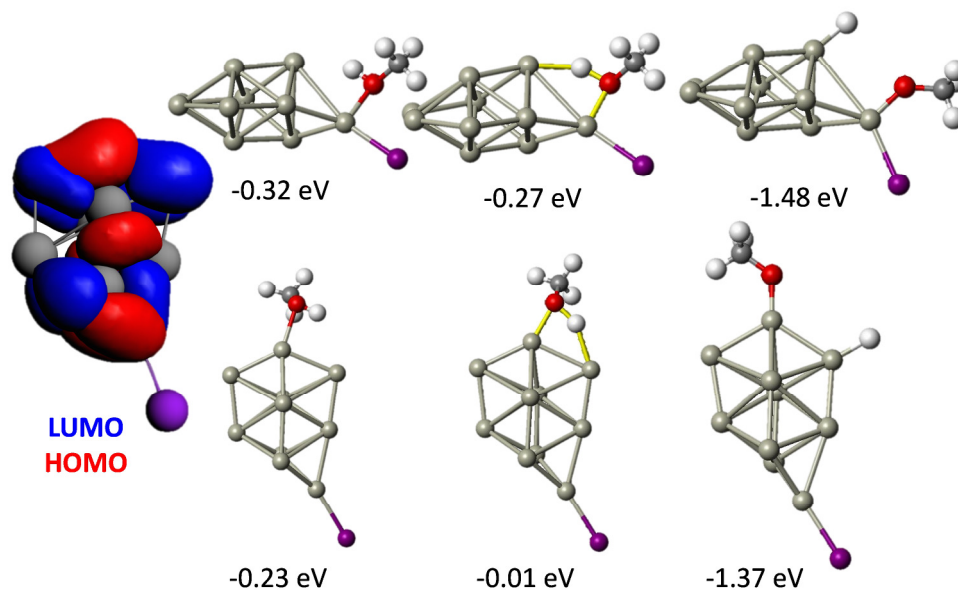

Figure A3. The HOMO and LUMO+ isosurfaces of Al_7I^-, and the binding energy, transition state energy and final state energy for the reaction of methanol with Al_7I^- at the I site (top row), and metal site (bottom row).
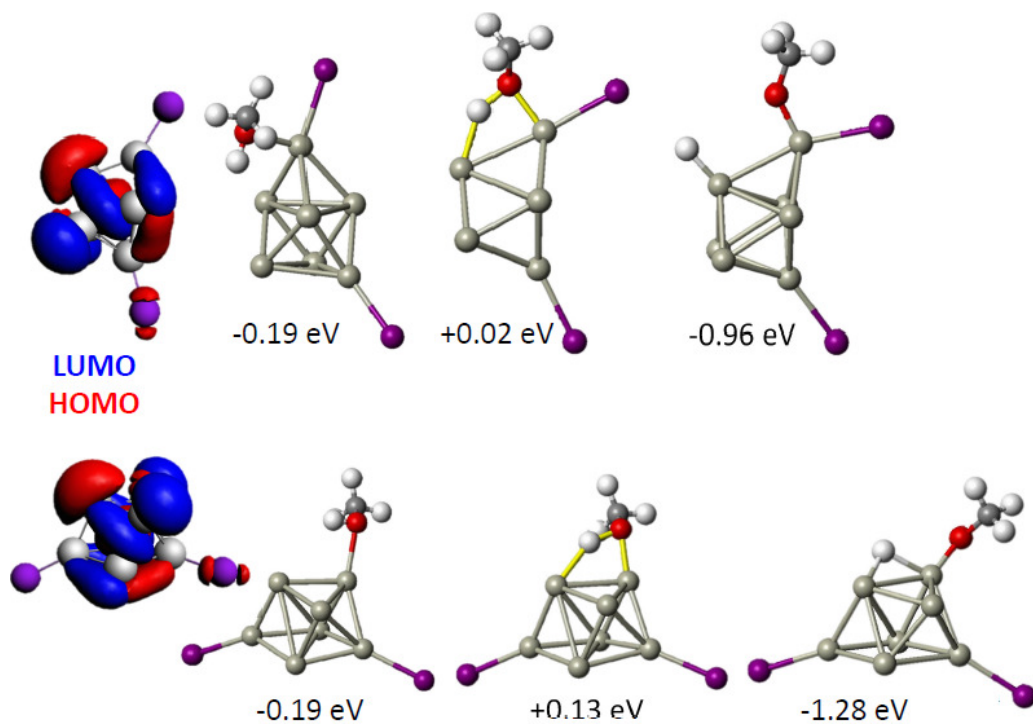
Figure A4. The HOMO and LUMO isosurfaces of $Al_7I_2^-$, and the binding energy, transition state energy and final state energy for the reaction of methanol with $Al_7I_2^-$ at the I site (top row), and metal site (bottom row).
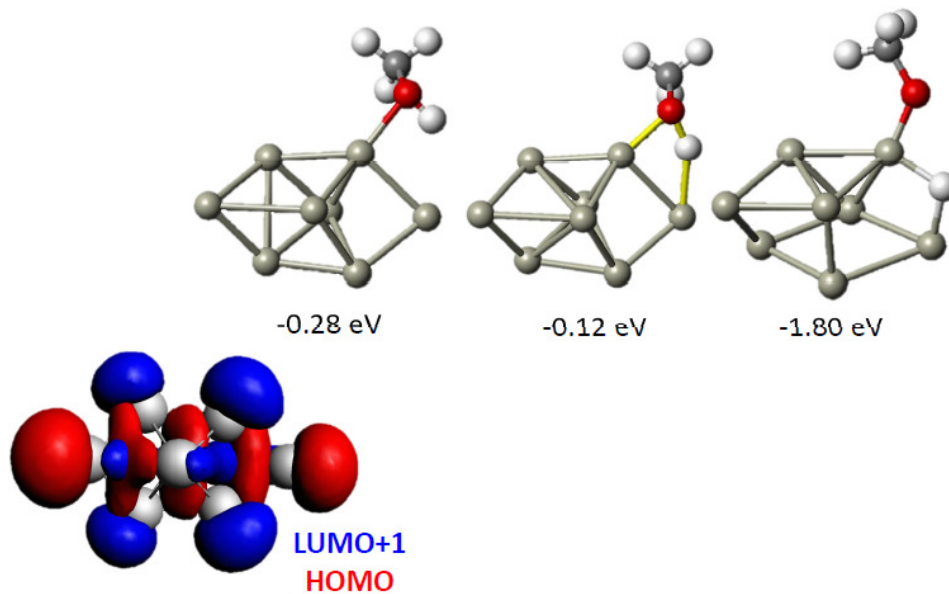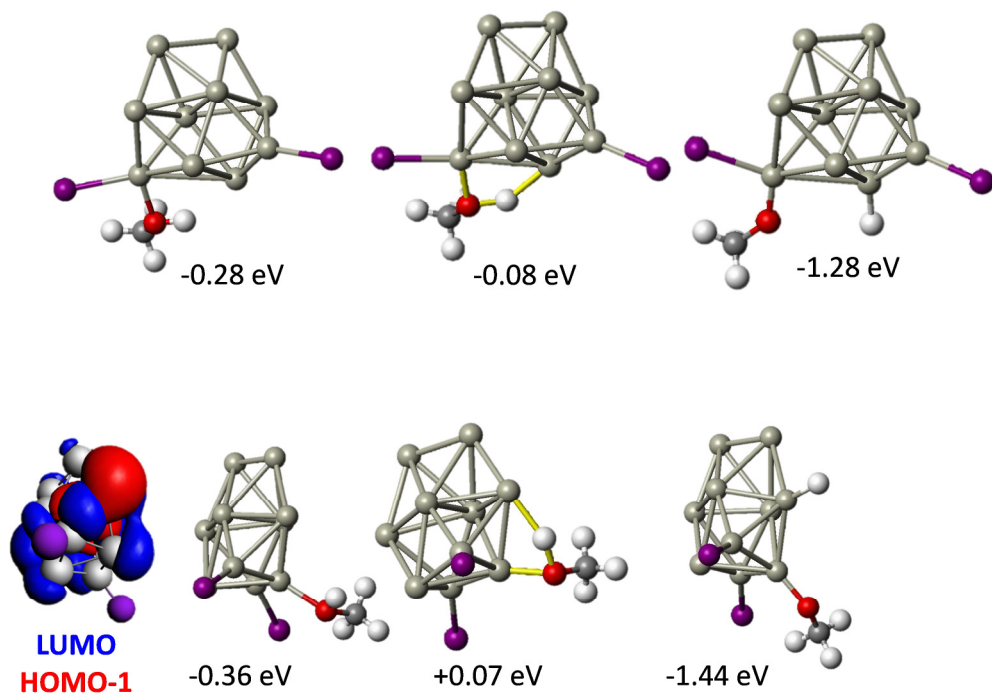

Figure A5. The HOMO and LUMO+1 isosurfaces of Al_8^-, and the binding energy, transition state energy and final state energy for the reaction of methanol with Al_8^-.
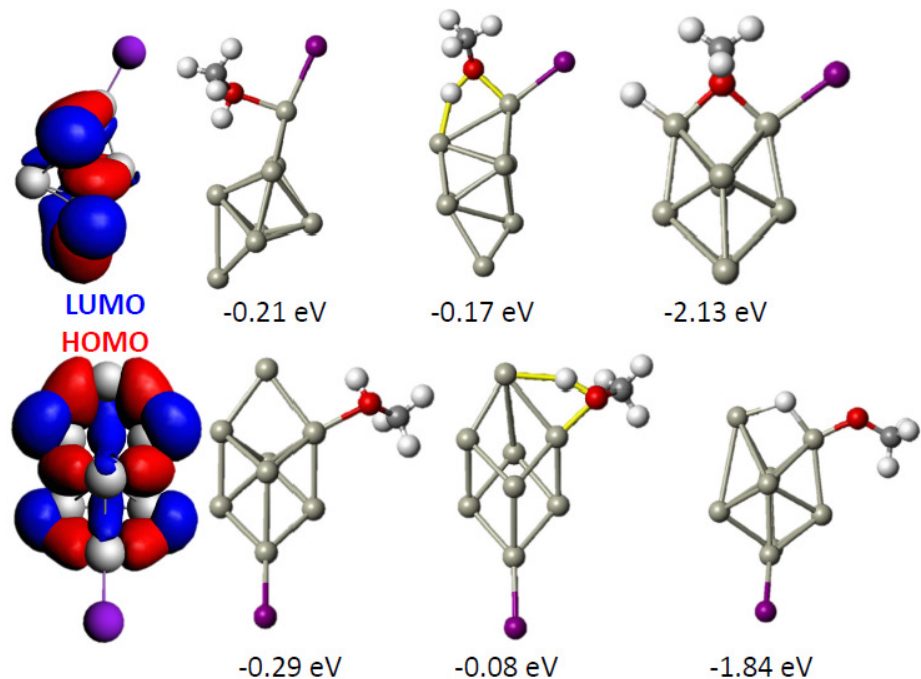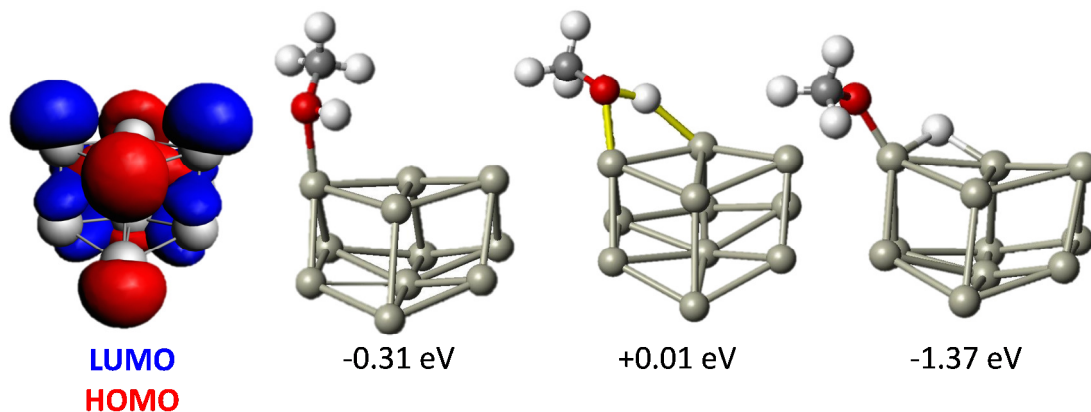
Figure A6. The HOMO and LUMO isosurfaces of Al_8I^-, and the binding energy, transition state energy and final state energy for the reaction of methanol with Al_8I^- at the I site (top row), and metal site (bottom row).
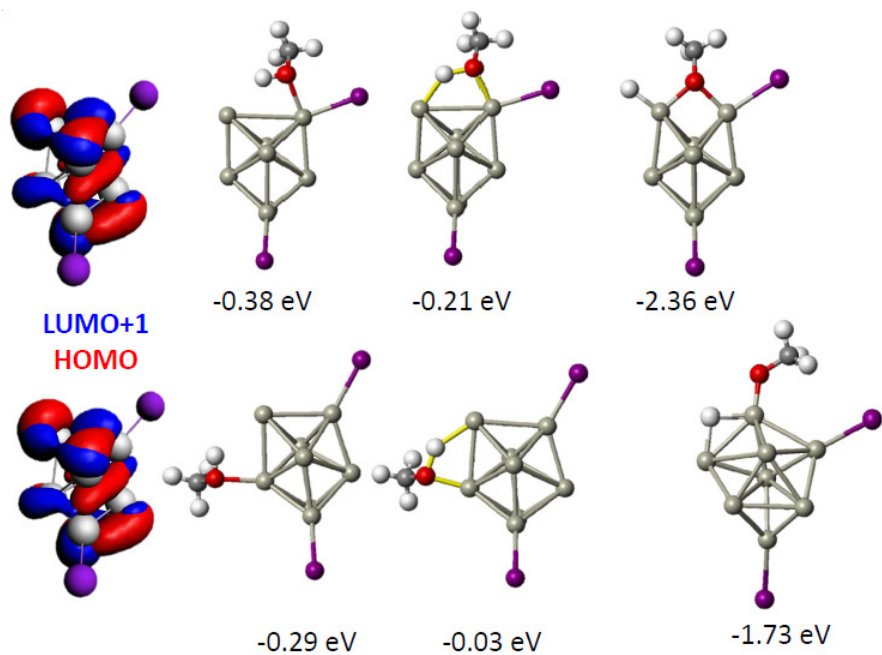
Figure A7. The HOMO and LUMO+1 isosurfaces of $Al_8I_2^-$, and the binding energy, transition state energy and final state energy for the reaction of methanol with $Al_7I_2^-$ at the I site (top row), and metal site (bottom row).
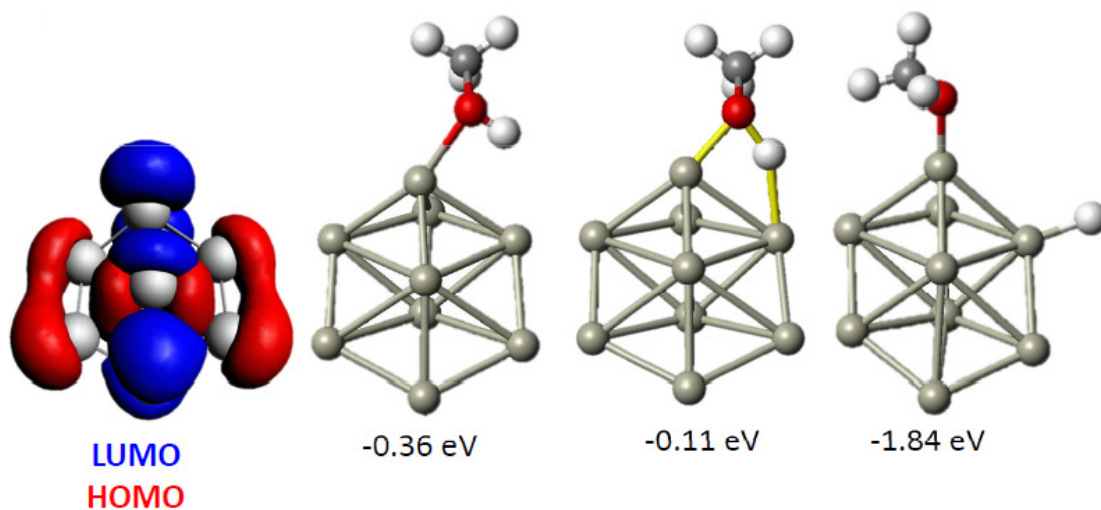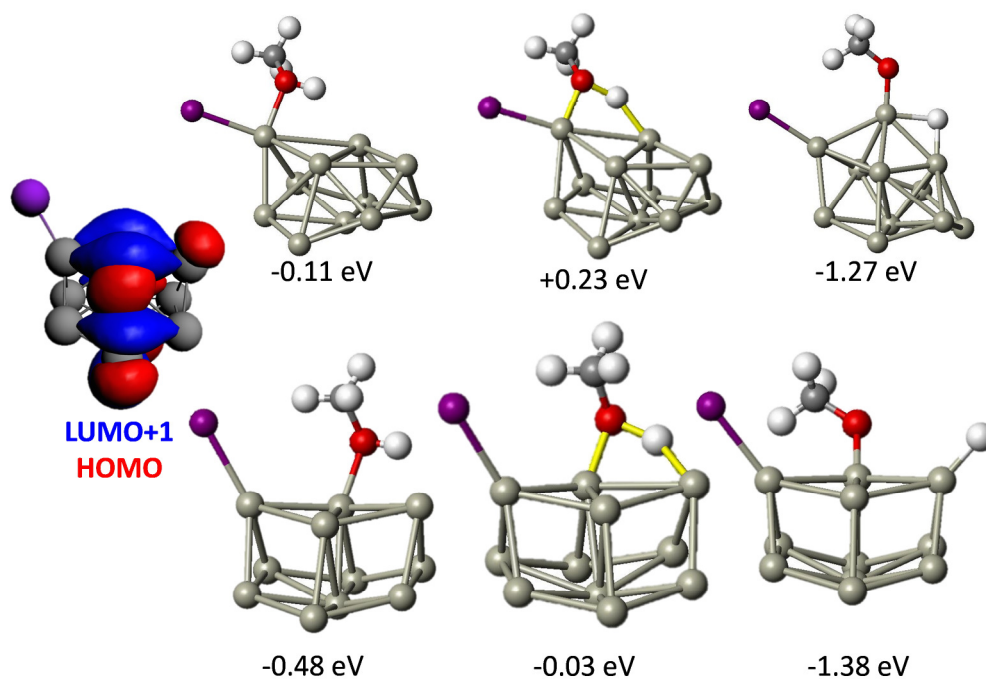
Figure A8. The HOMO and LUMO isosurfaces of Al$_9^-$, and the binding energy, transition state energy and final state energy for the reaction of methanol with Al$_9^-$.
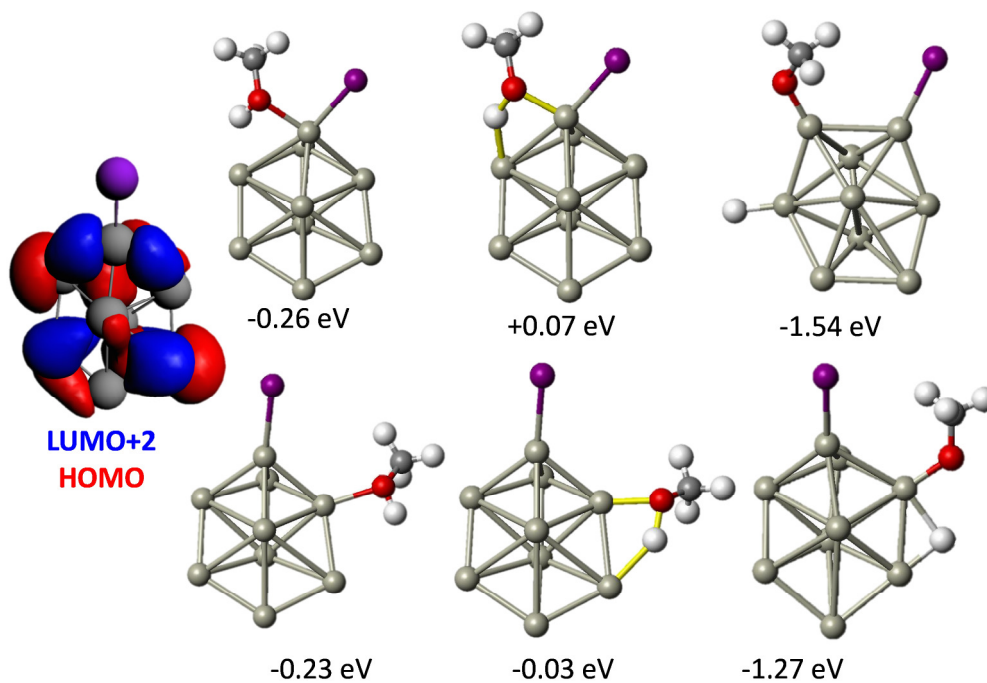
Figure A9. The HOMO and LUMO+2 isosurfaces of Al$_9$I$^-$, and the binding energy, transition state energy and final state energy for the reaction of methanol with Al$_9$I$^-$ at the I site (top row), and metal site (bottom row).
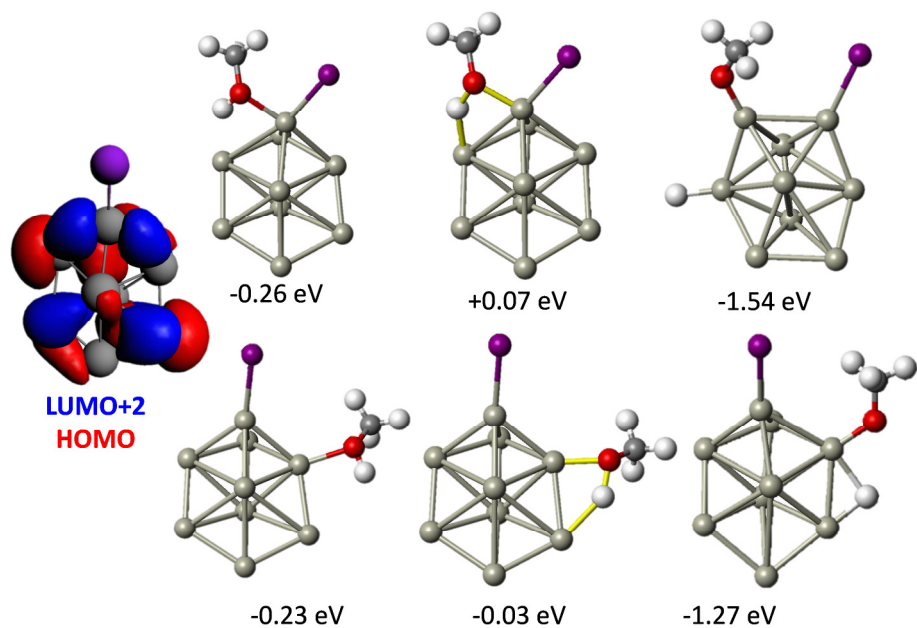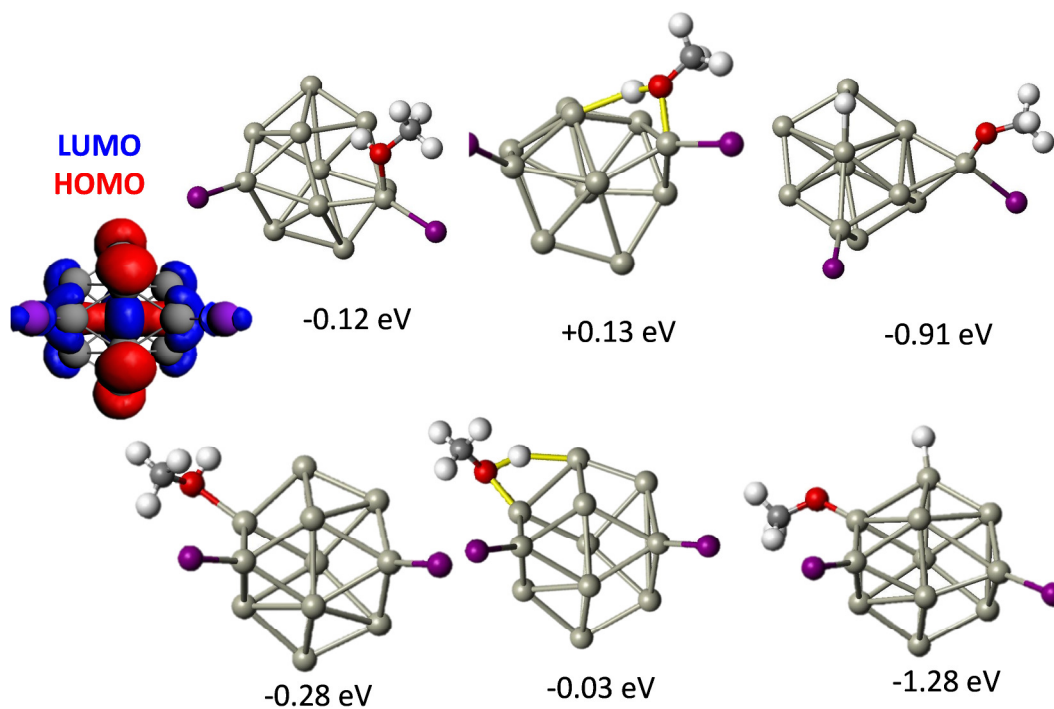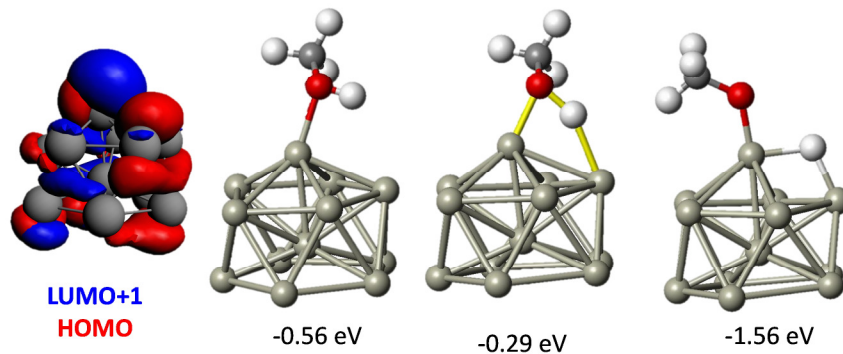
Figure A10. The HOMO and LUMO+2 isosurfaces of $Al_9I_2^-$, and the binding energy, transition state energy and final state energy for the reaction of methanol with $Al_9I_2^-$ at the I site (top row), and metal site (bottom row).
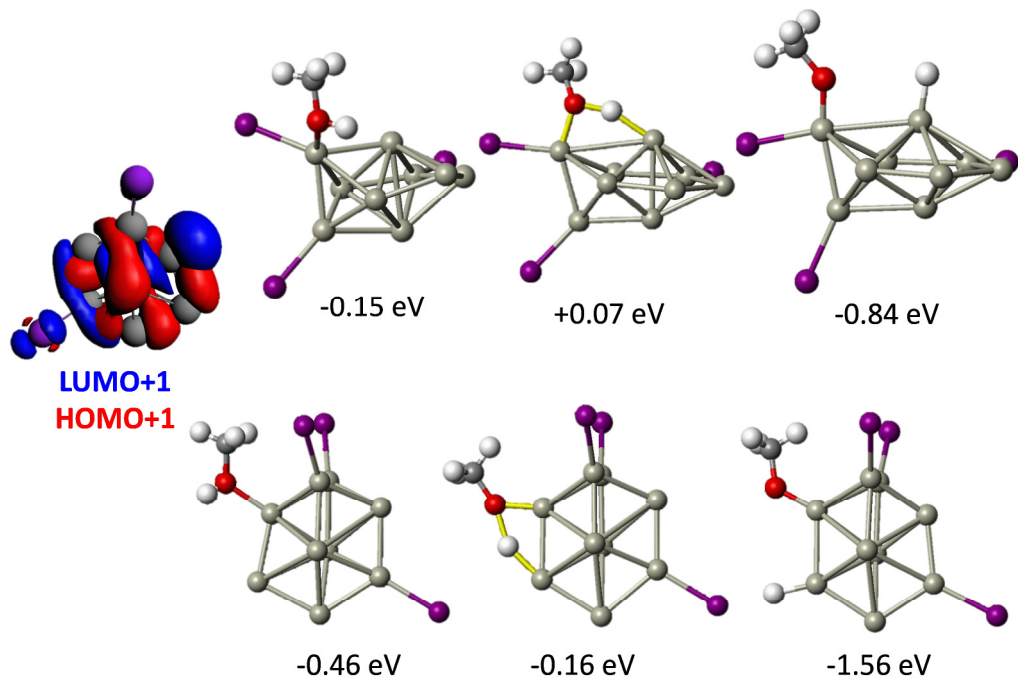
Figure A11. The HOMO+1 and LUMO+1 isosurfaces of the ground state of $Al_9I_3^-$, and the binding energy, transition state energy and final state energy for the reaction of methanol with $Al_9I_3^-$ at the I site (top row), and metal site (bottom row).

LUMO+3
HOMO

-0.27 eV   0.00 eV   -1.38 eV

-0.30 eV   -0.02 eV   -1.34 eV
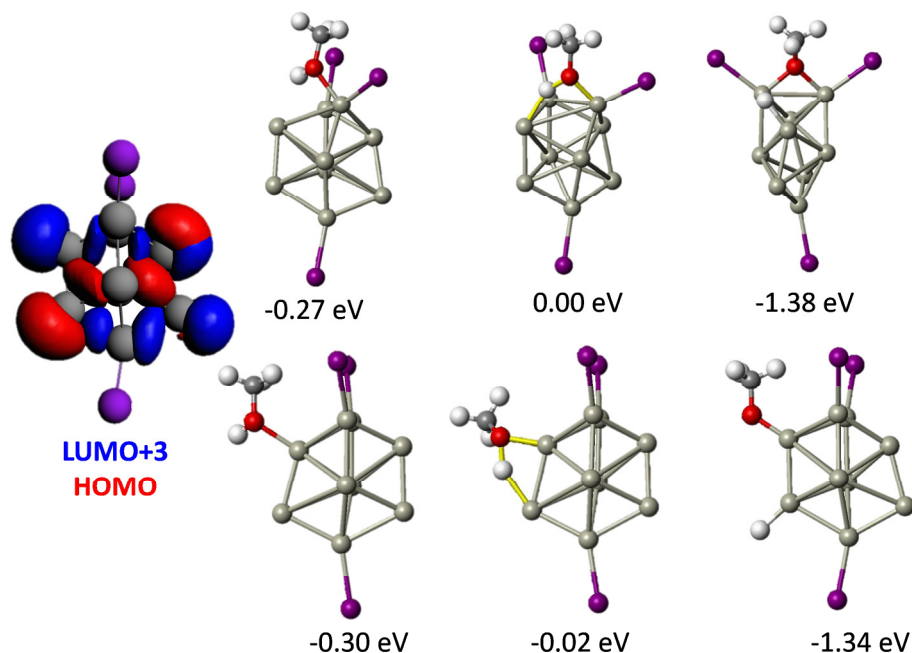
Figure A12. The HOMO and LUMO+3 isosurfaces of the second isomer of $Al_9I_3^-$, and the binding energy, transition state energy and final state energy for the reaction of methanol with the second isomer $Al_9I_3^-$ at the I site (top row), and metal site (bottom row). The energy is +0.03 eV higher than the isomer from S15.

LUMO+3
HOMO

-0.27 eV   0.00 eV   -1.38 eV

-0.30 eV   -0.02 eV   -1.34 eV
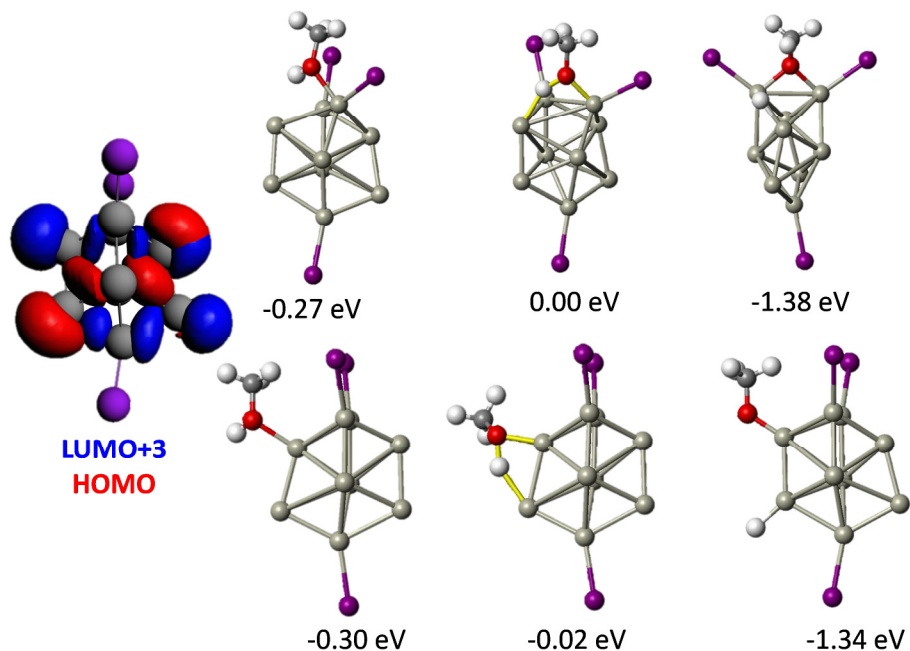
Figure A13. The HOMO and LUMO isosurfaces of the third isomer of $Al_9I_3^-$, and the binding energy, transition state energy and final state energy for the reaction of methanol with the third isomer $Al_9I_3^-$ at the I site (top row), and metal site (bottom row). The energy is +0.07 eV higher than the isomer from S15.

88

Figure A14. The HOMO and LUMO+1 isosurfaces of Al_{10}^-, and the binding energy, transition state energy and final state energy for the reaction of methanol with Al_{10}^-.
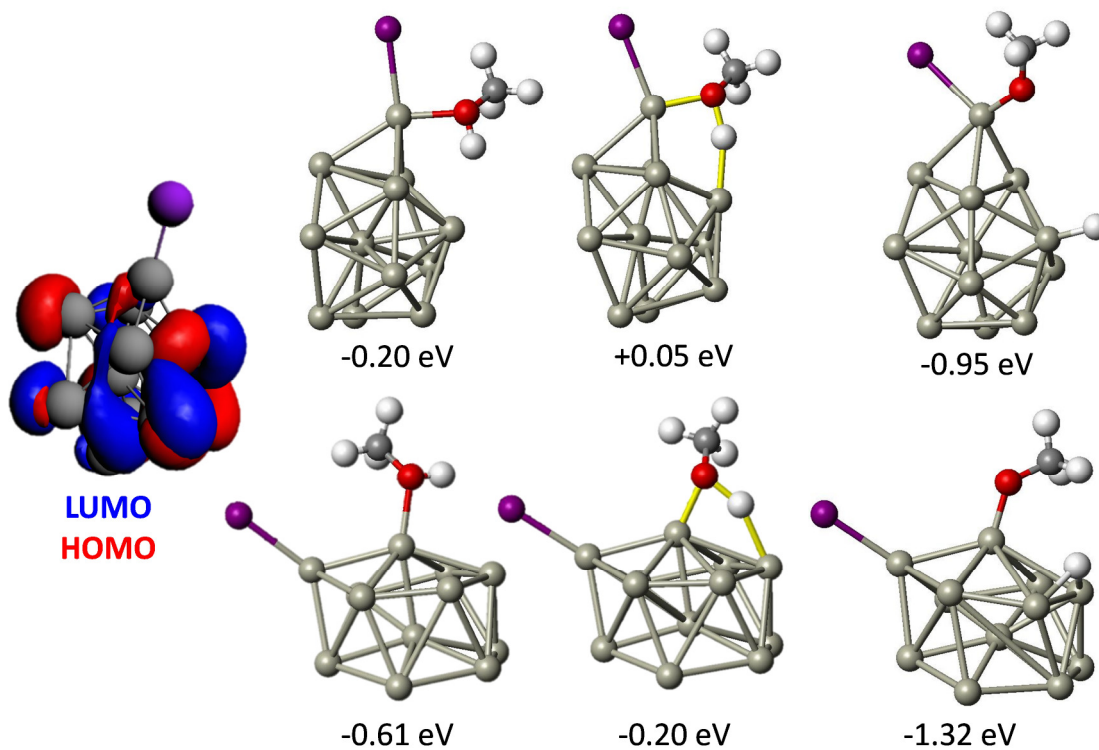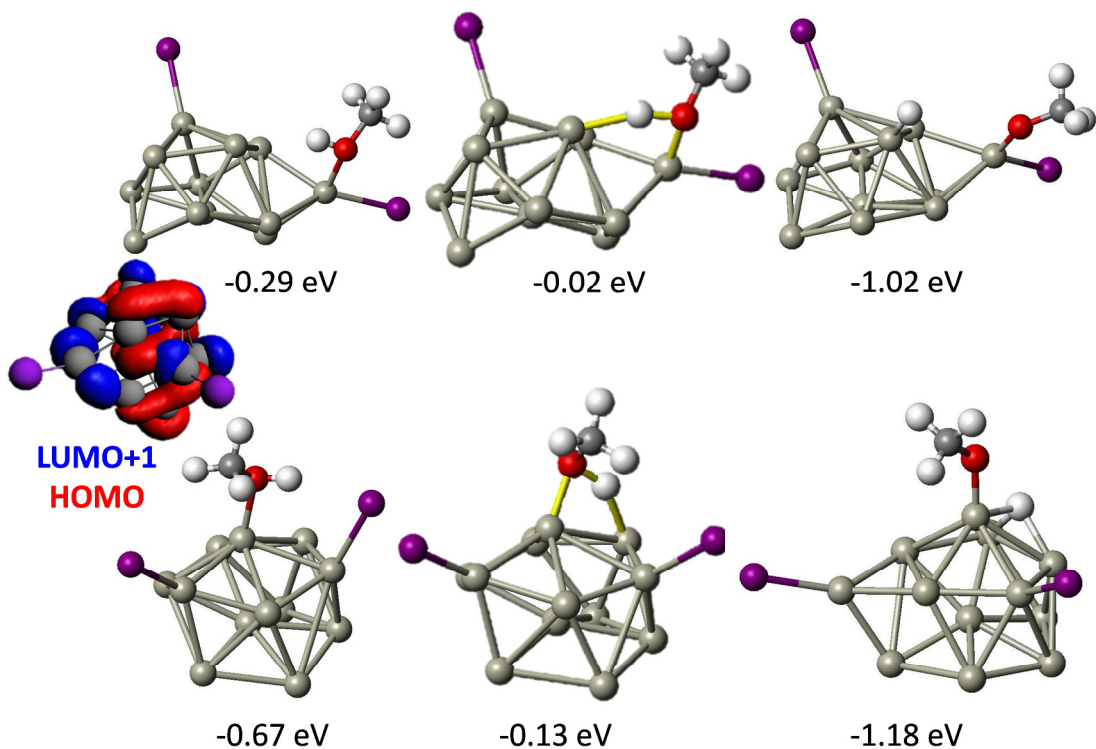

Figure A15. The HOMO and LUMO isosurfaces of $Al_{10}I^-$, and the binding energy, transition state energy and final state energy for the reaction of methanol with $Al_{10}I^-$ at the I site (top row), and metal site (bottom row).
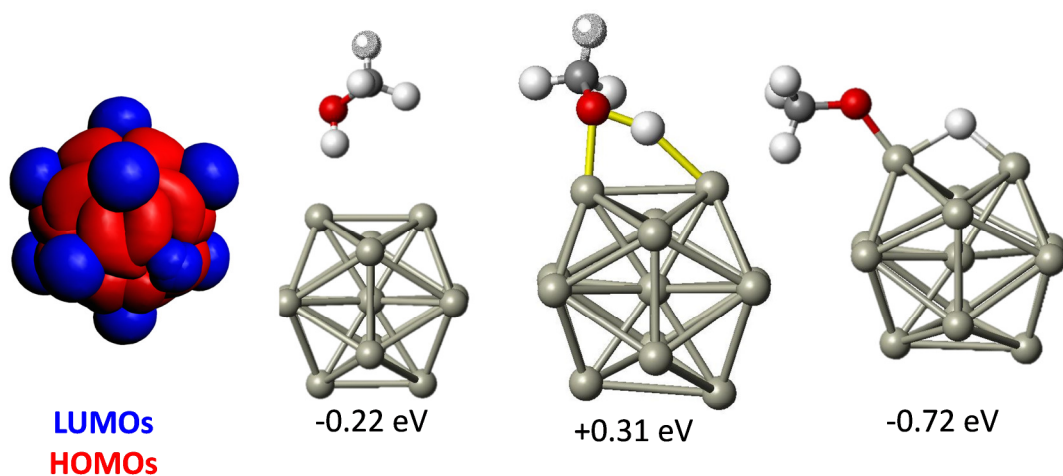
Figure A16. The HOMO-1 and LUMO isosurfaces of $Al_{10}I_2^-$, and the binding energy, transition state energy and f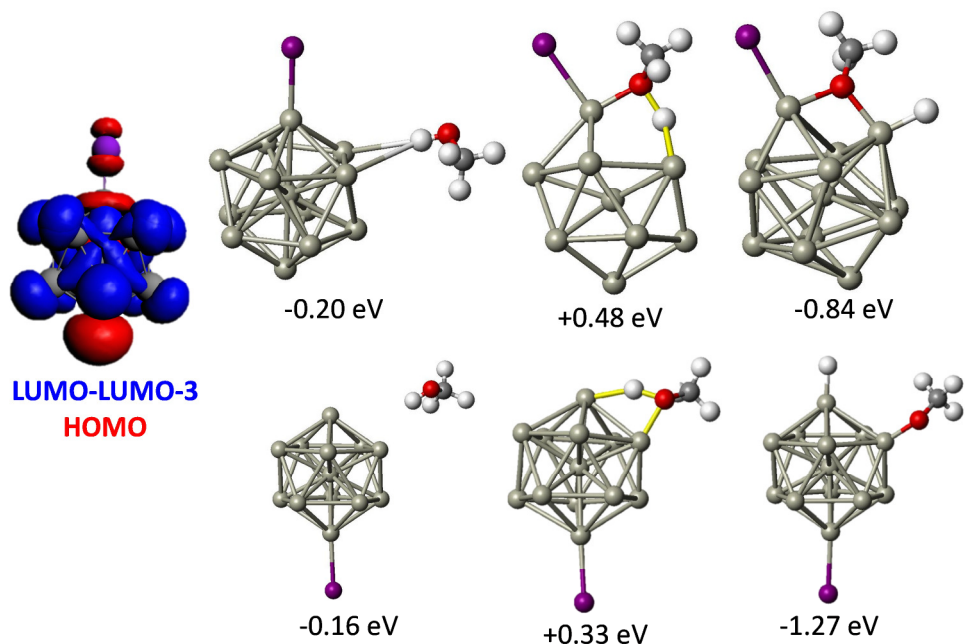inal state energy for the reaction of methanol with $Al_{10}I_2^-$ at the I site (top row), and metal site (bottom row).
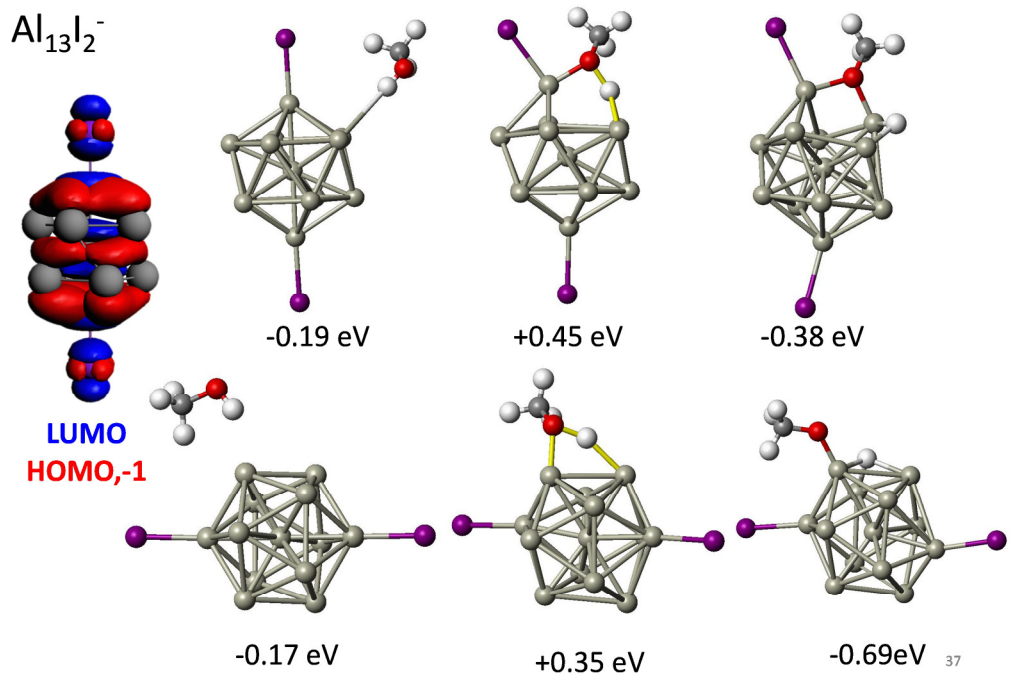

Figure A17. The HOMO and LUMO isosurfaces of Al_{11}^-, and the binding energy, transition state energy and final state energy for the reaction of methanol with Al_{11}^-.

Figure A18. The HOMO and LUMO+1 isosurfaces of $Al_{11}I^-$, and the binding energy, transition state energy and final state energy for the reaction of methanol with $Al_{11}I^-$ at the I site (top row), and metal site (bottom row).

Figure A19. The HOMO and LUMO isosurfaces of $Al_{11}I_2^-$, and the binding energy, transition state energy and final state energy for the reaction of methanol with $Al_{11}I_2^-$ at the I site (top row), and metal site (bottom row).
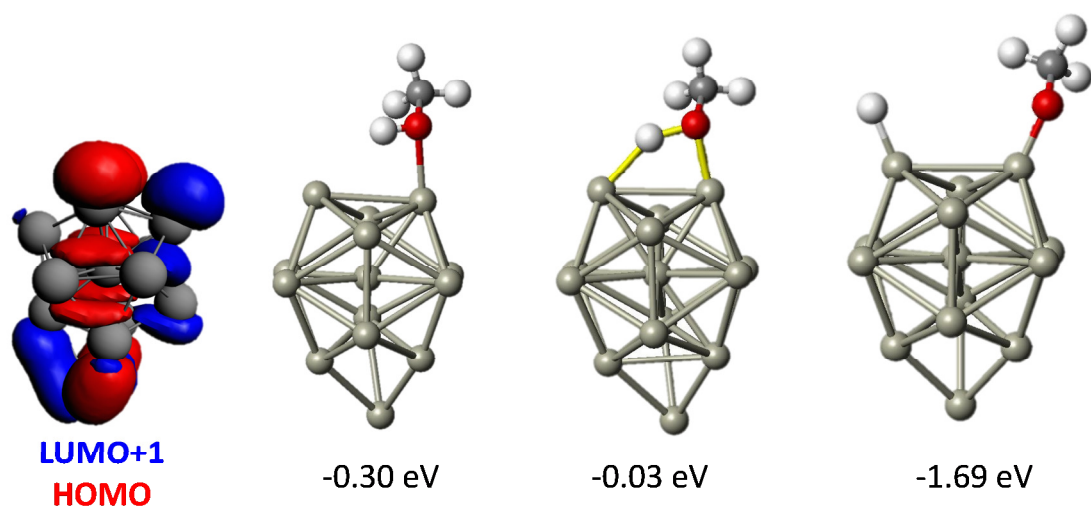
Figure A20. The HOMO and LUMO+1 isosurfaces of Al_{12}^-, and the binding energy, transition state energy and final state energy for the reaction of methanol with Al_{12}^-.
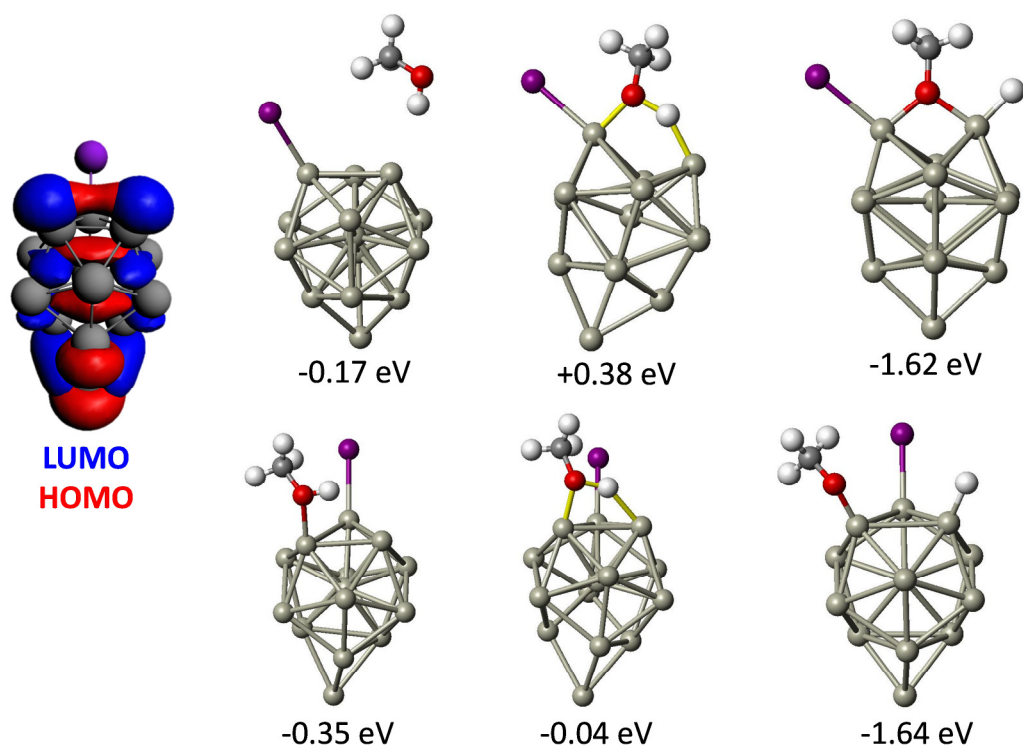

Figure A21. The HOMO and LUMO isosurfaces of $Al_{12}I^-$, and the binding energy, transition state energy and final state energy for the reaction of methanol with $Al_{12}I^-$ at the I site (top row), and metal site (bottom row).

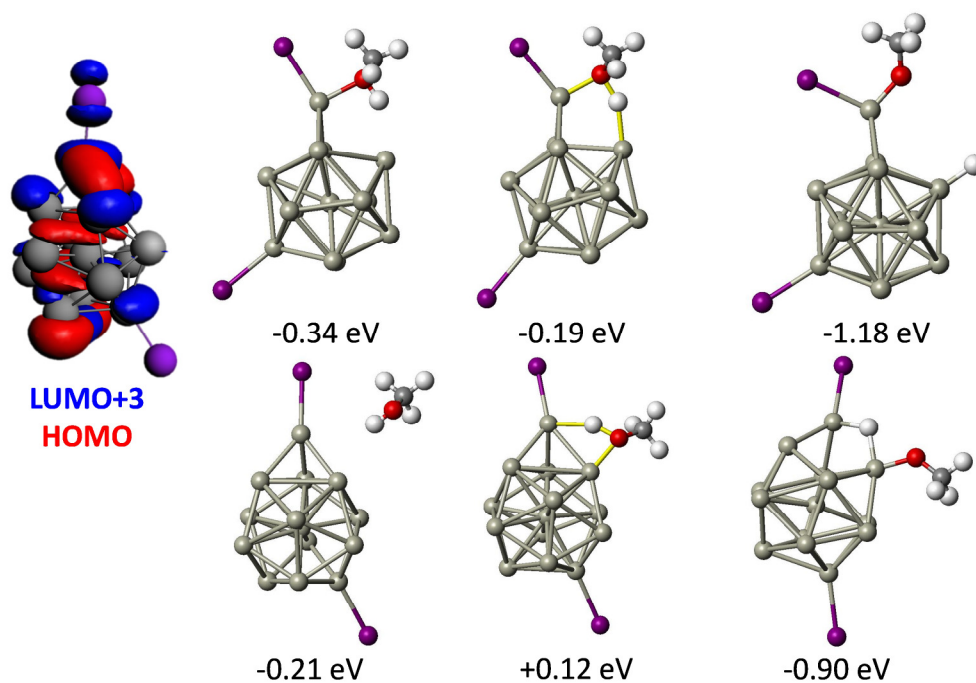**Figure A22**. The HOMO and LUMO+1 isosurfaces of $Al_{12}I_2^-$, and the binding energy, transition state energy and final state energy for the reaction of methanol with $Al_{12}I_2^-$ at the I site (top row), and metal site (bottom row).

Figure A23. The HOMO-HOMO-3 and LUMO-LUMO+3 isosurfaces of Al_{13}^-, and the binding energy, transition state energy and final state energy for the reaction of methanol with Al_{13}^-.

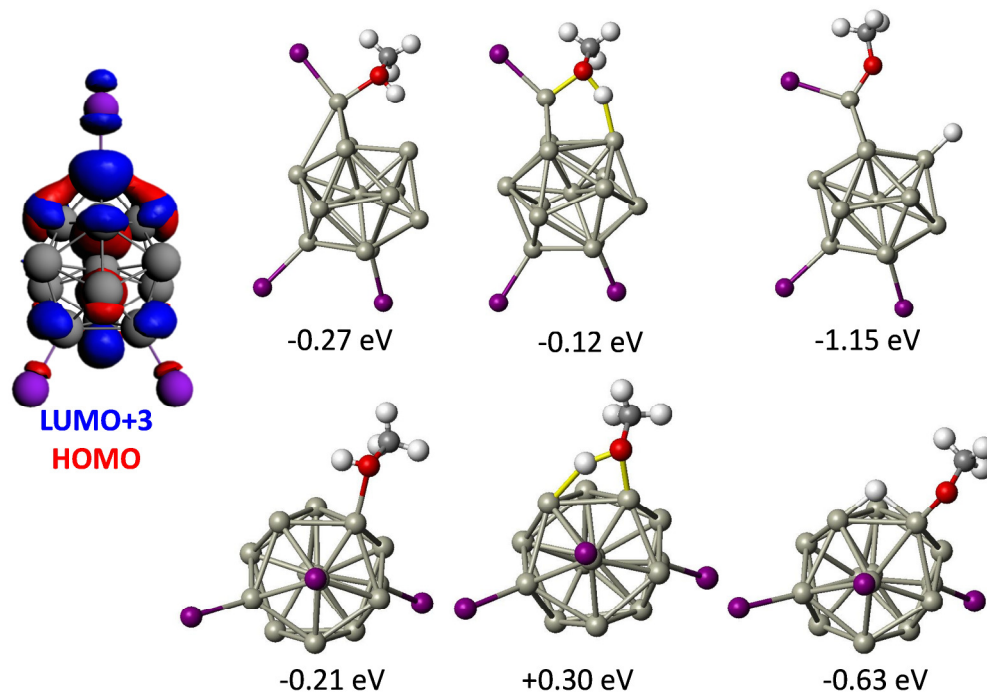**Figure A24.** The HOMO and LUMO-LUMO-3 isosurfaces of $Al_{13}I^-$, and the binding energy, transition state energy and final state energy for the reaction of methanol with $Al_{13}I^-$ at the I site (top row), and metal site (bottom row).

Figure A25. The HOMO/HOMO-1 and LUMO isosurfaces of $Al_{13}I_2^-$, and the binding energy, transition state energy and final state energy for the reaction of methanol with $Al_{13}I_2^-$ at the I site (top row), and metal site (bottom row).

Figure A26. The HOMO and LUMO+1 isosurfaces of Al_{14}^-, and the binding energy, transition state energy and final state energy for the reaction of methanol with Al_{14}^-.

Figure A27. The HOMO and LUMO isosurfaces of $Al_{14}I^-$, and the binding energy, transition state energy and final state energy for the reaction of methanol with $Al_{14}I^-$.

Figure A28. The HOMO and LUMO+3 isosurfaces of $Al_{14}I_2^-$, and the binding energy, transition state energy and final state energy for the reaction of methanol with $Al_{14}I_2^-$.

Figure A29. The HOMO and LUMO+3 isosurfaces of $Al_{14}I_3^-$, and the binding energy, transition state energy and final state energy for the reaction of methanol with $Al_{14}I_3^-$.

CHAPTER 5 APPENDIX
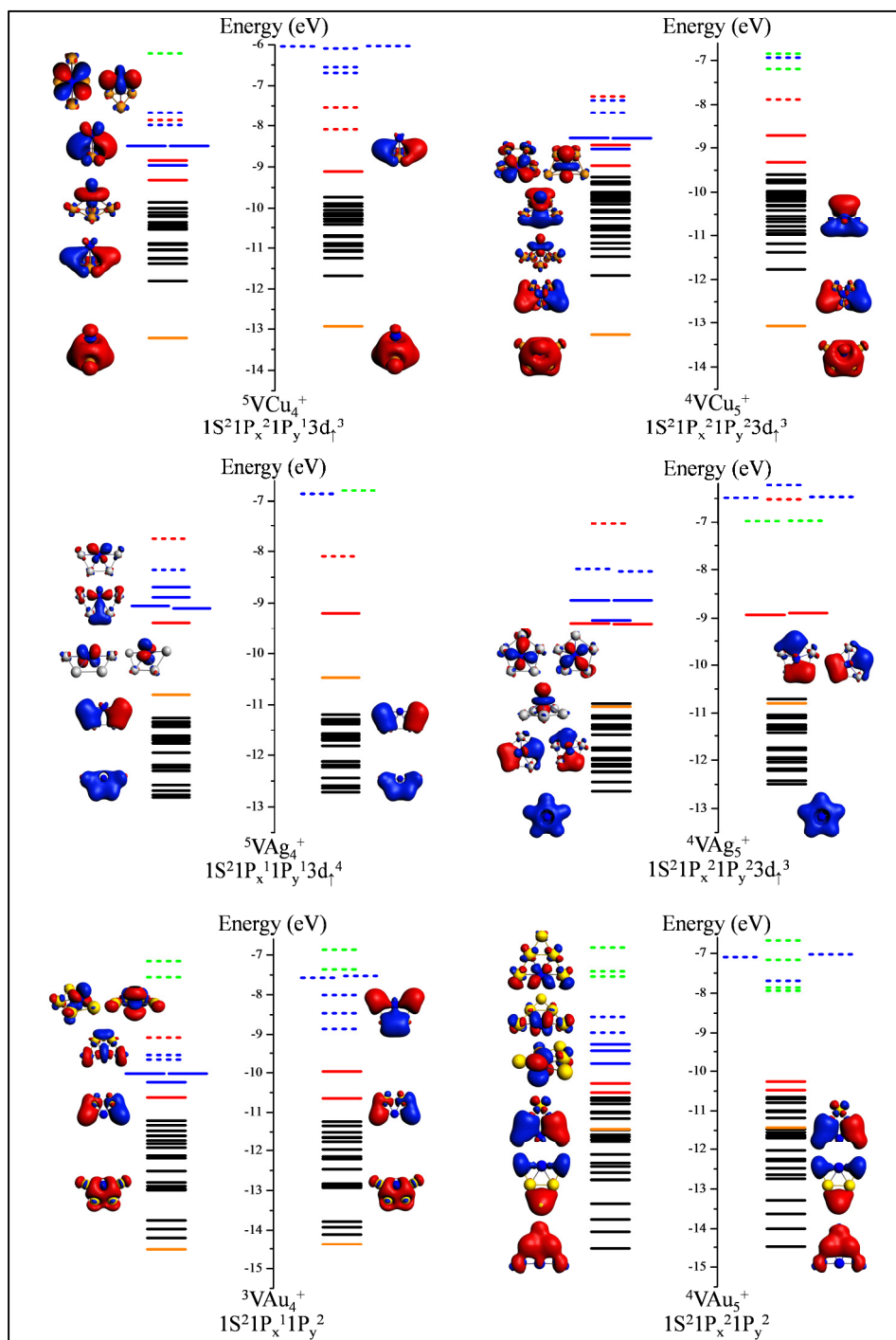
Figure A30. Molecular Orbital Analysis of VX_4^+ and VX_5^+ (X= Cu, Ag, and Au). Localized and delocalized orbitals of each cluster are shown for both the majority and minority spin channels. Filled lines correspond to occupied orbitals and dashed lines correspond to unoccupied orbitals.
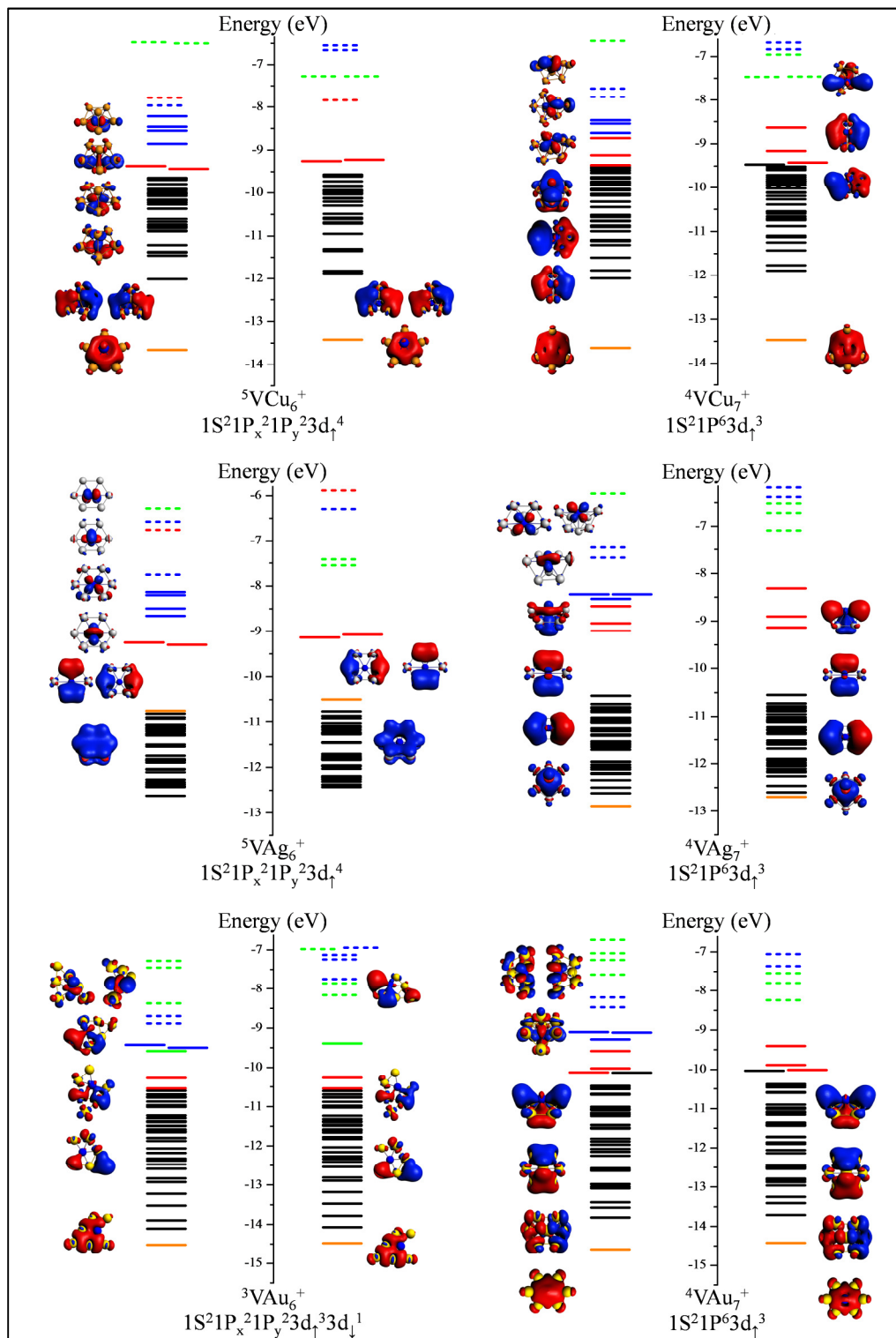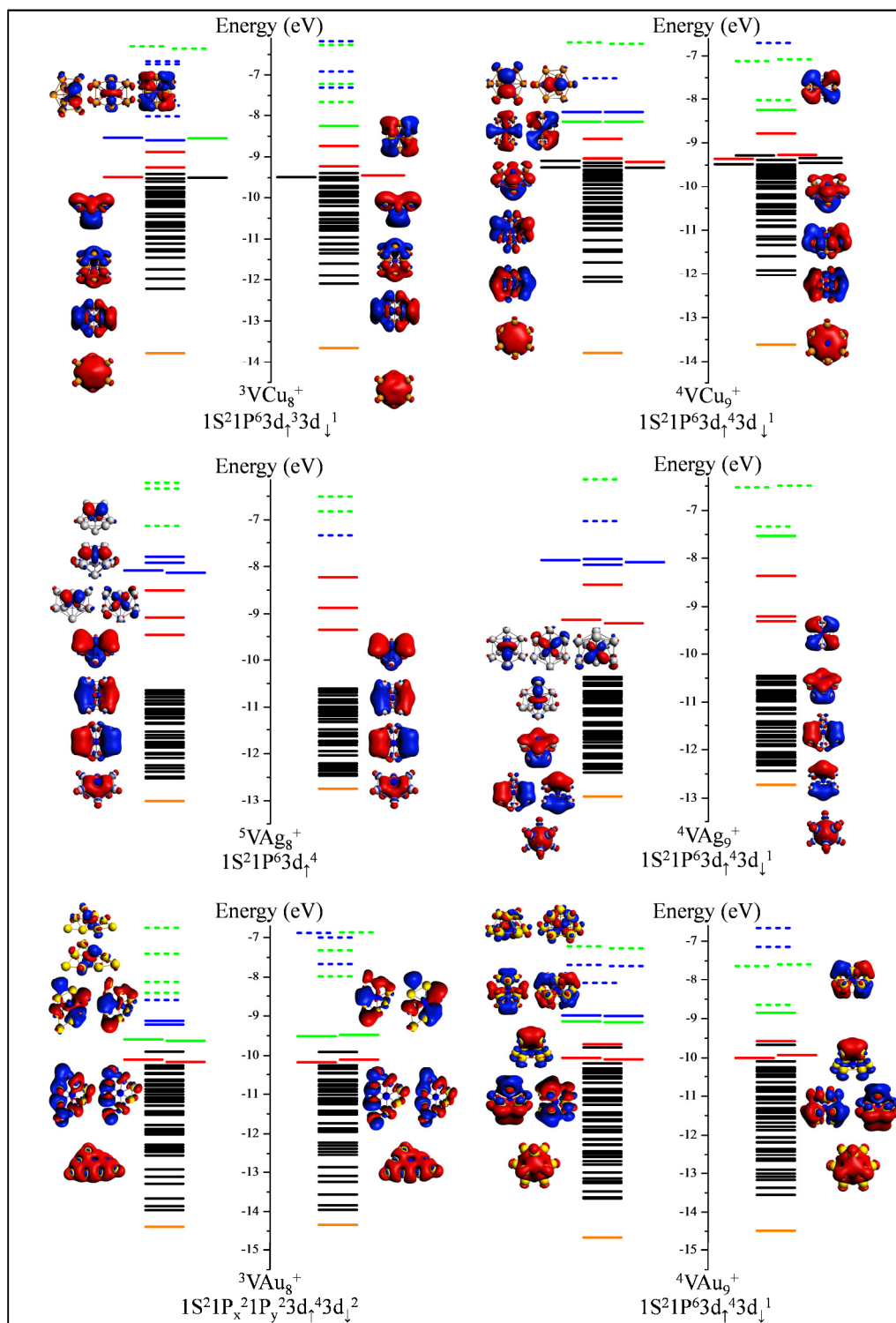
Figure A31. Molecular Orbital Analysis of VX_6^+ and VX_7^+ (X= Cu, Ag, and Au). Localized and delocalized orbitals of each cluster are shown for both the majority and minority spin channels. Filled lines correspond to occupied orbitals and dashed lines correspond to unoccupied orbitals.
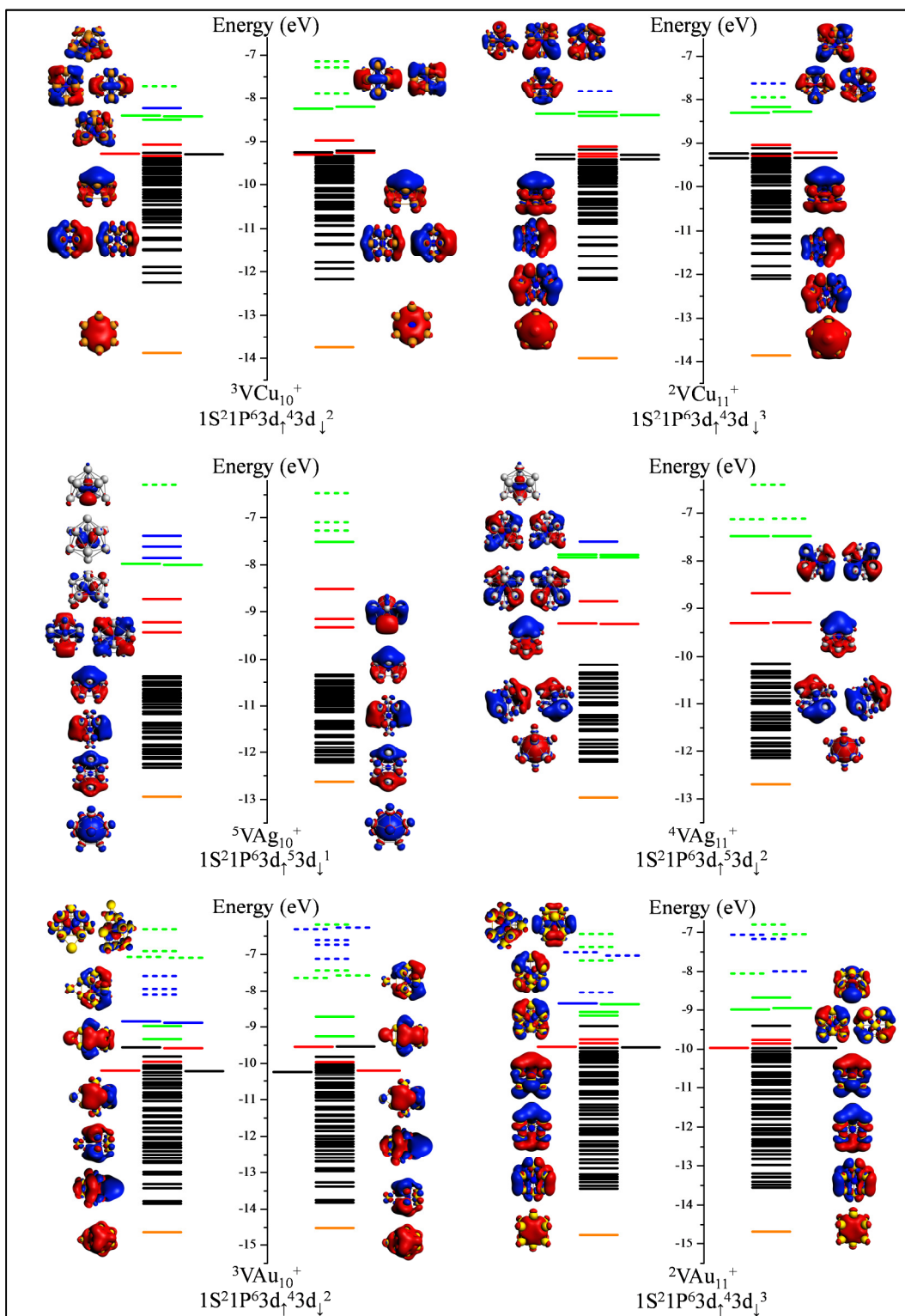
Figure A32. Molecular Orbital Analysis of VX_8^+ and VX_9^+ (X= Cu, Ag, and Au). Localized and delocalized orbitals of each cluster are shown for both the majority and minority spin channels. Filled lines correspond to occupied orbitals and dashed lines correspond to unoccupied orbitals.
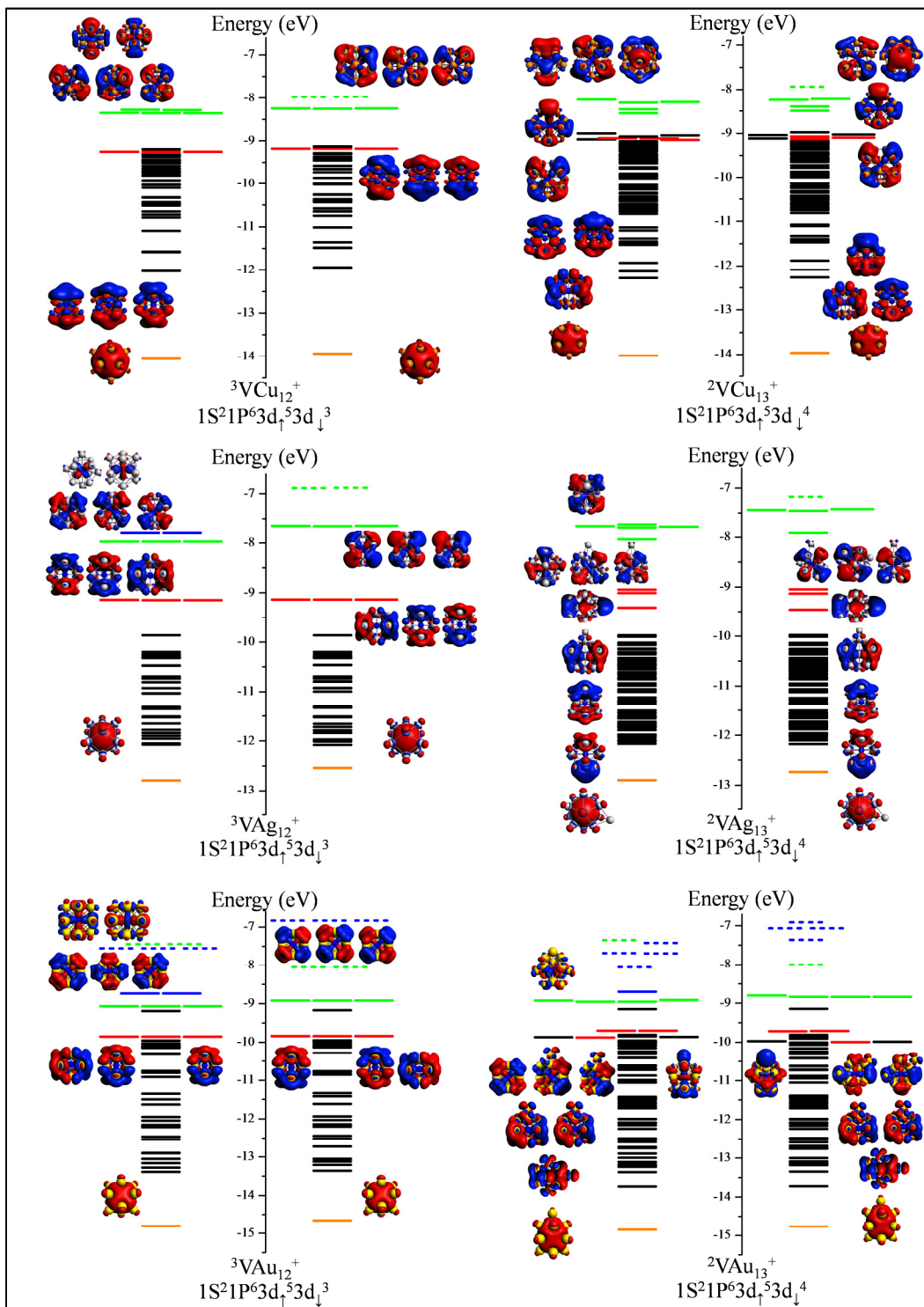
Figure A33. Molecular Orbital Analysis of VX_{10}^{+} and VX_{11}^{+} (X= Cu, Ag, and Au). Localized and delocalized orbitals of each cluster are shown for both the majority and minority spin channels. Filled lines correspond to occupied orbitals and dashed lines correspond to unoccupied orbitals.
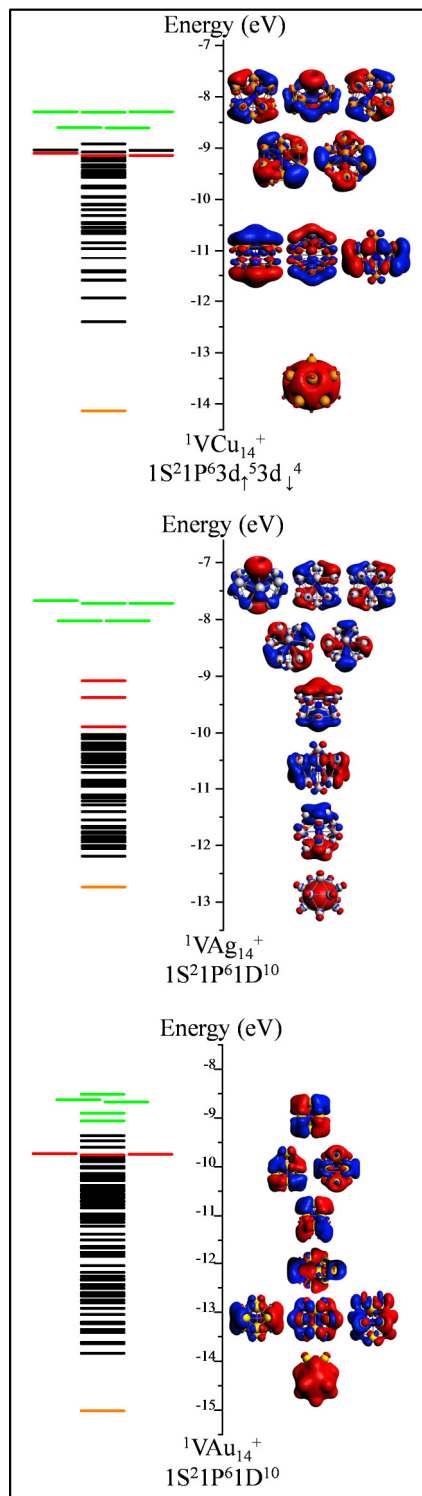
Figure A34. Molecular Orbital Analysis of VX_{12}^+ and VX_{13}^+ (X= Cu, Ag, and Au). Localized and delocalized orbitals of each cluster are shown for both the majority and minority spin channels. Filled lines correspond to occupied orbitals and dashed lines correspond to unoccupied orbitals.

Figure A35. Molecular Orbital Analysis of VX_{14}^{+} (X= Cu, Ag, and Au). Localized and delocalized orbitals of each cluster are shown for both the majority and minority spin channels. Filled lines correspond to occupied orbitals and dashed lines correspond to unoccupied orbitals.
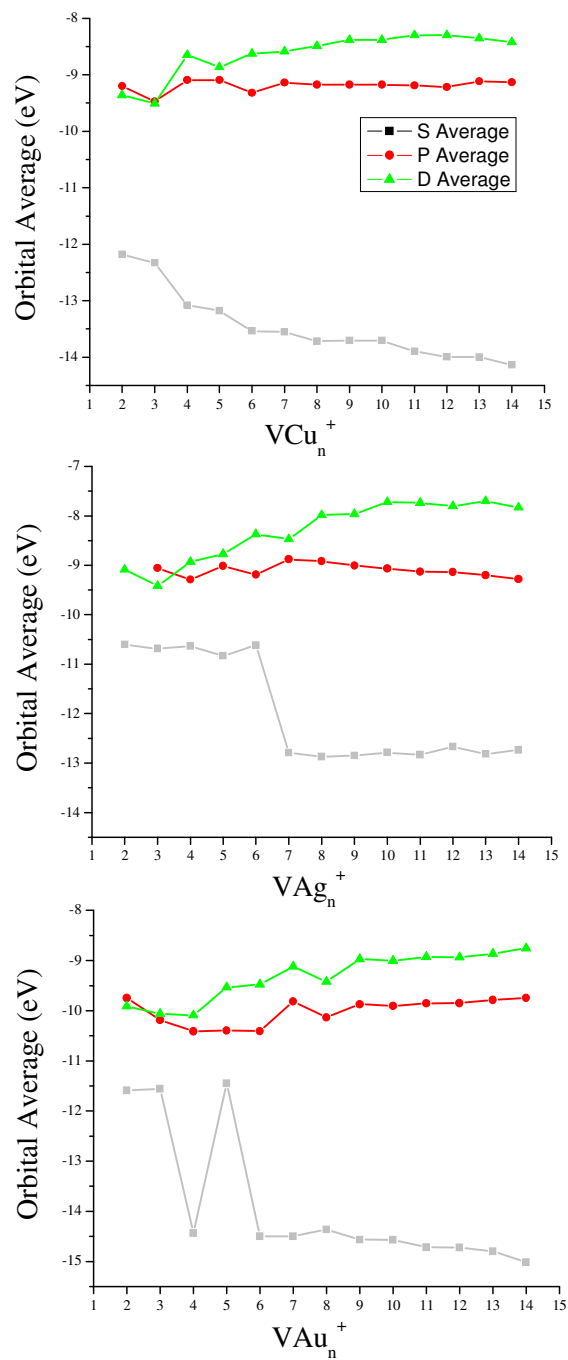
Figure A36. Average Orbital Energy of the delocalized orbitals of VX_{2-14}^+ (X= Cu, Ag, and Au).

S, P and D Orbital Width

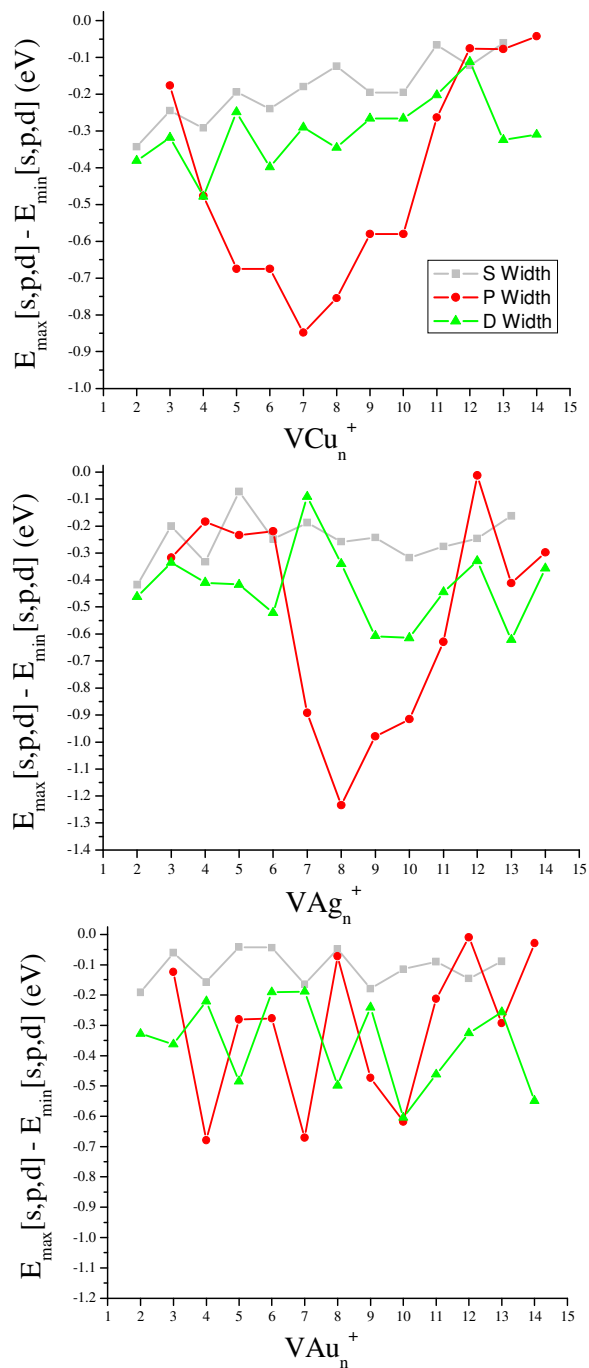**Figure A37.** Delocalized orbital width of VX_{2-14}^{+} (X= Cu, Ag, and Au). These values were obtained by subtracting the highest energy value associated with the S, P, and 3d/D orbital by the lowest energy value of that same orbital.

Vitae

William Harrison Blades is the son of Candace Evans and Charles Craig Blades and the brother of Caroline Upshur Blades. Born July 19, 1991 in Richmond, Virginia, Will conducted his undergraduate studies at Virginia Commonwealth University, and he received his Bachelor of Science in Physics, with a minor in Mathematics in the spring of 2014. When he is not spending his time cheering on the VCU Men's Basketball team or savoring new whiskey, Will enjoys spending his time traveling and exploring the world with friends and family.